
Methods¹

Expedition 330 Scientists²

Chapter contents

Procedures	1
Sedimentology	3
Paleontology	6
Igneous petrology and volcanology	8
Alteration petrology	14
Structural geology	15
Geochemistry	17
Physical properties	19
Paleomagnetism	25
Downhole logging	29
Microbiology	34
References	38
Figures	44
Tables	68

Procedures

Numbering of sites, holes, cores, and samples

Drilling sites are numbered consecutively from the first site drilled by the D/V *Glomar Challenger* in 1968. Integrated Ocean Drilling Program (IODP) Expedition 301 began using the prefix “U” to designate sites occupied by the US Implementing Organization (USIO) vessel (the R/V *JOIDES Resolution*). For all IODP drill sites, a letter suffix distinguishes each hole drilled at the same site. The first hole drilled is assigned the site number modified by the suffix “A,” the second hole takes the site number and the suffix “B,” and so on. Three Expedition 330 sites have only one hole (A). Sites U1375 and U1377 have two holes (A and B).

The cored interval is measured in meters below seafloor (mbsf). In general, depth below seafloor is determined by subtracting the water depth estimated from the initial drill pipe measurement to the seafloor from the total drill pipe measurement. During Expedition 330, all core depths below seafloor were calculated according to core depth below seafloor Method A (CSF-A) (see “IODP Depth Scales Terminology” at www.iodp.org/program-policies/). To more easily communicate shipboard results, all depths are reported in this volume as mbsf unless otherwise noted.

The depth interval assigned to an individual core begins with the depth below seafloor at which coring began and extends to the depth to which coring advanced. Each coring interval is generally ~9.5 m, which is the length of a core barrel; however, coring intervals may be shorter. When applicable, attempts were made during Expedition 330 to core the uppermost soft-sediment succession using a gravity-push technique with little or no rotation of the rotary core barrel assembly. When formation resistance was felt (at varied depths), the core barrel was retrieved before drill string rotation was initiated. In addition, depending on recovery rate and penetration speed in the hard rock portion of the hole, the core barrel was occasionally retrieved after only ~5 m of penetration, yielding a half-core.

Cores taken from a hole are numbered sequentially from the top of the hole downward. Core numbers and their associated cored intervals are unique in a given hole. Generally, maximum recovery for a single core is 9.5 m of rock or sediment contained in a plastic liner (6.6 cm internal diameter) plus an additional ~0.2 m in the core catcher, which is a device at the bottom of the core

¹Expedition 330 Scientists, 2012. Methods. In Koppers, A.A.P., Yamazaki, T., Geldmacher, J., and the Expedition 330 Scientists, *Proc. IODP*, 330: Tokyo (Integrated Ocean Drilling Program Management International, Inc.).
doi:10.2204/iodp.proc.330.102.2012
²Expedition 330 Scientists’ addresses.



barrel that prevents the core from sliding out when the barrel is retrieved from the hole. In certain situations, recovery may exceed the 9.5 m maximum. In soft sediments this is normally caused by core expansion resulting from depressurization. In hard rock cores this typically occurs when a pedestal of rock fails to break off and is grabbed by the core barrel of the subsequent core.

Recovered cores are divided into 1.5 m sections that are numbered serially from the top downward. When full recovery is obtained, the sections are numbered 1–7, with the last section usually being <1.5 m. Rarely, an unusually long core may require more than seven sections. When the recovered core is shorter than the cored interval, by convention the top of the core is deemed to be located at the top of the cored interval for the purpose of calculating (consistent) depths. When coring hard rocks, all pieces recovered are placed immediately adjacent to each other in the core tray. Samples and descriptions of cores are designated by distance, measured in centimeters from the top of the section to the top and bottom of each sample or interval. By convention, hard rock material recovered from the core catcher is placed below the last section. In sedimentary cores, the core catcher section is treated as a separate section (“CC”). When the only recovered material is in the core catcher, it is placed at the top of the cored interval.

A complete identification number for a sample consists of the following information: expedition, site, hole, core number, core type, section number, piece number (hard rock only), and interval in centimeters measured from the top of the section. For example, a sample identification of “330-U1372A-26R-3 (Piece 5, 40–47 cm)” indicates a 7 cm long sample of Piece 5 taken from the interval between 40 and 47 cm below the top of Section 3 of Core 26 (“R” means this core was taken with the rotary core barrel assembly) in Hole A at Site U1372 during Expedition 330. All cores were drilled with the rotary core barrel assembly during Expedition 330.

Core handling

All cores recovered during Expedition 330 were extracted from the core barrel in plastic liners. These liners were carried from the rig floor to the core processing area on the catwalk outside the core laboratory. Hard rock pieces were pushed to the bottom of the liner, and total rock length was measured by the curator on the catwalk. The length was entered into the database as “created length” using the Sample Master application. This number was used to calculate recovery. The plastic liner was then cut into ~1.5 m sections. Liner caps were placed at both ends

of each section (blue = top end, colorless = bottom end).

The 1.5 m sections were transferred to the core splitting room. For soft sediment, the plastic liners were split lengthwise to expose the core. Hard rock core pieces were slid out of the liners and placed in order in new, clean sections of core liner that had previously been split in half. Pieces having a vertical length greater than the internal (horizontal) diameter of the core liner are considered oriented pieces because they could have rotated only around their vertical axes. Those pieces were immediately marked on the bottom with a red wax pencil to preserve their vertical (upward) orientations. Pieces that were too small to be oriented with certainty were left unmarked. Adjacent but broken core pieces that could be fit together along fractures were curated as single pieces. The structural geologist on shift confirmed the piece matches and corrected any errors. The structural geologist also marked a split line on the pieces, which defined how the pieces should be cut into two equal halves. The aim was to maximize the expression of dipping structures on the cut face of the core while maintaining representative features in both archive and working halves.

Microbiology samples from soft sediment were taken as whole-round samples on the catwalk by cutting a ~5 cm piece of liner from the end of the core, just above the core catcher. For hard rocks, whole-round samples were taken in the splitting room immediately after the core was slid from the liner. The petrologist on duty monitored the microbiology sampling to ensure that no critical petrographic interval was depleted. All microbiology whole-round samples were photographed from both sides.

After microbiology sampling was completed, a plastic spacer was secured with acetone to the split core liner between individual pieces or reconstructed contiguous groups of subpieces (hard rock sections only). These spacers may represent a substantial interval of no recovery. The length of each section of core, including spacers, was then entered as “curated length” into the curation database. Curated length commonly differs by a few to several centimeters from the created length measured on the catwalk (depending on the number of pieces/spacers). Accordingly, the assumed depth of each piece is recalculated in the database on the basis of curated length, and all further observations and measurements are taken against this recalculated depth.

Each section was allowed to equilibrate for ~3 h to ambient room temperature before being scanned using the shipboard Whole-Round Multisensor Logger (see “[Physical properties](#)”). The whole-round core sections were next measured with the Natural

Gamma Radiation Logger (see “[Physical properties](#)”). Each piece of core was then split with a diamond-impregnated saw (for hard rocks) into an archive half and a working half, with the positions of plastic spacers between individual pieces maintained in both halves of the plastic liner. Pieces were numbered sequentially from the top of each section. Separate subpieces within a single piece were assigned the same number but were lettered consecutively (e.g., 1A, 1B, 1C). Pieces were labeled only on the outer cylindrical surfaces of the core. If it was evident that an individual piece had not rotated around a horizontal axis during drilling, an arrow pointing to the top of the section was added to the label. The oriented character of the piece was then recorded in the database using the Sample Master application.

Digital images of the dry, cut faces of the archive halves were captured with the Section Half Imaging Logger (SHIL). Images were taken with a line scan camera at intervals of 20 pixels/mm. Measurements of point magnetic susceptibility and color reflectance were performed with the Section Half Multi-sensor Logger (SHMSL) on the archive halves. This instrument also includes a laser calibration system. Laser data (e.g., locations of core gaps and rubble intervals) were used to aid data filtering of the multi-sensor measurements (see “[Physical properties](#)”).

The archive half of each core (soft sediment or hard rock) was described for lithologic, sedimentologic, magmatic, and volcanic features, and structural observations and alteration characteristics were noted. All observations were recorded in the Laboratory Information Management System (LIMS) database using the descriptive data capture application DESClogik. Specialized templates and spreadsheets were developed for this application by the individual descriptive laboratory groups (for details, see individual disciplinary sections in this chapter).

Finally, digital color close-up images (both from dry and wet surfaces) were taken of particular features of the archive or working halves, as requested by individual scientists. During the crossover between night and day shifts, a sample meeting was held at 1200 h to discuss the sections described and to select key sampling intervals for shipboard analysis. Discrete samples were taken from working halves for shipboard physical property, paleomagnetic, thin section, X-ray diffraction (XRD), and geochemical analyses (e.g., inductively coupled plasma–atomic emission spectroscopy [ICP-AES]), as described in the sections below. Nondestructive X-ray fluorescence (XRF) analyses were also conducted on the working halves using a portable XRF instrument (see details in “[Geochemistry](#)”). Each sample was logged into the Sample Master application by location, sample

type, and intended shipboard study (e.g., thin section, XRD, XRF, etc.). Paleomagnetic measurements with stepwise alternating-field demagnetization were conducted on oriented archive-half pieces (approved by the curator) to guide (and thereby minimize) paleomagnetic discrete sampling of the working halves. The microbiology whole-round samples taken on the catwalk (sediment) or in the splitting room (hard rock) were used both for shipboard and personal postcruise studies (see details in “[Microbiology](#)”). Residual material was returned to the curator and made available for additional shipboard or personal sampling.

Records of all removed samples are kept by the IODP curator. Sampling for personal postcruise research was conducted during several sampling parties over the course of the expedition. At the end of Expedition 330, all cores were transferred from the ship for permanent storage at the IODP Gulf Coast Repository in College Station, Texas (USA).

Sedimentology

The lithology of the sediment recovered during Expedition 330 was primarily determined using observations based on visual (macroscopic) core description, thin sections, and smear slides. In some cases digital core imaging, color reflectance spectrophotometry, and magnetic susceptibility analysis provided complementary discriminative information. The methods employed during this expedition were similar to those used during IODP Expedition 324 (Expedition 324 Scientists, 2010) to Shatsky Rise. Expedition 330 used the DESClogik application to record and upload descriptive data into the LIMS database (see [DESClogik user guide](#)), which was first implemented during IODP Expedition 320T (Expedition 320T Scientists, 2009). Three spreadsheet templates were set up in DESClogik and customized for Expedition 330 before the first core arrived on deck. The spreadsheet templates were used to record macroscopic sedimentologic core descriptions and data from smear slides and thin sections, which were used to quantify the texture and relative abundance of biogenic and nonbiogenic components. The locations of all smear slide and thin section samples taken from each core were recorded in the Sample Master application. Descriptive data uploaded to the LIMS database were also used to produce visual core description (VCD) standard graphic reports.

Visual core descriptions

After descriptions of the cores were uploaded into the central LIMS database, the data were used to produce VCDs, which include a simplified graphical rep-

resentation of the core (per section) with accompanying descriptions of the features observed (Figs. F1, F2). Depending on the type of material drilled, two VCDs were sometimes produced for the same section: one to describe sediment or sedimentary rocks and the other to describe igneous features.

Site, hole, and depth in mbsf, calculated according to the CSF-A depth scale, are given at the top of each VCD, with depth of core sections indicated along the left margin. Observations of the physical description of the core correspond to entries in DESClogik, including grain size, bioturbation intensity, fossils, ichnofossils, lithologic accessories, sedimentary structures, and drilling disturbance. Symbols used in the VCDs are given in Figure F2. Additionally, sedimentary VCDs display magnetic susceptibility, color reflectance, paleontological observations, and the locations of samples taken for shipboard measurements. Section summary text provides a generalized overview of the core section's lithology and features. This summary text and individual columns shown on the VCDs are described below in greater detail, followed by an outline of the lithostratigraphic classification used during Expedition 330.

Section summary

A brief overview of major and minor lithologies present in the section, as well as notable features (e.g., sedimentary structures) and the composition of basalt clasts (if present), is presented in the section summary text field at the top of the VCDs. The summary includes sediment color determined qualitatively using Munsell soil color charts (Munsell Color Company, Inc., 2000). Because sediment color may evolve during drying and subsequent oxidization, color was described shortly after the cores were split and imaged or measured by the SHIL and SHMSL.

Section-half image

The high-resolution scans of each core section (at 20 pixels/mm) made by the SHIL are included to provide a continuous image of the whole section.

Graphic lithology

The lithology of the recovered core is represented on the VCDs by graphic patterns. See Figure F2 for an explanation of patterns used during Expedition 330.

Magnetic susceptibility

When recovery and core length permitted, the magnetic susceptibility of both whole rounds and split sections of the core was measured, which roughly indicates the concentration of magnetic minerals. A filter was applied to remove spurious data related to

gaps between broken pieces of the hard rock cores (see “Physical properties”). Both filtered and raw data are shown on the VCDs.

Color reflectance spectrophotometry

Color reflectance spectrophotometry of visible light (“Reflectance” in the VCDs) was routinely measured on archive halves of sediment (and hard rock) cores using the SHMSL, which was equipped with Ocean-Optics software for analysis of color reflectance data (see details in “Physical properties”). Cores consisting of soft sediment were covered with clear plastic wrap and then placed on the SHMSL. Hard rock sections were run without the protective plastic cover. Measurements were taken at 1 cm spacing. The SHMSL is set to skip empty intervals in the core liner, but it cannot recognize relatively small cracks, disturbed areas of cores, or plastic section dividers. Thus, raw SHMSL data may contain spurious measurements. Therefore, during postprocessing a filter was applied to the reflective data set (see “Physical properties”). Both filtered and unfiltered data are shown on the VCDs.

Grain size

The Grain size column displays sediment grain size as a block chart. The dominant grain size is represented numerically for each lithologic interval using a range of 1–6:

- 1 = clay size (<3.9 μm).
- 2 = silt size (3.9–62.5 μm).
- 3 = very fine to fine sand size (>62.5–250 μm).
- 4 = medium to very coarse sand size (>250 μm –2 mm).
- 5 = granule to cobble size (>2–256 mm).
- 6 = boulder size (>256 mm).

Because the bulk of the sediment observed during Expedition 330 is composed of basalt breccia and volcanic sandstone, the size of detrital grains in coarse-grained sediment was estimated during visual description of the cores by measuring the largest grain size per 10 cm interval. Grains overlapping several intervals were measured only once. Also, the roundness of grains was estimated on the basis of the average roundness of the largest grains in each 10 cm interval for each lithology. Six categories of roundness were defined with the help of a visual comparison chart (Shepard and Young, 1961): very angular, angular, subangular, subrounded, rounded, and well rounded (no measurement of roundness was made for clasts <1 mm). These measurements are not shown on the VCDs but are available in supplementary tables (see SIZE in SEDIMENT in “Supplementary material”) and are displayed in stratigraphic summary figures in each site chapter. The average

maximum grain size of coarse-grained sediments is available in LIMS.

Bioturbation intensity

The degree of bioturbation was determined by observing how intensely the sediments were altered by the action of organisms (Droser and Bottjer, 1986). The following categories were used to describe degree of bioturbation:

- Intense (ichnofabric index 5 and 6): 60%–100% of original bedding disturbed.
- Moderate (ichnofabric index 3 and 4): 10%–60% of original bedding disturbed.
- Minor (ichnofabric index 1 and 2): 0%–10% of original bedding disturbed.

The Bioturbation column was left blank for intervals composed of volcanoclastic sediments.

Fossils/Ichnofossils

Identifiable fossils (or fossil fragments) and trace fossils (ichnofossils) are identified in the Fossils/Ichnofossils column.

Sedimentary structures

Structures resulting from physical sedimentary processes are represented in the Sedimentary structures column. Identified features include laminations and cross-bedding, contacts between sediment of differing lithologies, and any soft-sediment deformation structures.

Lithologic accessories

Some postdepositional features (e.g., ferromanganese encrustations) and grains of interest (e.g., pumice and coated grains) are recorded in the Lithologic accessories column.

Drilling disturbance

The Drilling disturbance column indicates the mode and type of disturbance (e.g., flow-in or fall-in) caused by the drilling process. The degree of disturbance within soft sediment is characterized using the nomenclature of Ocean Drilling Program (ODP) Leg 180 (Taylor, Huchon, Klaus, et al., 2000):

- Slightly disturbed: bedding contacts are slightly deformed.
- Moderately disturbed: bedding contacts have undergone extreme bowing.
- Highly disturbed: bedding is completely deformed as flow-in and other soft stretching and/or compressional shearing structures attributed to coring/drilling.

- Soupy: intervals are water saturated and have lost all aspects of original bedding.

The degree of fracturing within indurated sediments is described using the following categories:

- Slightly fractured: core pieces are in place and broken.
- Moderately fractured: core pieces are in place or partly displaced, but original orientation is preserved or recognizable.
- Highly fractured: core pieces are probably in correct stratigraphic sequence, but original orientation is lost.
- Drilling breccia: core is crushed and broken into many small and angular pieces, with original orientation and stratigraphic position lost.

Age

The nannofossil or foraminiferal zone that defines the age of the sediments was provided by the shipboard biostratigraphers (see “[Paleontology](#)”) and is listed in the Age column.

Samples

The exact positions of samples used for microscopic descriptions (i.e., smear slides and thin sections), biochronological determinations, and shipboard analysis of chemical and physical properties of the sediments are recorded in the Samples column.

Sediment classification

Lithologic names, including sediment composition, degree of lithification, and texture, are based mostly on conventions outlined by Mazzullo et al. (1988) in the ODP sediment classification scheme (Fig. F3). The term “mixed sediment” was not used during Expedition 330 because thin-bedded lithologic variations did not occur. Pelagic sediments are defined as >50% pelagic and neritic components and <50% siliciclastic and volcanoclastic components, with a higher proportion of pelagic than neritic components. Neritic sediments, on the other hand, are defined as >50% pelagic and neritic components and <50% siliciclastic and volcanoclastic components, with a higher proportion of neritic than pelagic components. Siliciclastic sediments are defined as >50% siliciclastic and volcanoclastic components and <50% neritic and pelagic components, with a higher proportion of siliciclastic than volcanoclastic components. Finally, volcanoclastic sediments are defined as >50% siliciclastic and volcanoclastic components and <50% neritic and pelagic components, with a higher proportion of volcanoclastic than siliciclastic components.

The nomenclature includes a principal name based on the composition of the major lithology, preceded by major modifiers (in order of increasing abundance) that refer to components making up at least 25% of the sediments. The principal name is followed by minor modifiers for components forming between 10% and 25% of the sediments, in order of increasing abundance. In clastic deposits, components refer to clasts and do not include the matrix. For example, a well-indurated breccia sample containing 40% basalt, 35% bioclasts, 20% cement, and 5% foraminifers would be described as a “bioclast basalt breccia.” The principal name (breccia, in the preceding example) is displayed in the Graphic lithology column of the VCDs with a general descriptive prefix (e.g., volcanic), whereas major and minor components are available from the LIMS database or section summaries of the VCDs. The term “sandy foraminiferal ooze” is applied to the youngest sediments encountered during Expedition 330, which likely represent a winnowed residue of foraminiferal ooze originally richer in nannofossils.

The subclassification of volcanoclastic sediments followed here differs from the standard ODP classification (Mazzullo et al., 1988) in that we adopted a descriptive (nongenetic) terminology similar to that employed during ODP Leg 197 and Expedition 324 (Shipboard Scientific Party, 2002; Expedition 324 Scientists, 2010). Unless an unequivocally pyroclastic origin for volcanogenic particles could be determined, we simply described deposits composed of these materials as being of volcanic provenance according to the classification scheme for clastic sediments, noting the dominance of volcanic grains (e.g., volcanic sandstone). We followed the clastic textural classification of Wentworth (1922) to separate the various volcanic sediment types and sedimentary rocks (according to grain size) into volcanic gravel (>2 mm), volcanic sand (2 mm–62.5 μm), volcanic silt (62.5–3.9 μm), and volcanic clay (<3.9 μm). For coarse-grained, poorly sorted volcanoclastic sediments rich in basalt clasts, such as those produced by gravity currents, we applied the terms “basalt breccia” (angular clasts) or “basalt conglomerate” (rounded clasts) and used lithologic or structural modifiers for further description.

Where evidence for a pyroclastic origin was compelling, we adopted the classification scheme of Fisher and Schmincke (1984). In these instances we used the grain-size terms “volcanic blocks” (>64 mm), “lapilli/lapillistone” (2–64 mm), and “ash/tuff” (<2 mm). The term “hyaloclastite” was used for vitroclastic (i.e., glassy) materials produced by the interaction of water and hot magma or lava (Fisher and Schmincke, 1984). The term “peperite” was applied

to a rock formed essentially in situ by disintegration of magma intruding and mingling with unconsolidated or poorly consolidated, typically wet, sediments. The term also refers to similar mixtures generated by the same processes operating at the contacts of lavas and other hot volcanoclastic deposits with such sediments (Skilling et al., 2002).

Smear slide observation

Smear slides are useful for identifying and reporting basic sediment attributes (texture and composition) in soft sediments, but the results are not quantitative. Similar to the procedure applied during IODP Expedition 315, we estimated the abundances of biogenic, volcanoclastic, and siliciclastic constituents with the help of a visual comparison chart (Rothwell, 1989). Errors can be large, however, especially for fine silt- and clay-size fractions, and reproducibility among different sedimentologists is expected to be poor. Smear slide analysis also tends to underestimate the amount of sand-size grains because they are difficult to incorporate evenly onto the slide. Thus, it would be misleading to report values as absolute percentages. Instead, our descriptive results are tabulated as visual percentage estimates in the LIMS database, with values grouped into the following broad range of categories:

- D = dominant (>50%).
- A = abundant (>20%–50%).
- C = common (>5%–20%).
- P = present (>1%–5%).
- R = rare (0.1%–1%).
- T = trace (<0.1%).

Semiquantitative X-ray fluorescence analysis

Semiquantitative XRF analysis using a portable XRF spectrometer was applied for some sedimentary intervals, such as ferromanganese encrustation and phosphatized limestone (see “[Geochemistry](#)”; see also XL3_EVAL.PDF in XRF in “[Supplementary material](#)”).

Paleontology

Preliminary age assignments were based on calcareous microfossils (nannofossils and planktonic foraminifers) in core catcher samples, with additional samples from core sections, as required. The Quaternary, Neogene, and Paleogene timescale constructed for IODP Expedition 320/321 was used for this study (Expedition 320/321 Scientists, 2010). Biostratigraphic events were correlated to the geomagnetic polarity timescale, which is based on a composite of

several timescales (Cande and Kent, 1995; Lourens et al., 2004; Pälike et al., 2006) (Fig. F4A–F4D). The timescales of Gradstein et al. (1995) and Channell et al. (1995) were applied for the early Paleocene (older than 60 Ma) and Late Cretaceous (Fig. F4E). Preservation, abundance, and zonal assignments for each microfossil group were entered into the LIMS database via DESClogik software.

Calcareous nannofossils

Calcareous nannofossils were examined in smear slides prepared with standard microscope slides and coverslips and mounted with Norland optical adhesive. Slides were observed using standard light microscope techniques on a Zeiss Axiophot with crossed polarizers and transmitted light at 1000× magnification. Following the methods used during ODP Leg 144, the zonation of Okada and Bukry (1980) was used during Expedition 330 for Cenozoic calcareous nannofossils (Table T1, modified from Expedition 320/321 Scientists, 2010). In the upper Cretaceous the zonation of Sissingh (1977) was applied (Table T2, modified from Shipboard Scientific Party, 2004). Taxonomy follows that of Bowen (1998) and Perch-Nielsen (1985), where full taxonomic lists can be found.

Estimates of the abundance of calcareous nannofossils were determined as follows:

- D = dominant (>100 specimens per field of view).
- A = abundant (>10–100 specimens per field of view).
- C = common (1–10 specimens per field of view).
- F = few (1 specimen per 1–10 fields of view).
- R = rare (<1 specimen per 10 fields of view).
- B = barren.

Preservation of calcareous nannofossils was classified as follows:

- VG = very good (no evidence of dissolution and/or recrystallization, no alteration of primary morphological characteristics, and all specimens identifiable to the species level).
- G = good (little or no evidence of dissolution and/or recrystallization, primary morphological characteristics only slightly altered, and specimens identifiable to the species level).
- M = moderate (some etching and/or recrystallization, primary morphological characteristics somewhat altered, and most specimens identifiable to the species level).
- P = poor (severe etching or overgrowth, primary morphological characteristics largely destroyed, fragmentation has occurred, and

specimens often unidentifiable at the species and/or generic level).

Planktonic foraminifers

The planktonic foraminiferal zonal scheme used for the Cenozoic follows Berggren et al. (1995), except for the Eocene and Oligocene, which are based on Berggren and Pearson (2005). The mid–late Paleogene, Neogene, and Quaternary age estimates (0–60 Ma) used in this study follow those used during Expedition 320/321 (Expedition 320/321 Scientists, 2010). Those ages and sources are listed in Table T3. The zonation used for Cretaceous planktonic foraminifers is based on the zonal schemes of Caron (1985), Sliter (1989), and Robaszynski and Caron (1995). The early Paleogene (>60 Ma) and Late Cretaceous age estimates, obtained from Erba et al. (1995), Bralower et al. (1997), and Premoli Silva and Sliter (1999), are based on those used during ODP Leg 207 (Shipboard Scientific Party, 2004) (Tables T3, T4).

Cenozoic taxonomic concepts used selectively follow those of Kennett and Srinivasan (1983), Bolli and Saunders (1985), Toumarkine and Luterbacher (1985), Loeblich and Tappan (1988), Spezzaferri and Premoli Silva (1991), Chaisson and Leckie (1993), Leckie et al. (1993), Spezzaferri (1994), Pearson (1995), Chaisson and Pearson (1997), Pearson and Chaisson (1997), and Pearson et al. (2006). Cretaceous taxonomic concepts used are based on Robaszynski and Caron (1979), Robaszynski et al. (1984), Caron (1985), Nederbragt (1991), and Petrizzo (2000).

Foraminifers from ooze were spray-washed over a 63 µm sieve. Semilithified ooze and chalk were first partly fragmented by hand and then soaked in a 3% solution of hydrogen peroxide (H₂O₂) before washing. Hard chalk and limestone were pounded with a hammer into pea-size fragments and boiled on a hot plate for 1–2 min in a 3% H₂O₂ solution. Species identification for planktonic foraminifers was made on >250 µm and >150 µm size fractions for the Neogene and Paleogene–Cretaceous, respectively.

The following group abundance categories were estimated from visual examination of the dried sample for foraminiferal group abundance:

- A = abundant (>50%).
- C = common (>25%–50%).
- F = few (>10%–25%).
- R = rare (1%–10%).
- T = trace (only a few broken specimens).
- B = barren (no specimens).

The following species abundance categories were used for foraminiferal species abundance:

- D = dominant (>30%).

- A = abundant (>10%–30%).
 F = few (>5%–10%).
 R = rare (1%–5%).
 P = present (<1%).

The preservation status of planktonic foraminifers was estimated as follows:

- VG = very good (no evidence of overgrowth, dissolution, or abrasion).
 G = good (little evidence of overgrowth, dissolution, or abrasion).
 M = moderate (calcite overgrowth, dissolution, or abrasion are common but minor).
 P = poor (substantial overgrowth, dissolution, or abrasion).

In many cases during Expedition 330, foraminifers from consolidated sediments were also examined in thin section. Species identification was made only for axially sectioned specimens, whereas general morphologies were described for all other individuals. Group abundance, species abundance, and preservation were not recorded for thin section analyses.

Igneous petrology and volcanology

The procedures for core description outlined here are essentially those used during Expedition 324 to Shatsky Rise (Expedition 324 Scientists, 2010). The goal of our shipboard studies was to produce an integrated picture of each drill site's style of volcanism and environmental setting. This goal was achieved by systematically describing rocks and identifying key effusive, volcanoclastic, and igneous textures known to be diagnostic of specific modern physical volcanic processes. Physical description of the volcanic rocks and deposits recovered during Expedition 330 required a multistage process. First, lithologic unit boundaries were defined by visual identification of actual lithologic contacts or by inference of such contacts using observed changes in composition (e.g., phenocryst assemblages), volcanic characteristics, or volcanoclastic features. Then, lithology, phenocrysts, lithologic variation, and characteristic igneous textures and vesicle distributions were described. Finally, these macroscopic observations were combined with those from detailed thin section petrographic studies of key igneous units.

Physical characteristics of volcanic units

Subaerial lava eruptions

A'a lava flows

A'a flows are characterized by angular, spinose clinker at both flow tops and bottoms, in contrast to pa-

hoehoe and pillow flows, which are often characterized by smooth surfaces and clear contacts between successive or adjacent units. Internal disruption during emplacement permits efficient degassing, and the crust, core, and base of *a'a* flows are typically sparsely vesicular or nonvesicular. Transitional flow types (e.g., rubble, slab, or toothpaste pahoehoe; Guilbaud et al., 2005) show some of the characteristics of both pahoehoe- and *a'a*-type flows.

Pahoehoe lava flows

Pahoehoe flows are usually vesicular, often highly so, and can exhibit bulk porosities in excess of 20 vol% (typical range = 20–60 vol%). Thin pahoehoe lobes (<0.5–1 m) are often vesicular throughout and exhibit gradual coarsening in vesicle size from the lobe margins toward the interior (Wilmoth and Walker, 1993). During development of subaerial pahoehoe lava fields, gas bubbles can frequently become trapped and entrained in the magma body as it cools from both above and below. Thus, thicker inflated pahoehoe lobes, such as those documented in continental flood basalt provinces, are often characterized by a threefold structure of vesicular upper crust, dense core, and thinner vesicular lower crust (Aubele et al., 1988; Thordarson and Self, 1998). Very close morphological similarity exists between pahoehoe lava formed on land and pillow lava formed under water, though the former typically lacks, or else has only relatively thin, glassy rinds (i.e., glassy surface selvages).

Subaqueous lava flows

Subaqueous lava flows and hyaloclastite associations have been documented where flows from land-based eruptions entered water (e.g., into seas or freshwater lakes) or else erupted in shallow-submarine situations (e.g., ongoing eruption from Pu'u O'o, Hawaii; Surtsey eruptions of 1963–1967; and around the coasts of the Azores). On entering water or soft unconsolidated sediments, the eruptive style changes fundamentally, and depending on local conditions advancement of the lava front typically generates pillow basalt, hyaloclastites, or peperites (or any combination of these three). Hyaloclastites and peperites are volcanoclastic sediments that form by quench fragmentation (Carlisle, 1963). Pillow basalts are a common product of these environments and can usually be distinguished from pahoehoe flows by their much thicker glassy rinds (a consequence of more efficient aqueous quenching) and by the presence of lacustrine/marine sediments preserved between the pillows. However, although less frequently documented, larger subaqueous flows may also be massive and sheetlike if the local flow rate is high

enough, as determined by slope and eruption rate (Walker, 1992; Gregg and Fink, 1995).

Submarine lava eruptions

Pillow lava flows

Pillow lavas are subaqueous extrusions resulting from individual budding, inflation, and separation of lava pods from point sources along the advancing lava front. They can accumulate in a variety of styles depending on effusion rate, number of point sources, and internal plumbing architectures within the growing volcanic edifice. However, pillow lavas typically consist of discrete subrounded units of relatively small size (~0.2–1.0 m diameter). Characteristically, their exteriors are entirely bounded by glassy rinds as a result of rapid cooling, and their interiors typically display internally radiating vesicle and joint patterns.

Lobate lava flows

Larger lobate flows or flow lobes (~1–2 m diameter) can also develop by the same endogenous inflation process as pillow lava flows. Although these extrusions broadly resemble pillow lavas, they differ in that they have massive, coarser grained, and sparsely vesicular cores, often with pipe vesicle domains. Because their larger size permits a slower rate of cooling, these inflation units are characterized by more effective degassing and maturation of internal vesicle patterns. Accordingly, vesicle zoning is more concentrated in the upper regions of the inflation unit and often occurs as a series of vesicle bands that develops through the inward migration of the cooling front. By contrast, the lower part of the inflation unit typically contains either sparse, poorly defined vesicle banding or teardrop-shaped vesicles at, or just above, the basal chill zone. Rather than being spherical or subspherical, these massive inflation units tend to have flattened, oblate, or tubular shapes and are most probably generated as a series of interconnected, semiadjacent inflation units fed simultaneously by internal plumbing. Their size and morphology are considered to be indicative of higher effusion rates than those that generate pillow lavas. Individual units can cover an area of several square meters (or significantly more where adjacent units merge either through internal plumbing or as a result of rupture and coalescence). In those instances where they merge into a single entity, they appear as a lava flow displaying a dominantly botryoidal surface morphology. Recognizing lobate flows in drill core is often very difficult or impossible, especially in the thick volcanoclastic successions drilled during Expedition 330. The terms “lava fragment” or “flow lobe” were used for >30 cm thick continuous intervals of basalt

when features diagnostic of lobate flows were lacking.

Massive basaltic lava flows

Massive basaltic lava flows form thick (several meters or more), laterally extensive sheetlike units (van Andel and Ballard, 1979). They have a variety of surface features generated by deformation and disturbance of the solidifying lava crust while in a plastic/semi-plastic state. In dimension and internal features they can resemble larger subaerially erupted flows. This type of flow may be fed by lava tubes and develop by internal inflation or marginal budding. These flows often have texturally uniform massive cores as thick as several meters, are characterized by sparse vesicle layering, or have vertical vesicle pipes containing late-stage melt segregation material. Massive or sheetlike flows may be a response to particularly high effusion rates or local slope and other controlling topographic conditions. These unit types have been called “sheet flows” in previous ODP and IODP reports, although this term implies a lateral extent that cannot be determined from core alone. Nevertheless, where recovered, these units are significantly thicker than the normal (~0.2–2 m) dimensions of pillow lava or lobate flows observed in drill cores.

Volcanoclastic deposits

Volcanoclastic deposits include a range of materials from rubbly, in situ volcanic debris to resedimented material such as volcanic sand and gravel. Volcanic material of all sizes may be a direct product of eruptive processes (pyroclastic) or an accumulation of processes involving transport, sorting, and deposition (epiclastic). Pyroclastic activity includes hydrovolcanic deposits formed by explosive interaction between magma and water, as well as nonexplosive quench fragmentation processes (e.g., hyaloclastite and peperite).

Hyaloclastite

Hyaloclastite literally means “glass-fragment rock” and includes all glassy fragmental debris formed by eruptions involving water. Environments of hyaloclastite production relevant to the Louisville Seamounts may include shallow-water phreatomagmatic eruptions when the seamounts were emergent volcanic islands and, most probably, volcanoclastic materials associated with the development and advancement of submarine lavas at greater water depths (Clague et al., 2009). Phreatomagmatic conditions can result in the fragmentation of gas bubbles inflated by steam, producing thick layers of glass shards that may be sent into subaerial trajectories or else form suspended plumes within the water col-

umn. In either case, they then settle upon the surrounding land or seafloor surface (i.e., on newly formed volcanic material) or are transported and re-deposited elsewhere. Depending on the nature of the eruption, welded and unwelded volcanic rubble and breccia may also occur in these environments (Fisher and Schmincke, 1984). Submarine lavas are almost invariably associated with hyaloclastites and a variety of other fragmental volcanic debris, including breccia (Staudigel and Schmincke, 1984; Batiza and White, 2000). Hyaloclastite is common on seamounts, where it may be the product of cooling contraction granulation and surficial spalling of lava flows. Seamounts are also characterized by volcanic breccia and are commonly associated with mass debris flows, especially where the eruption occurs on significant seafloor topography.

Peperite

Peperite is a distinct volcanic sediment facies occurring where subaqueous basaltic lava flows interact with unconsolidated sediment as they erupt into water bodies on land or, more commonly, on the seafloor (Skilling et al., 2002). The mingling of basaltic lava and wet sediment produces distinct volcanic textures resulting from the physical interaction of lava and sediment (entrainment, baking, chilling, etc.), as well as physical and chemical fragmentation and alteration through steam-rock interaction during flash heating of the water. Common features include quenched lava flow margins of basaltic clasts surrounded by sediment, as well as basaltic clasts with a variety of fragment morphologies, including fluidal (e.g., where fragments remained plastic enough to deform after deposition) or jigsaw-fit (e.g., where fragments cracked apart in situ, forming blocky peperite). The presence and texture of peperite may provide important information regarding the nature of the eruptive environment. Importantly, the occurrence of peperite provides evidence that the volcanism and affected sedimentary environment existed contemporaneously.

Other lava-sediment interactions include features involving the mixing or mingling of molten or plastic lava with sediment (e.g., where lava injects or intrudes into a substrate). In some instances, there is a lack of bedding or lamination in sediment adjacent to pillow lavas or the material surrounding lava injections. A likely explanation is fluidization of the fine-grained sediment, attributable to flash heating and vaporization of sediment pore water during emplacement of the pillow lava (Kokelaar, 1982). Such momentary fluidization causes sediment reconstitution, localized transport, and redistribution and

hence the destruction of any inherent bedding structures.

Definition of lithologic units and volcanic successions

In recording our observations of the drill core, it was important to avoid nomenclature or terminologies that imply particular styles of basaltic volcanism. Most lava type classifications are based on field observations that consider both lateral and vertical variations of eruptive units and their stacking relationships. Such refined classifications are neither realistic nor justifiable from core observation alone and can only become achievable when additional petrographic, geochemical, or downhole logging data are available. In most instances, only the smaller volcanic unit divisions (i.e., individual cooling units) can be identified in core material, so these are necessarily the basic units of description.

Descriptive nomenclature

Volcanic succession

To aid efficient core description and enable later collation of the observed volcanic elements into volcanically meaningful successions, we adopted a simple twofold numerical hierarchy. First, to define lithologic units we looked for lava contacts, chilled margins or identifiable flow tops, changes in phenocryst populations, vesicle distributions, and intercalated volcanoclastic or sedimentary horizons. When considered together, these features typically define the key volcanic cooling, inflation, and depositional units of various sizes and the scales within the eruptive succession. Lithologic units are given consecutive downhole Arabic numerals (i.e., lithologic Units 1, 2, 3, etc.), irrespective of whether they are pillows, massive flows, volcanoclastic deposits, or igneous intrusions. This procedure, therefore, provides a non-genetic cataloging system.

Stratigraphic units were defined where successions of consecutive cooling, inflation, or depositional units of similar or shared evolutionary characteristics could be identified, usually on the basis of phenocryst type. In effect, these stratigraphic units combine similar types of eruptive products and provide a first step toward considering the volcanic stratigraphy in terms of packages of petrologically and genetically related lithologic units and, ultimately, the evolving volcanism. These packages are given consecutive downhole Roman numerals (e.g., stratigraphic Units III, IV, V, etc.) that follow consecutively from the overlying sedimentary units (e.g., Units I and II). Although we made every effort to en-

sure that the identified stratigraphic unit boundaries reflect individual lava packages or eruptive units, the term “boundary” should not be considered synonymous with an individual lava flow or single eruptive event but rather as indicating a division of core into elements or sections displaying broadly similar volcanic and petrologic characteristics.

The best evidence for dividing core into lithologic units is the presence of flow/flow contacts. Unfortunately, these are not always preserved in low-recovery sections. Alternatively, the presence of glassy material or finer grained chill zones can be a useful proxy for determining the presence or estimating the position of lithologic unit boundaries. However, grain-size changes close to flow tops are often no greater than those within inflated lava flows, so interpretation of grain-size changes in core can prove difficult. Changes in vesiculation that occur through inflation or cooling units of all sizes are of particular use in sections of poor core recovery. To identify and estimate the position of lithologic unit boundaries using this method we paid special attention to vesiculation characteristics by measuring, estimating, and otherwise recording (1) the percentage volume of vesicles, (2) their modal size range, (3) their shape and sphericity, and (4) changes in vesicle size (i.e., fining- or coarsening-upward) at intervals appropriate for the variability shown in the core (typically 10–100 cm intervals). The volume fraction of vesicles within the unit or section under consideration, together with the modal shape and sphericity of vesicle populations, was estimated using appropriate comparison charts similar to those used by sedimentologists and derived from the Wentworth (1922) classification scheme (Fig. F5). Maximum and modal sizes were determined using a hand lens with a sub-millimeter graticule. It proved impractical to measure the minimum size because this was always at or below the limit of visual resolution.

Lithology

Lithologic descriptions followed accepted conventions. Porphyritic basaltic rocks were named according to major phenocryst phase(s), but only where the total abundance of phenocrysts was >1% (e.g., plagioclase-phyric basalt or olivine-augite-phyric basalt). Phenocryst phases were always listed in order of decreasing abundance so that the dominant phase was listed first. The term “phenocryst” was used for any crystal that was (1) significantly (typically five times) larger than the average size of the groundmass crystals, (2) >1 mm, and (3) euhedral or subhedral. The term “microphenocryst” was used for crystals larger than the modal groundmass grain size but smaller than 1 mm. Where macroscopic observation

was possible, these microphenocrysts were also described in the DESClogik application under a suitable heading in the phenocryst table. Aphyric rocks were not assigned any mineralogical modifier.

Volcaniclastic deposits

We used “volcaniclastic” as a nongenetic term for any fragmental aggregate of volcanic parentage containing >60% volcaniclastic grains and <40% other types of clastic or biogenic material. This definition is necessarily broader than that for pyroclastic deposits because the term “pyroclastic” strictly applies only to products of explosive volcanic activity, including hydroclastic deposits formed by explosive interaction between magma and water/sediment and nonexplosive quench fragmentation (i.e., hyaloclastite and peperite). Our adopted definition may also include the volcanic detritus produced by erosion or transport of volcanic material (i.e., epiclastic sediment). Accordingly, the term “volcaniclastic” does not necessarily imply active volcanism at the time of deposition.

In fragmental lava facies we documented volcaniclastic textures using standard sedimentologic techniques (e.g., clast versus matrix modal proportions, clast size, shape, sorting, and lithology). Of particular interest was the presence (or absence) of features diagnostic of viscous or quench fragmentation while the lava was hot. These include clasts engulfing fragments of other (earlier) clasts, welding, glassy margins surrounding the clasts, extensions of the interior of the flow into the breccia, entrained clasts within the interior of the flow, and the presence of basal breccia. We used changes in clast morphology and crystallinity as well as changes in vesicle abundance and shape to identify clast types within breccia.

Our subclassification of volcaniclastic sediment differs from the standard ODP classification (Mazzullo et al., 1988) in that we adopted a descriptive (nongenetic) terminology similar to that employed during Leg 197 (Shipboard Scientific Party, 2002). We simply described volcaniclastic sediment according to the classification scheme for clastic sediment, noting the dominance of volcanic grains. We followed the clastic textural classification of Wentworth (1922) to separate the various volcanic sediment types and sedimentary rocks (according to modal grain size) into the following:

- Volcanic gravel (>2–8 mm; equivalent to fine gravel on the Wentworth scale),
- Volcanic sand (>0.0625–2 mm),
- Volcanic silt (0.0039–0.0625 mm), and
- Volcanic clay (<0.0039 mm).

Volcaniclastic rocks with grain sizes in the silt and clay ranges were not found in any of the basement successions drilled during Expedition 330. For coarser-grained (modal grain size >8 mm) volcaniclastic rocks with angular clasts we applied the term “breccia” and used lithologic or genetic modifiers (e.g., volcanic, basalt, and hyaloclastite) for further description. Thus, we divided the volcaniclastic rocks into volcanic sandstone (0.0625–2 mm), gravel-size volcanic breccia (>2–8 mm), and volcanic breccia (>8 mm). For simplicity we used the expressions “volcanic sand” and “volcanic gravel” on the stratigraphic columns. We further classified volcaniclastic rocks by adding additional modifiers to the designated principal name. Relative proportions of vitric (glass), crystal (mineral), and lithic (rock fragment) components (where the proportion exceeds 5%) were used to determine these modifiers. For example, a volcanic sandstone composed of 75% glass, 5% feldspar crystals, and 20% lithic fragments would be named “vitric-lithic volcanic sandstone.”

Core and thin section descriptions

The first step in describing the recovered core was identifying unit boundaries on the basis of lithologic changes, color, grain size, the presence of volcaniclastic or sedimentary intercalations, volcanological features (e.g., presence of contacts or chilled margins), vesicle distribution patterns, changes in primary mineralogy (occurrence and abundance of plagioclase, augite, and olivine), structure, alteration, and veins. Unit boundaries of volcanic rocks were chosen to reflect different volcanic cooling or volcaniclastic units. In some cases, limited recovery required interpolation to position unit boundaries. Of fundamental importance to core interpretation was the additional use of digital image printouts of the archive core halves. During core processing, these printouts are generated from the archive half of the split core using the digital SHIL. Annotation of these printouts provides a working record onto which observation notes, sketches of key features, or indication of shipboard sampling or analytical requirements can easily be made. This visual record also proved invaluable during the preparation of site reports. These handwritten records were later scanned and are provided as supplementary data to this volume (see SCANS in “[Supplementary material](#)”).

Macroscopic visual core description

We used the DESClogik application to document each section of the igneous rock cores and upload these descriptions to the LIMS database (see [DESClogik user guide](#)). For consistency, our procedures and database templates closely followed the meth-

ods for core descriptions from recent ODP and IODP volcanic basement expeditions, in particular those to the Hawaii-Emperor Seamounts (Leg 197; Shipboard Scientific Party, 2002) and Shatsky Rise (Expedition 324; Expedition 324 Scientists, 2010).

VCD standard graphic reports were generated from data downloaded from the LIMS database to summarize each core section. An example VCD for igneous rocks is shown in Figure F6. The VCD readouts display the following items:

- Depth in mbsf;
- Scale for core section length (0–150 cm, or as appropriate);
- Sample piece number;
- Scanned digital image of the archive half;
- Upward-pointing arrow indicating oriented pieces of core;
- Sample type and position of intervals selected for different types of shipboard analytical studies;
- Lithologic unit number;
- Symbolized structural information;
- Structural measurements of dip direction and dip angle;
- Block chart displaying the percent vesicularity;
- Stacked line chart displaying phenocryst percentage for plagioclase (pl; red line), olivine (ol; green line), and pyroxene (px; blue line);
- Block chart displaying variation in crystal size of modal groundmass (in millimeters) and indicating presence of fresh glass (f), slightly altered glass (s), moderately altered glass (m), or completely altered glass (a);
- Ornament depicting alteration intensity;
- Chart displaying point magnetic susceptibility, including both raw (shaded) and filtered (solid) data; and
- Chart displaying color reflectance, with total reflectance (L*), red (a*), and blue (b*) data arranged side by side, again showing both raw (shaded) and filtered (solid) data.

Additionally, the VCDs contain written descriptions to accompany the schematic representation of the core sections. This information includes the following:

- Expedition, site, hole, core and core type, section number, and top of core section (measured according to the CSF-A depth scale, which directly corresponds to mbsf; see “[Procedures](#)”), shown at top of VCD;
- Unit number(s) (numbered consecutively down-hole) and piece numbers belonging to unit (and

on which piece, or pieces, the description was based);

- Lithology, rock description, and name;
- Volcanic description based on type of (partial) unit (e.g., pillow lava, massive flow);
- Rock texture: aphyric (<1% phenocrysts), sparsely phyric (1%–2% phenocrysts), moderately phyric (>2%–10% phenocrysts), or highly phyric (>10% phenocrysts);
- Color determined on dry rock surfaces;
- Phenocryst percentage and type based on minerals identifiable by eye, hand lens, or binocular microscope;
- Groundmass grain size and texture: glassy, aphanitic (crystalline, but individual grains not discernible with a hand lens), fine grained (<1 mm), medium grained (1–5 mm), or coarse grained (>5 mm);
- Vesicle percentage by volume;
- Upper and lower unit contact relations and boundaries, as based on physical changes observed in retrieved core material (e.g., presence of chilled margins, changes in vesicularity, and alteration), and information regarding their position within the section. “Not recovered” was entered where no direct contact was recovered (if igneous contact was inferred using proxy observations such as a chilled margin or changes in vesicularity); and
- Alteration and veins (see “[Alteration petrology](#)”) and structural features (described in “[Structural geology](#)”).

Microscopic visual core description

Thin section analyses of sampled core intervals were used to complement and refine macroscopic core observations. Typically, one thin section was examined and logged per defined lithologic unit, although this was not possible in volcanoclastic units with frequent alternations of massive and brecciated units. As far as was practically possible, the same terminology and nomenclature hierarchy employed for visual core compositional descriptions were also used for thin section descriptions. The textural terms used are those defined by MacKenzie et al. (1982). Phenocryst assemblages (and their modal percentages and sizes), groundmass, and alteration phases were determined, and textural descriptions were constructed. All observations were entered into the LIMS database via a special DESClogik thin section template. Downloaded tabular reports of all igneous thin section descriptions can be found in “[Core descriptions.](#)”

Assessing the probability that igneous rocks have remained in situ since emplacement within the volcanic seamount structures

Determining the paleolatitude of the Louisville Seamounts was one of the primary objectives of Expedition 330, so it was essential that a large number of individual in situ igneous cooling units were collected at each site. It was therefore important to establish that (1) these units were correctly identified and (2) that the identified intervals had not rotated about a horizontal axis since they acquired their remanent magnetization. Both of these facts are easy to establish in the case of subaerial lava flows, but problems arise when the recovered units form part of a submarine succession. Individual pillows and flow lobes may be identified where recovery is high, but establishing that they had retained their cooling orientation was less straightforward. For example, individual lava lobes or pillows in an eruptive stack will probably have remained in situ, but an isolated pillow or small lobe in a volcanoclastic sequence will probably have cooled and rolled before coming to rest. It was therefore necessary to construct a set of objective criteria with which to assess the probability of an individual igneous lithologic unit having remained in situ after emplacement. These criteria, set out below, allowed us to assign to each cooling unit (our lithologic units) of lava or intrusive igneous rock in the core a number (0, 1, 2, 3) or NA (not applicable) that we call the in situ confidence index:

- 0 = unlikely to be in situ (individual isolated pieces <30 cm long; any piece <30 cm long separated from its neighbor by a selvage of hyaloclastite or breccia; any section of core of any length where there is compelling evidence that it is not in situ, such as large boulders in a conglomerate).
- 1 = could be in situ (discrete lithologically similar pieces that form continuous sections of 30 cm to 1 m; continuity is broken if traces of hyaloclastite or breccia are identified between individual pieces).
- 2 = probably in situ (discrete lithologically similar pieces that extend over recovered intervals of >1 m, provided there are no traces of hyaloclastite or breccia between any individual pieces; core recovery need not be high).
- 3 = highly likely to be in situ (must satisfy at least one of the following requirements: [1] lava flows with identified flow tops or bottoms; [2] dikes or sills with at least one clearly identified margin; [3] recovered intervals of core >1 m with pieces that clearly belong together and where core recovery over the interval extending from above to below

the unit was >60%; [4] pieces form part of an eruptive lobe or pillow stack within a continuous core showing individual cooling units in contact with each other; [5] clear vertical pipe vesicles or consistent horizontal magnetic foliation).

NA = not applicable (applied during Expedition 330 to volcanoclastic deposits made of clasts that possibly did not retain their orientation since cooling, although the deposit as a whole may have acquired the ambient magnetic field through alteration processes soon after eruption).

Alteration petrology

Alteration characteristics were described from visual observation of the archive halves, and the general degree of alteration is presented on the igneous VCDs (see “[Igneous petrology and volcanology](#)”). Petrographic description of thin sections and X-ray diffraction (XRD) analyses (bulk rock, veins, vesicles, and void infillings) were carried out on samples from the working halves.

All igneous rocks recovered during Expedition 330 underwent some degree of alteration or weathering in subaerial, shallow-subaqueous, hydrothermal, or deep-marine environments. Primary igneous phases such as glass and olivine have therefore often been altered to a variety of secondary phases, including clays, zeolites, carbonates, and iron oxides that were identified and described by the alteration petrology group. Methods used include hand sample descriptions, inspection of polished thin sections, and XRD spectroscopy. Alteration mineralogy was defined by color, habit and shape, association with primary minerals (if distinguishable), and hardness. Complications arise in the identification and description of the secondary phases because many minerals produced in the different alteration environments (e.g., low-temperature submarine alteration and subaerial weathering) are visually similar and indistinguishable in the cores. Also, some cores may have experienced multiple alteration events (e.g., subaerial weathering overprinted by seafloor alteration), producing a more complex mineral assemblage. Hence the identification of some alteration phases remains tentative, pending more detailed shore-based XRD studies and electron microprobe analyses.

Core logging

The types, forms, and distribution of secondary minerals were determined during core description, as was the abundance of veins and vesicles and their re-

lated infilling material. Descriptions were based mostly on hand specimen observations of cut, dry, and wet surfaces. These observations provided information on the alteration of primary igneous features, including the alteration of phenocrysts and groundmass minerals and volcanic glass. Information was recorded on the extent of replacement of igneous minerals and groundmass by secondary minerals and, where possible, the nature and approximate modes of secondary mineral assemblages.

The secondary mineral assemblages were largely composed of clay minerals that were difficult to identify macroscopically; therefore, a general descriptive term such as “brown clay” was used for these cores. Similarly, the specific zeolite and carbonate minerals are not generally distinguished, except when their crystal morphology allowed unequivocal identification. Visual estimates of alteration degree, type, color, and textures (e.g., halos and patches); abundance (%) of minerals filling veins and vesicles; and the proportion of altered groundmass, volcanic glass, and phenocrysts were recorded.

The degree of alteration for groundmass and glass is defined and reported graphically on the VCDs according to various ranges of intensity (Fig. F7):

Fresh = <2 vol%.

Slight = 2–10 vol%.

Moderate = >10–50 vol%.

High = >50–95 vol%.

Complete = >95–100 vol%.

Note that for some intervals, especially those containing clasts with different degrees of alteration, mixed alterations are defined.

Alteration color was defined using Munsell Soil Color Charts (Munsell Color Company, Inc., 1994) and converted to a more intuitive color name (e.g., very dark gray, greenish gray, etc.). Quantification of individual mineral modes was estimated by investigating the archive halves under a binocular microscope or using hand lenses with graticules of 0.1 mm. A distinction was made between overprinting alteration assemblages and assemblages localized by preexisting lithology changes.

During Expedition 330, veins were first recorded by the shipboard structural geologists to identify the location, orientation, and width of the veins; alteration petrologists then recorded the mineralogy of veins and vein halos. All features were recorded in DESClogik (see below) using a series of codes (Fig. F8) for vein shape (straight, sigmoidal, irregular, pull-apart, and fault vein), connectivity (isolated, single, branched, and network), texture (massive, cross fiber, slip fiber, vuggy, and polycrystalline),

structure (simple, composite, banded, haloed, and intravenous), and geometry (en echelon, ribbon, and cross fractures). Likewise, vesicles were first recorded by the igneous petrology group for shape, abundance, size, and density, after which the infilling minerals were identified by the alteration petrologists. Voids were described by the alteration petrologists in terms of size, abundance, and infilling minerals.

DESClogik: descriptive data capture

During Expedition 330 the DESClogik application (see [DESClogik user guide](#)) was used to enter data from visual core description, thin section description, and compilation into the LIMS database. Before drilling operations began, spreadsheet templates were constructed and customized in DESClogik to record alteration characteristics of Expedition 330. These templates were based on the methods and observations of ODP Leg 192 and IODP Expeditions 304/305 and 324 (Mahoney, Fitton, Wallace, et al., 2001; Blackman, Ildefonse, John, Ohara, Miller, MacLeod, and the Expedition 304/305 Scientists, 2006; Sager, Sano, Geldmacher, and the Expedition 324 Scientists, 2010). A first template was used to record general alteration characteristics observed in the igneous rocks (first column of Table T5), and a second template, shared with the igneous petrologists and structural geologists, was used to record alteration characteristics of veins and vesicles (second and third columns of Table T5).

Thin section description

Thin section descriptions were also recorded using DESClogik and subsequently uploaded to the LIMS database. Secondary mineral assemblages and replacement relations to primary phases were described, as were secondary modes. Mineralogy of veins and vesicles, as well as cement and voids present in basaltic breccia, was also reported. Modal estimates of secondary minerals allowed characterization of alteration intensity. Total alteration (%) was calculated using the modal proportions of phenocrysts and groundmass minerals and their respective percentages of alteration.

X-ray diffraction

Mineral identification was aided by XRD analyses using a Bruker D-4 Endeavor diffractometer with a Vantec-1 detector using nickel-filtered $\text{CuK}\alpha$ radiation. Instrument conditions were as follows:

Voltage = 40 kV.

Current = 40 mA.

Goniometer scan (bulk samples) = 4° – $70^{\circ}2\theta$.

Step size = 0.0087° .

Scan speed = 0.2 s/step.

Divergence slit = 0.3° , 0.6 mm.

When available, additional mineralogical evidence from thin section descriptions or X-ray diffractograms was integrated into the alteration, vein, and vesicle DESClogik template and into the summary text field of the VCDs.

Clay mineral identification using XRD remains tentative, notably because of the absence of well-marked peaks in XRD patterns resulting from the low crystallinity of the clay minerals and the high proportion of associated calcite, which obscures the clay signal. For some samples with high proportions of clay, two other analyses of immediately adjacent material were performed in order to obtain a better resolution for clay mineral peaks. One of the two analyses was conducted after carbonates were dissolved from the sample with diluted hydrochloric acid. The second analysis was performed after ethylene glycolation of the powder (60°C ; 6–12 h). This method expands the crystal network of smectite and results in a d-spacing shift toward lower 2θ (Moore and Reynolds, 1997), which allowed better identification of clay minerals that are present mainly in groundmass resulting from the alteration of interstitial glass, in coatings of vesicle walls, and in veins as intergrowths with other secondary minerals such as carbonate or zeolite.

Structural geology

This section outlines the techniques used for macroscopic and microscopic description of structural features observed in Expedition 330 cores. Conventions for these structural studies generally follow those established during recent IODP hard rock drilling expeditions (Expedition 309/312 Scientists, 2006; Expedition 324 Scientists, 2010).

Detailed observations of structures in the recovered igneous basement of the drilled seamounts allowed us to (1) determine if there has been any post-eruption orientation change of the lava flows, either by tectonic activity close to the Kermadec subduction zone or by seamount flank collapse; (2) document structures in the core and record evidence for the relative timing of the formation of joints, veins, and other structural features caused by magmatic cooling, tectonic processes, and hydrothermal alteration; (3) where possible, record the three-dimensional orientation of all structures (Fig. F9); and (4) obtain orientations of sedimentary features (bedding, erosional surfaces, and geopetals) that may provide information for sedimentologic studies of these flat-topped seamounts. All observations were entered

into the LIMS database using the DESClogik application.

Several features were logged in conjunction with other core describing laboratory groups. The orientation and distribution of veins were first logged by the structural geology group, and subsequently mineral infills and alteration halos were described by the alteration petrology group (see “[Alteration petrology](#)”). Hyaloclastites, volcanic breccia, and chilled margins were first identified and described by the igneous petrology and sedimentology groups (see “[Igneous petrology and volcanology](#)” and “[Sedimentology](#)”), after which the orientations of these structures were entered into DESClogik by the structural geology group. When aligned vesicles occurred because of magma flow, vesicle orientations were recorded in DESClogik after the igneous petrologists had logged the vesicles. Sedimentary bedding was described together with the sedimentologists to ensure consistency in core descriptions.

Graphic symbols and terminology

Material from both the working and archive halves of the core were examined, but structures and orientations were measured exclusively on the archive halves.

A predefined set of structural features was used to maintain consistency in the core descriptions (Fig. [F7](#)). Brittle deformation identifiers include fractures, veins, faults, and breccia. Identification of these features was based on the presence of fractures, filling phases, and evidence of shear displacement. The terminology adopted generally follows that of Ramsay and Huber (1987), Twiss and Moores (1992), and Passchier and Trouw (1996). The terms and symbols used in the structural descriptions are presented in Figures [F7](#) and [F8](#). The features identified include the following:

1. Igneous contacts (demonstrably extrusive or intrusive contacts).
2. Fractures (brittle failure with unknown displacement and no secondary infill minerals). Joints were identified as fractures when the two sides showed no differential displacement relative to the naked eye or a 10× hand lens. Faults are fractures with kinematic evidence for shear displacement across the discontinuity. Breaks clearly resulting from drilling were not logged as fractures.
3. Veins (extensional open fractures filled with secondary minerals).
4. Shear veins (obliquely opening veins with minor shear displacement, filled with slickenfibers or overlapping fibers).
5. Lineations (oriented minerals in shear zones or slickenlines on a fault surface).

6. Magmatic fabrics (magmatic foliations defined by shape-preferred orientations of primary minerals, with no evidence of crystal-plastic deformation).
7. Aligned vesicles (filled or unfilled primary igneous gas bubbles resulting from the outgassing of the lava).
8. Sedimentary bedding.
9. Geopetals (vesicles or voids filled with sedimentary or hydrothermal minerals originally deposited or precipitated horizontally).

This division of structures does not imply that all features fall into distinct and exclusive categories. The term “vein” is preferably used for all healed fractures, avoiding the usual division based on fracture width (e.g., Ramsay and Huber, 1987).

Structural features in the cores recovered during Expedition 330 are summarized in the VCDs (Figs. [F7](#), [F10](#); see “[Core descriptions](#)”). For some important intervals, more detailed structural information is described and photographed in figures within the respective site reports.

Geometric reference frame

To determine the orientation of a structure in the recovered core, a three-step process was followed. In step one, the attitude of a feature on the archive-half core face frame was recorded with a goniometer (Fig. [F11](#)) according to the conventions illustrated in Figure [F9](#). The orientation of planar (Fig. [F9A](#)) or linear (Fig. [F9B](#)) structures in the core was obtained with the goniometer by rotating and holding its moveable (i.e., hinged) plane parallel to the feature to be measured. In the core face frame, the plane along which the core was split is referred to as the apparent horizontal plane, on which 000° points downcore on the archive half and 180° points upcore (Fig. [F9A](#)). When looking onto the face of the archive half in this 360° coordinate system 270° is on the right and 90° is on the left (Figs. [F9](#), [F10](#)).

In step two, the orientations of structures were rotated 90° clockwise about the horizontal 090°–270° axis to transform the measurements from the core face frame into the core reference frame (Fig. [F9C](#)). These rotation calculations were performed using a Perl script written by Expedition 330 scientist L. Kalnins. In the core reference frame, the cut surface of the core is a vertical plane striking 90°–270°, with pseudonorth (000°) pointing out of the cut surface of the archive half and pseudosouth (180°) pointing into the cut surface of the archive half (Fig. [F9C](#)). The core reference frame used herein is consistent with that used by the paleomagnetism group (see “[Paleomagnetism](#)”). All dip and dip direction values listed in the VCDs (Fig. [F10](#)) are reported in the

core reference frame. It is important to note that the dips in the core reference frame represent the actual dips of the features within the seamount, provided that the drill hole is vertical. Dip directions, however, will have been affected by rotary drilling because the core pieces are free to rotate independently around the vertical axis while inside the core barrel. Regardless of the transformation of the measurements into the core reference frame, dip directions are still referenced relative to the plane upon which the core was split (Fig. F9).

The full in situ orientation of the core (i.e., both dip and dip direction) can only be obtained when independent constraints are available, specifically from Formation MicroScanner downhole data (see “[Downhole logging](#)”). Core reorientation is possible by matching structural features recorded on the core to structures on the borehole wall that are imaged by the Formation MicroScanner tool and measured in the true geographic reference frame. This analysis, which forms step three of the structural orientation process, is a target of postexpedition research. For sites without downhole logging, paleomagnetic measurements may potentially be useful for core reorientation, but because of the high paleolatitude of the seamounts, the uncertainty will probably be large (several tens of degrees).

Thin section description

Thin sections made during Expedition 330 were examined in order to (1) confirm macroscopic descriptions of structures, (2) characterize the microstructure of the rocks, (3) identify timing relationships between magmatic and alteration processes and the relative temporal sequence between different groups of veins and joints, and (4) document downhole variations within structured zones.

The microstructural notes were entered into the DESClogik thin section description template (see “[Igneous petrology and volcanology](#)” for details about template). For the description of microstructures we primarily applied the terminology of Passchier and Trouw (1996). Shipboard thin sections were oriented relative to the core face frame, which was marked on each thin section by an arrow pointing upward. Digital photomicrographs were taken during the expedition to document features described in the thin sections. These photomicrographs were also uploaded into the LIMS database.

Geochemistry

Sampling and analysis of igneous rocks

Sample preparation

Representative samples of igneous rocks were analyzed for major and trace element concentrations

during Expedition 330 using inductively coupled plasma–atomic emission spectroscopy (ICP–AES). Samples ranging in size from ~2 to ~8 cm³ were cut from the core with a diamond saw blade. A thin section billet was taken from the same or adjacent interval. All outer surfaces were ground on a diamond-impregnated disk to remove altered rinds and surface contamination derived from the drill or saw. Each sample was then placed in a beaker containing trace-metal-grade methanol and washed ultrasonically for 15 min. The methanol was decanted, and the samples were washed in deionized water for 10 min and then in Barnstead deionized water (~18 MΩ·cm) for 10 min in an ultrasonic bath. The cleaned pieces were dried for 10–12 h at 110°C.

The cleaned, dried samples were crushed to <1 cm chips between two disks of Delrin plastic in a hydraulic press. The chips were then ground to a fine powder in tungsten carbide in a SPEX 8515 Shatterbox. Some samples were amygdular, so before grinding we handpicked chips under a binocular microscope to obtain material as free of amygdules as possible. After grinding, an aliquant of the sample powder was weighed on a Mettler Toledo balance and ignited to determine weight loss on ignition (LOI). Samples were ignited at 930°–960°C for 4 h. For samples from Sites U1372–U1374, the amount of sample weighed for the LOI measurement was 1000.0 ± 0.5 mg. Estimated relative uncertainty on LOI values for these samples is ~14% on the basis of duplicate measurements. For samples from Sites U1375–U1377, a 5000.0 ± 0.5 mg aliquant was used, and the estimated relative uncertainty on LOI values is ~4%.

ODP *Technical Note 29* (Murray et al., 2000) describes in detail the shipboard procedure for digestion of rocks and ICP–AES analysis of samples. The following protocol is an abbreviated form of this procedure with minor modifications. After determination of LOI, 100.0 ± 0.2 mg splits of the ignited whole-rock powders were weighed and mixed with 400.0 ± 0.5 mg of LiBO₂ flux that had been preweighed on shore. Standard rock powders and full procedural blanks were included with unknowns in each ICP–AES run (note that among the elements analyzed, contamination from the tungsten carbide mills is negligible; Shipboard Scientific Party, 2003). All samples and standards were weighed on a Cahn C-31 microbalance (designed to measure at sea) with weighing errors estimated to be ±0.05 mg under relatively smooth sea-surface conditions.

To prevent the cooled bead from sticking to the crucible, 10 mL of 0.172 mM aqueous LiBr solution was added to the mixture of flux and rock powder as a nonwetting agent. Samples were then fused individ-

ually in Pt-Au (95:5) crucibles for ~12 min at a maximum temperature of 1050°C in an internally rotating induction furnace (Bead Sampler NT-2100).

After cooling, beads were transferred to high-density polypropylene bottles and dissolved in 50 mL of 10% (by volume) HNO₃, aided by shaking with a Burrell wrist-action bottle shaker for 1 h. Following digestion of the bead, the solution was passed through a 0.45 µm filter into a clean 60 mL wide-mouth high-density polypropylene bottle. Next, 2.5 mL of this solution was transferred to a plastic vial and diluted with 17.5 mL of 10% HNO₃ to bring the total volume to 20 mL. The final solution-to-sample dilution factor was ~4000. For standards, stock standard solutions were placed in an ultrasonic bath for 1 h prior to final dilution to ensure a homogeneous solution.

Analyses

Major (Si, Ti, Al, Fe, Mn, Mg, Ca, Na, K, and P) and trace (Ba, Sr, Zr, Y, V, Sc, Cu, Zn, Co, Cr, and Ni) element concentrations of standards and samples were determined with a Teledyne Leeman Labs Prodigy ICP-AES instrument. Wavelengths used for sample analysis during Expedition 330 are provided in Table T6. For several elements, measurements were made at more than one wavelength (e.g., Si at 250.690 and 251.611 nm).

The plasma was ignited at least 30 min before each run of samples to allow the instrument to warm up and stabilize. A zero-order search was then performed to check the mechanical zero of the diffraction grating. After the zero-order search, the mechanical step positions of emission lines were tuned by automatically searching with a 0.002 nm window across each emission peak using basalt laboratory standards BAS-140 (Bach et al., 1996) or BAS-206 (Shipboard Scientific Party, 2003) dissolved in 10% HNO₃. During the initial setup, a BAS-140 solution was used to select an emission profile for each peak to determine peak-to-background intensities and set the locations of background levels for each element. The Prodigy software uses these background locations to calculate the net intensity for each emission line. Photomultiplier voltage was optimized by automatically adjusting the gain for each element using BAS-140.

The ICP-AES data presented in the “Geochemistry” section of each Expedition 330 site chapter were acquired using the Gaussian mode of the Prodigy software. This mode fits a curve to points across a peak and integrates the area under the curve for each element measured. Each sample was analyzed four times from the same dilute solution (i.e., in quadruplicate) within a given sample run.

For elements measured at more than one wavelength, we either used the wavelength giving the best calibration line in a given run or, if the calibration lines for more than one wavelength were of similar quality, used the data for each and reported the average concentration.

A typical ICP-AES run (Table T7) included

- A set of 9 or 10 certified rock standards (BCR-2, BHVO-2, BIR-1, JA-3, JGb-1, JR-1, NBS-1c, SCO-1, and STM-1 or MRG-1) analyzed at the beginning of each run;
- As many as 22 samples (unknowns) analyzed in quadruplicate;
- A drift-correcting standard (BHVO-2) analyzed in every fifth sample position and at the beginning and end of each run;
- Blank solutions analyzed near the beginning and end of each run and, in the longer runs, at another point in the middle of the sequence;
- Two or three “check” standards (BHVO-2 and some combination of BCR-2, MRG-1, BAS-140, or BAS-206) run as unknowns, each also analyzed in quadruplicate; and
- A 10% HNO₃ wash solution run for 90 s between each analysis.

Data reduction

Following each run of the instrument, the measured raw-intensity values were transferred to a data file, corrected for instrument drift, and then corrected for the procedural blank. Drift correction was applied to each element by linear interpolation between the drift-monitoring solutions run every fifth analysis. After drift correction and blank subtraction, a calibration line for each element was calculated using the results for the certified rock standards. Element concentrations in the samples were then calculated from the relevant calibration lines.

The United States Geological Survey Hawaiian basalt standard BHVO-2 is the closest in composition to the Expedition 330 igneous rocks, and replicate measurements of this standard analyzed as an unknown were used to estimate precision and provide an idea of accuracy for both major and trace elements. Table T8 summarizes the results and compares them with recommended values (Govindaraju, 1994), showing that for most elements, Expedition 330 values agree very well with published values.

Individual analyses of both standards and samples produced total volatile-free major element weight percentages that vary from 100 wt% by as much as several percent. Possible causes include some combi-

nation of errors in weighing the sample (particularly in rougher seas) and/or flux powders (although weighed on land, weighing errors are nevertheless possible), variability in the dilutions (which were done volumetrically), and the duration and relatively low temperature of ignition. To facilitate comparison of Expedition 330 results with each other and with data from the literature, we normalized the measured major element values to 100 wt% totals.

Semiquantitative X-ray fluorescence analysis

A portable X-ray fluorescence (XRF) spectrometer, the Thermo Scientific Niton XL3 Analyzer, was installed aboard the ship for evaluation during Expedition 330. This instrument provides relatively rapid measurement of concentration for a number of elements in either a 3 or 8 mm diameter area of a sample (X-ray “spot” analysis). For a preliminary report of the results of this evaluation, see XL3_EVAL.PDF in XRF in [“Supplementary material.”](#) In brief, the usefulness of the instrument for reliably distinguishing between different eruptive units via measurement of sawn core faces, cubes, or slabs is restricted to sites with a fairly large range of compositional variation. However, the instrument was found to be quite valuable for material identification in sedimentary intervals and zones of alteration. Interpretation of several core intervals was aided by the identification of ferromanganese material, phosphate, and Fe-poor or Fe-rich carbonates that were present in associations involving two or more phases. These materials could not be identified, or at least not with certainty, by visual or microscopic observation, but the handheld XRF instrument identified them readily.

Sedimentary carbon, carbonate, and nitrogen analysis

Sediment samples were taken from the interiors of cores with autoclaved cut-tip syringes. They were then freeze-dried to remove water and powdered to ensure homogenization. Carbonate content was determined by acidifying ~10 mg of bulk powder with 2M HCl and measuring the CO₂ evolved, all of which was assumed to be derived from CaCO₃. A UIC coulometer was employed for the measurement. The weight percent of total inorganic carbon was calculated by dividing the CaCO₃ content in weight percent by 8.33.

We determined total carbon content for the same samples by combusting the sample at an initial temperature of 900°C in a Flash EA-1112 Series Thermo Electron Corporation CHNS analyzer (CHNS stands for carbon-hydrogen-nitrogen-sulfur). The total carbon value was then used to calculate weight percent

of total organic carbon via subtraction. That is, the weight percent of inorganic carbon derived from the carbonate measured by coulometric analysis was subtracted from the total carbon content obtained with the CHNS analyzer.

Physical properties

Shipboard measurements were performed to characterize the physical properties of the recovered material. The primary objective of Expedition 330 was to recover hard rock, which necessitated a modified approach compared with expeditions focusing on the recovery of soft sediment. The descriptions herein relate specifically to hard rock material; sedimentary material was treated in the same manner, except where otherwise specified.

Once recovered, whole-round cores were first allowed to thermally equilibrate to ambient room temperature (~3 h for both hard rock and sedimentary material). Core sections with continuous intervals of >8 cm were run through the Whole-Round Multi-sensor Logger (WRMSL) for measurement of gamma ray attenuation (GRA) bulk density and magnetic susceptibility. The WRMSL also incorporates a non-contact resistivity detector and a compressional wave (*P*-wave) velocity logger. The noncontact resistivity detector was not used on this expedition, and the *P*-wave logger was used only for sections where unconsolidated sediment filled most of the core liner because the diameter of hard rock cores is generally too small to make good contact with the core liner. Sections longer than 50 cm were measured with the Natural Gamma Radiation Logger (NGRL).

After measurements with the WRMSL and NGRL, the cores were split into archive and working halves. The archive half of the core was passed through the Section Half Multisensor Logger (SHMSL) for measurement of point magnetic susceptibility and color reflectance. The SHMSL uses a laser to create a profile of the archive half of the core, which yields information about the location of gaps and cracks between pieces of the core. This information was used to filter out data from gaps and cracks between pieces in magnetic susceptibility, color reflectance, and GRA data using a custom-designed MATLAB program suite, as described in [“Data filtering.”](#) The filtered data were then visually double-checked against images of the core section halves.

Nondestructive thermal conductivity testing was performed on the working halves of the split cores. Until failure of the thermal conductivity instrument prevented further testing (see [“Thermal conductivity”](#)), roughly one measurement was made per core,

depending on core recovery and lithologic variability.

Lastly, discrete samples were taken from the working half of the core with a sampling interval of approximately 2–3 m, depending on lithologic variability. Many of these discrete samples were used for paleomagnetic measurements of alternating-field demagnetization (see “[Paleomagnetism](#)”), before being used for measurements of compressional wave velocity in three orthogonal directions and moisture and density measurements of wet bulk density, dry bulk density, grain density, water content, void ratio, and porosity. Details about each physical property measurement are given below. A comprehensive discussion of methodologies, calibrations, and calculations used in the *JOIDES Resolution* physical properties laboratory is presented by Blum (1997).

Whole-Round Multisensor Logger measurements

GRA-derived bulk density and magnetic susceptibility were measured nondestructively with the WRMSL. To optimize WRMSL performance, sampling intervals and measurement integration times were the same for all sensors. Sampling intervals were set at 2 cm, with an integration time of 5 s for each measurement. These sampling intervals are common denominators of the distances between the sensors installed on the WRMSL (30–50 cm), which allows sequential and simultaneous measurements. After every core, quality control and assurance were monitored by passing a single core liner filled with deionized water through the WRMSL. For Expedition 330, the primary objective was the recovery of hard rock, which is often recovered in pieces rather than intact core. Anomalously low values associated with gaps and cracks in the core were removed using a data filtering procedure (see “[Data filtering](#)”).

Gamma ray attenuation bulk density

The GRA densitometer on the WRMSL operates by passing gamma rays from a ^{137}Cs source through a whole-round core into a 75 mm × 75 mm sodium iodide detector situated directly below the core. The gamma ray peak has a principal energy of 0.662 MeV that attenuates as it passes through the core. The attenuation of gamma rays occurs primarily by Compton scattering, which is related to the material bulk density; therefore, for a known thickness of sample, the density (ρ) is proportional to the intensity of the attenuated gamma rays and can be expressed as

$$\rho = \ln(I/I_0)/(\mu d),$$

where

I = measured intensity of gamma rays passing through the sample,

I_0 = gamma ray source intensity,

μ = Compton attenuation coefficient, and

d = sample diameter.

μ and I_0 are treated as constants, such that ρ can be calculated from I .

In general, WRMSL measurements are most accurate when taken on a completely filled core liner with minimal drilling disturbance; otherwise, measurements tend to underestimate true values. By default, the instrument reports measurements using the internal diameter of the core liner (66 mm) as the assumed sample diameter. This assumption is suitable for most sediment cores; however, for hard rock the core diameter is usually <58.5 mm. Following Jarrard and Kernekian (2007), the density measurements were corrected by multiplying the density values by $66/58 = 1.138$ to account for this bias.

The spatial resolution of the GRA densitometer is less than ± 1 cm. Calibration of the densitometer was done using a set of aluminum cylinders encased in a core liner filled with distilled water. Recalibration was performed as needed when the deionized water quality control and assurance standard deviated significantly (more than a few percent) from 1 g/cm³.

Magnetic susceptibility

Magnetic susceptibility (K) is a dimensionless measure of the degree to which a material can be magnetized by an external magnetic field:

$$K = M/H,$$

where M is the magnetization induced in the material by an external field of strength H . Magnetic susceptibility is sensitive to the type and concentration of magnetic minerals within a material, making it useful in identifying compositional variations. Materials such as clay, possibly from alteration of igneous materials, have a magnetic susceptibility several orders of magnitude lower than magnetite and some other iron oxides that are common constituents of igneous material. Water and plastics (e.g., core liner) have a slightly negative magnetic susceptibility.

The WRMSL incorporates a Bartington Instruments MS2 meter coupled to an MS2C sensor coil. Data from this instrument require a correction factor, which depends on both the instrument and the operating frequency. For Expedition 330, the instrument operated at a frequency of 0.621 kHz, whereas the sensor assumes an operating frequency of 0.595

kHz. The data are multiplied by the appropriate factory-supplied correction factor of 1.099 before being uploaded to the LIMS database. These values, however, must be converted to dimensionless SI units by multiplying by 10^{-5} . Measurements from the MS2C sensor are also sensitive to the diameter of the core relative to the diameter of the sensor coil and thus require an additional correction. The true magnetic susceptibility of the core is given by

$$K = \alpha K_{\text{rel}},$$

with

$$\alpha = 0.290(D/d)^3,$$

where

- K = magnetic susceptibility of the core,
- K_{rel} = measured magnetic susceptibility,
- D = coil diameter (i.e., the aperture diameter plus 8 mm) (see MS2 Magnetic Susceptibility System operation manual, www.bartington.com/operation-manuals.html), and
- d = core diameter.

For the instrument on board the *JOIDES Resolution*, $D = 88$ mm, which gives a value of $\alpha = 1.0$ for hard rock cores (with d generally between 58 and 58.5 mm) and $\alpha = 0.687$ for sediment cores (with $d = 66$ mm). However, for consistency with previous expeditions, we followed Blum (1997) and used $\alpha = 0.68$ for intervals containing unconsolidated sediments, corresponding to a core diameter of 66.1–66.2 mm. Data discussed in the site reports and shown on the VCDs reflect corrected values. However, data in the LIMS database remain uncorrected, with only the factory-supplied correction applied.

The spatial resolution of the MS2C instrument is ± 2 cm; therefore, magnetic susceptibility of core material that is not continuous over a 4 cm interval will be underestimated. Data collected near gaps or from pieces <4 cm in length were removed by a filtering process (see “[Data filtering](#)”). The removed data are shown as shaded points in the VCDs but are not shown in the site report figures. Quality control and assurance was performed at the start of the expedition with a factory-provided standard of a homogeneous mixture of magnetite and epoxy (to prevent oxidation of the magnetite) in a 40 cm long piece of core liner.

Natural Gamma Radiation Logger

The NGRL installed on the *JOIDES Resolution* was designed and built at the Texas A&M University IODP-USIO facility from 2006 to 2008. Natural gamma ra-

diation (NGR) arises primarily as a result of the decay of ^{238}U , ^{232}Th , and ^{40}K isotopes. Data generated from this instrument are used to augment geologic interpretations, including delineation of flow boundaries and alteration zoning throughout the core. The NGRL consists of 8 sodium iodide (NaI) scintillator detectors, 7 plastic scintillator detectors, 22 photomultipliers, and passive lead shielding. The NaI detectors are covered with 8 cm of lead shielding. Half of the lead shielding closest to the NaI detectors is composed of low-background lead (~ 3 Bq/kg internal radioactivity rate), and the outer half is composed of regular (virgin) lead (50–200 Bg/kg). Lead separators composed of ~ 7 cm of low-background lead are also positioned between the NaI detectors. In addition to passive lead shielding, the NGRL employs a plastic scintillator that suppresses data collection when high-energy gamma and muon components of cosmic radiation pass through it.

For reporting purposes, the counts are summed over the range of 100–3000 keV to be comparable with data collection from previous expeditions and for direct comparison with downhole logging data. Background measurements of an empty core liner were made for a total count time of 11 h when moving to new sites located at least 150 nmi from the previous site (~ 15 h of total transit time); this background radiation was then automatically subtracted from each new measurement. For Site U1377, technical difficulties with the NGRL software meant that background measurements could only be taken for 4.5 h instead of the standard 11 h.

NGRL measurements are taken at a spatial resolution of 10 cm for a total of 16 measurements on a standard 150 cm long section of core. Because the detector unit contains eight sensors positioned 20 cm apart, analysis of each section of core consists of two steps: the first set of eight measurements at 20 cm apart, followed by a shift of the core section by 10 cm for the second set of eight measurements. For each section, the count time was the same at each position. Sections <50 cm in length were not logged.

The quality of the NGRL data depends on the concentration of radionuclides in the sample and also on the counting time, with higher times yielding better counting statistics and more accurate measurement of the energy spectra for each detector. It may be possible during postexpedition analyses to separate high-quality energy spectra into ^{40}K , ^{232}Th , and ^{238}U contributions, leading to eventual quantification of concentrations of the radionuclide daughters. During Expedition 330, count times ranged from 0.25 to 1 h for each position, resulting in total count times of 0.5–2 h per section, depending on

core recovery and overall core flow. There was a concerted effort to keep count times as high as possible for future work on total abundance calculations, but ultimately times had to be reduced to keep up with exceptionally high recovery, particularly at Site U1374. For Sections 330-U1374A-42R-3 through 73R-1, count times were reduced to 60 min for sections containing potential lava flows or lobes and 30 min for all other sections. For Site U1377 cores, count times were reduced from 60 to 30 min, as needed, to ensure core was processed as quickly as possible before the end of the expedition. The counting statistics for these shorter measurement times are still of acceptable quality because the alkalic rocks of the Louisville Seamount Trail contain significantly higher K, U, and Th concentrations than mid-ocean-ridge basalt oceanic crust.

The NGRL was calibrated using a ^{137}Cs and ^{60}Co source, identifying the peaks at 662 keV (^{137}Cs) and 1330 keV (^{60}Co) using calibration materials obtained from Eckert and Ziegler Isotope Products (Valencia, California [USA]).

Section Half Multisensor Logger measurements

The SHMSL measures color reflectance and magnetic susceptibility on core section halves. The archive half of the split core is placed on the core track, above which an electronic platform moves along a track, recording the height of the split-core surface with a laser sensor. The laser establishes the location of the bottom of the section, and then the platform reverses the direction of movement, moving from bottom to top making measurements of point magnetic susceptibility and color reflectance. During Expedition 330, point magnetic susceptibility and color reflectance data were collected at 1 cm intervals, the highest possible resolution.

Color reflectance spectrometry

Color reflectance of the core was measured using a color reflectance spectrometer that takes measurements from 380 to 900 nm wavelengths at 2 nm intervals using an Ocean Optics 30 mm integrating sphere and both halogen and LED light sources, covering wavelengths from ultraviolet through visible to near-infrared. The scan of the entire wavelength range takes ~5 s per data acquisition offset. From the full reflectance spectra collected, the data are reported using the $L^*a^*b^*$ color system, in which L^* is lightness, a^* is redness (positive) versus greenness (negative), and b^* is yellowness (positive) versus blueness (negative) of the rock. The color reflectance spectrometer calibrates on two spectra: pure white

(reference) and pure black (dark). Color calibration was conducted approximately once every 6 h (twice per shift).

Point magnetic susceptibility

Point magnetic susceptibility was measured with a Bartington MS2 meter and an MS2E contact probe with a flat 3.8 mm \times 10.5 mm rectangular sensor with a field of influence of 5 mm and an operation frequency of 2 kHz. The instrument averages three measurements from the sensor for each 1 cm offset, leading to an accuracy of ~5%. The spatial resolution of the point magnetic susceptibility instrument is ~3.8 mm, making it better than whole-round magnetic susceptibility for sections containing broken pieces <4 cm in length (the spatial resolution of whole-round magnetic susceptibility). As with whole-round magnetic susceptibility measurements, the output displayed by the point magnetic susceptibility sensor must be converted to dimensionless SI units by multiplying by 10^{-5} . The probe is zeroed in air before each measurement location to avoid influence from the metal track. The point magnetic susceptibility meter was calibrated by the manufacturer before installation on the ship and is quality checked every ~6 h at the same time as color reflectance sensor calibration.

Thermal conductivity

Thermal conductivity is the measure of a material's ability to conduct heat and is sensitive to the material's porosity, composition, and microstructure. Measurements of thermal conductivity were made by transiently heating samples with an automatically determined heat flux controlled by the heating power and duration using either half-space or full-space geometry. The changes in temperature with time after initial heating were recorded using a Teka TK04 instrument system. The temperature of the superconductive probe has a linear relationship with the natural logarithm of the time after the initiation of heating (Blum, 1997).

For lithified sections, thermal conductivity was measured on the split core with the probe in half-space mode using a needle probe embedded in the surface of an epoxy block with a low thermal conductivity (Vacquier, 1985). Sample surfaces need to be smooth to ensure adequate contact with the heating needle. Silicon gel can be employed to improve sample/needle contact, but this was avoided during Expedition 330 in order to keep the samples clean.

Cores were measured at irregular intervals at an average of once per core, depending on the availability of homogeneous and relatively vein- and crack-free

pieces that were long enough to be measured without edge effects. Pieces should be at least 7 cm long, longer than the instrument needle. Samples were selected from the working half and returned unaltered to the core liner upon completion of the tests. The sample and sensor needle were equilibrated together in seawater in a cooler insulated with extruded polystyrene foam for at least 1 h prior to measurement. Isolation of the sample and sensor needle eliminated the effect of rapid but small temperature changes introduced by air currents in the laboratory.

Thermal conductivity in unlithified sediment was measured once per core when deemed appropriate, depending on the degree of presumed drilling disturbance. These measurements were taken using a needle embedded in the center of the section, with the probe in full-space mode.

At the beginning of each measurement, temperatures in the samples were monitored to ensure that the background thermal drift was $<0.04^{\circ}\text{C}/\text{min}$. After the background thermal drift was determined to be stable, the heater circuit was closed and the increase in the probe temperature was recorded. Maximum sample temperature during the measurements did not exceed 25°C for sediment or hard rock.

Thermal conductivity values were determined from the average of three repeated measurements. Individual measurements are usually within 1% of the mean for both full- and half-space measurements and thus within a total uncertainty of 5% (Blum, 1997). Measurements were made at room temperature and pressure and were not corrected for subsurface conditions. A MACOR ceramic standard with a certified thermal conductivity of $1.637 \pm 0.033 \text{ W}/(\text{m}\cdot\text{K})$ (TeKa, Version 4.0.2) was tested frequently as a quality assurance check to ensure that readings remained accurate.

Unfortunately, during thermal conductivity testing on core intervals from Site U1374, the hard rock thermal probe puck began to yield unreliable values, intermittently producing no value at all and then becoming completely nonfunctional. A backup thermal conductivity probe puck was then used, and it yielded one additional reasonable data point before failing as well. The probes were thoroughly dried and then used with the MACOR ceramic standard to check for accuracy. Each puck produced results for several tests but returned values significantly lower than the standard $1.637 \pm 0.033 \text{ W}/(\text{m}\cdot\text{K})$ value before failing completely once again. These probe malfunctions are attributed to water seeping into the electronic wiring, thus shorting out the device and corroding the wiring. This corrosion changed the resistivity of the wiring (to which these measurements are very sensitive), and thermal conductivity mea-

surements could not be made for the remainder of the expedition.

Discrete samples

Cubic samples were cut from the working halves of split cores at an interval of approximately one sample for every two sections. These $\sim 8 \text{ cm}^3$ samples were selected to best represent the major stratigraphic units and any variation in lithology. To minimize core depletion, most discrete samples were used for paleomagnetic measurements of alternating-field demagnetization (see “[Paleomagnetism](#)”) before being used for compressional wave velocity and moisture and density measurements, as discussed below.

Moisture and density

Several rock properties (water content or moisture, bulk density, dry density, porosity, and void ratio) were determined through precise mass and volume determinations on discrete samples. Moisture and density data were also used for comparison with GRA-derived bulk density data from the WRMSL. The shipboard moisture and density facility on the *JOIDES Resolution* for hard rock coring consists of a vacuum water saturator, a dual balance system, and a pycnometer.

Sample preparation

Determination of a precise and accurate wet mass of sparsely porous material requires that the pore space of the sample be completely saturated. To do this, we placed the samples in individual plastic vials filled with seawater and used a vacuum chamber. A vacuum pump removed the air from the chamber to a pressure of $\sim 40\text{--}50 \text{ kPa}$ below atmospheric pressure, forcing the seawater into the samples. The samples were kept under saturation for at least 24 h. After removal from the saturator, the cubes remained in the plastic vials filled with seawater to help prevent evaporation of pore water. Next, the cube surfaces were patted dry with a paper towel and wet mass was immediately determined using the dual balance system. Compressional wave (*P*-wave) velocities were then measured on the wet sample. Following the velocity measurements, the samples were dried in a convection oven for at least 24 h at $105^{\circ} \pm 5^{\circ}\text{C}$. Dried samples were then cooled in a desiccator for at least 60 min before the dry mass was measured.

Dual balance system

The dual balance system was used to measure both wet (M_w) and dry (M_D) masses. Two analytical Mettler-Toledo XS204 balances were used to compensate

for ship motion: one acting as a reference and the other for simultaneously measuring the unknown. A standard weight with similar mass to the sample (± 1 g) was placed on the reference balance to increase accuracy, giving a precision of better than 0.005 g (Expedition 324 Scientists, 2010). The default setting of the balances is 300 measurements, which takes ~ 1.5 min. However, in rough seas and during transit we found that longer measurement times of 400–1500 counts, depending on sea state, were required to keep the error range at or below 0.001 g. In addition to electronic records, the final masses and count, if different from 300, were also recorded on data log sheets, hard copies of which are stored at IODP at Texas A&M University.

Pycnometer system

The pycnometer system measures dry sample volume (V_D) with a nominal precision of ± 0.04 cm³. Constant-volume gas pycnometers allow volume measurements to be made by evaluating gas pressures between two sealed chambers: a sample chamber and an expansion chamber. The sample chamber is pressurized to an initial pressure (P_1), and then the gas is allowed to expand into the second chamber. The sample volume, V_S , is then given by

$$V_S = V_C + [V_E(P_A - P_2)]/(P_1 - P_2),$$

where

- V_C = known volume of sample chamber when empty,
- V_E = known volume of expansion chamber,
- P_A = ambient pressure, and
- P_2 = pressure after gas is allowed to expand into both chambers.

For Expedition 330, the pycnometer system on board the *JOIDES Resolution* had five working sample chambers, each with its own expansion chamber, allowing as many as four samples to be measured per run.

At the start of the expedition and midway through when the helium gas tank was changed, shipboard technicians performed a calibration using stainless steel spheres of known volume to determine the volume of the sample and expansion chambers. During both acquisition and measurement, the three data acquisition cycles were preceded by three purges of the sample chambers with research-grade (99.995% or better) helium gas heated to 28°C. These purges help remove any volatiles that could affect chamber pressure. A batch of samples consisted of four cells with unknowns and one cell with two stainless steel spheres (3.2 and 7.0 cm³), assumed to have a total

volume known to within 1%. The spheres were routinely cycled through the different cells to identify any systematic error or instrument drift. The final volume for each sample was recorded on the data log sheets together with mass information.

Moisture and density calculations

Following physical measurements of wet mass (M_w), dry mass (M_D), and dry volume (V_D), the physical properties shown in Table T9 were calculated. During Expedition 330, moisture and density Method C was used to increase the accuracy of the wet mass measurements (Blum, 1997).

Compressional wave velocity

Using the same discrete cube samples as were used for moisture and density measurements, the compressional wave (*P*-wave) velocity of hard rock samples was measured immediately after determination of wet mass. The system uses Panametrics-NDT Microscan delay line transducers, which transmit at 0.5 MHz. To maximize contact with the transducers, de-ionized water was applied to sample surfaces before the transducers were placed on the sample. Measurements used *x*-axis caliper-type contact probe transducers on the *P*-wave velocity gantry, and oriented samples were rotated manually to measure the other two axes. The three orthogonal axes form a right-handed coordinate system and are defined as follows: the *x*-axis is normal to the split-core surface and pointing into the working half, the *y*-axis is horizontal and parallel to the split-core surface, and the *z*-axis is downcore. The reference frame is identical to that used for paleomagnetism and structural geology analyses (see “[Structural geology](#)” and “[Paleomagnetism](#)”).

The signal received through the sample was recorded, and the peak of the initial arrival was chosen with automatic-picking software. The complete waveform was automatically stored by the system, should reanalysis be deemed necessary; however, shipboard visual checks of the picks appeared satisfactory. The distance between transducers was measured with a built-in linear variable differential transformer (LVDT).

Calibration was performed before measurements were made at least once a day using a series of acrylic cylinders of differing thicknesses and known *P*-wave velocities of 2750 ± 20 m/s. The system time delay determined from calibration (i.e., the delay observed using the acrylic standards) was subtracted from the picked arrival time to give the traveltime of the *P*-wave through the sample. The thickness of the sample (calculated by the LVDT in meters) was di-

vided by the traveltime (in seconds) to calculate a *P*-wave velocity in meters per second.

Data filtering

To remove spurious data in hard rock core sections related to gaps and piece breaks, magnetic susceptibility, GRA-derived bulk density, L^* , a^* , b^* , and point magnetic susceptibility data were filtered using a MATLAB program suite. These programs were written by Expedition 330 scientists L. Kalnins and P. Fulton and were inspired by a similar procedure written by A. Harris (Expedition 324 Scientists, 2010). This program uses sample height data collected with the laser attached to the SHMSL to identify cracks between pieces and gaps where plastic spacers were inserted between pieces. These gaps and cracks will, in general, provide anomalously low GRA-derived bulk density and whole-round and point magnetic susceptibility values, as well as irrelevant color reflectance values. The NGR whole-round data were not filtered because of the large sampling interval.

Cracks and gaps in the core were detected using a combination of the curated piece lengths and positions, a minimum laser height, and the gradient of the laser height. Starting from the curated piece divisions, the filter attempts to find a gap matching each division, defined as a region bounded by gradients in excess of 40% (the piece edges) or falling below the minimum laser height. If a gap cannot be detected (for example if the pieces are pressed against the plastic divider), the curated piece division is used. Pieces are then further divided using two criteria: first, any gaps detected above (bounded by gradients in excess of 40% or falling below the minimum laser height) that did not correspond to a curated piece division and, second, smaller cracks with a gradient of >10% and an extent of <1 cm. Limiting the extent of this second detection threshold to 1 cm prevents removal of pieces that are not horizontal in the core liner. Finally, pieces <2 cm in length were removed and the subdivisions were checked against core photographs to remove spurious piece breaks (e.g., breaks due to large vesicles, which are indistinguishable from cracks using a single laser profile). Data measured in the spaces between pieces, as well as measurements taken near piece edges, were then removed. Finally, remaining outliers were removed using an iterative implementation of the Grubbs test (Grubbs, 1969).

The gradient thresholds to test for both gaps and cracks, as well as minimum piece length, can be set by the user. The values used here were experimentally tuned to balance the number of divisions not

detected with the number of spurious piece breaks introduced, based on laser profiles with a measurement every 0.1 mm (accurate to ± 0.02 mm). In the filtering program, the edge effect (i.e., how far a measurement must be from a gap or crack to remain unaffected by the missing material) associated with each instrument may also be set by the user, together with the minimum length that a piece must be to provide an acceptable measurement, typically twice the edge effect. Parameter settings used to create filtered data sets for this expedition are listed in Table T10.

Data that were filtered out appear in the VCDs as shaded points, whereas data that met the criteria described above (e.g., GRA-derived bulk density measurements that were at least 1 cm away from a gap or crack and that were measured on pieces that were at least 2 cm long) are plotted as solid colored points according to the legend. Only data that met the filtering parameters are shown on the figures in the site reports. For GRA-derived bulk density and whole-round magnetic susceptibility data, the corrections to account for the average core diameter were applied even to data that were filtered out, because these corrections resulted from instrumentation design and are not related to the filtering process.

The major benefit of filtering GRA-derived bulk density, magnetic susceptibility, and color reflectance data is that actual variations can be discerned from data trends. Data that are filtered out of the GRA-derived bulk density and magnetic susceptibility data sets are underestimates of real values because of edge effects. However, caution should be used because filtering parameters have been set to remove a minimum amount of data, so some data affected by discontinuities in the core may remain.

Paleomagnetism

During Expedition 330, routine paleomagnetic and rock magnetic experiments were carried out aboard the *JOIDES Resolution*. Remanent magnetization was measured on archive core halves and on discrete cube samples taken from working core halves. All continuous archive halves were demagnetized in an alternating field (AF), whereas discrete samples were subjected to either stepwise AF or thermal demagnetization. Since the azimuthal orientations of core samples recovered by rotary drilling are not constrained, all magnetic data are reported relative to the sample core coordinate system. In this system, $+x$ is perpendicular to the split-core surface and points into the working half (i.e., toward the double line),

+z is downcore, and +y is orthogonal to x and z in a right-hand sense (Fig. F12).

Archive-half remanent magnetization data

Remanent magnetization of the archive halves, including any undisturbed sediment, was measured at 2 cm intervals using the automated pass-through direct-current superconducting quantum interference device (DC-SQUID) cryogenic rock magnetometer (2G Enterprises model 760R). An integrated in-line AF demagnetizer (2G Enterprises model 600) capable of applying peak fields up to 80 mT was used to progressively demagnetize the core. Demagnetization steps were typically (5), 10, (15), 20, (25), 30, 40, 50, (60), and (70) mT, where the fields in parentheses were not always performed.

With strongly magnetized materials, the maximum intensity that can be reliably measured (i.e., with no residual flux counts) is limited by the slew rate of the sensors. At a track velocity of 2 cm/s, it was possible to measure archive-half cores with a magnetization as high as ~ 10 A/m. Where even this slow measurement speed still resulted in residual flux counts, the data were nonetheless archived because they provide some indication of the character of the magnetization. Caution is therefore warranted in using archive-half data from strongly magnetized intervals. Although the baseline values measured just prior to and just after archive-half measurements were not saved in the database, the baseline drift, and thus the number of residual flux counts, can be determined indirectly from the archived directional and intensity data. We developed LabView software (WebTabularToMag) to reconstruct the baseline drift, allowing the residual flux counts to be logged while the data were converted for further processing.

A noise test was conducted on the magnetometer on a relatively calm day on station to assess the practical resolution of the instrument. This test was performed with a modified version of the Scripps Institution of Oceanography LabView code in order to allow more rapid communication with the magnetometer and therefore capture an unaliased record of wave noise. All three axes were sampled simultaneously every ~ 0.5 s, in contrast with the existing magnetometer software that sequentially accessed these data at a slower rate of ~ 3.5 s. The spectra from these magnetic noise measurements (Fig. F13) revealed a peak at the dominant period (8–12 s) of wave motion, corresponding to a moment of a $\sim 1 \times 10^{-9}$ Am² and therefore a practical resolution of $\sim 1 \times 10^{-5}$ A/m for a core half.

The most recent compiled version of the LabView software (SRM_SAMPLE) is Build 1.0.0.3. However,

an uncompiled version of this program (BETA with speed control) was used throughout the expedition because this allowed the track speed to be adjusted, a critical parameter for hard rock expeditions. Two modifications to the program and the Galil motor system were made during the expedition. First, the speed at which the archive halves were moved when not measuring was increased to 20 cm/s. Second, the simultaneous sampling of the magnetometer axes described above was also incorporated into the magnetometer software midway through measurements on archive halves from Hole U1374A (a more rapid measurement routine was implemented on 14 January 2011 with Section 330-U1374A-31R-3). Together, these changes resulted in substantial time savings (on the order of 0.5 h per section with 6–8 demagnetization steps) and also allowed multiple measurements at each interval for weakly magnetized cores.

The response functions of the pick-up coils of the SQUID sensors have a full width of 7–8 cm at half height (Parker and Gee, 2002). Therefore, data collected within ~ 4 cm of piece boundaries (or voids) are significantly affected by edge effects. Consequently, all data points within 4.5 cm of piece boundaries (as documented in the curatorial record) were filtered out prior to further processing. It should be noted that edge effects may also occur in a contiguous core piece if substantial heterogeneity (in intensity or direction) is present in the piece. Such artifacts are more difficult to filter out, but calculating the average direction (using Fisher statistics) for each core piece provides a means of identifying these problems (see below).

Automated calculation of best-fit directions

Remanent magnetization directions were calculated for each 2 cm measurement using principal component analysis (PCA; Kirschvink, 1980). Manual selection of principal component directions was not practical given the substantial amount of data. Rather, we used an automated procedure to select the most linear segment of the demagnetization data. PCA was conducted for each permutation of four or more consecutive demagnetization steps (typically 6–8 steps). The following criteria were then used to calculate a single misfit value that could be minimized to select the best-fit direction and to assign a reliability index to this selection. First, the range of demagnetization steps must yield a fit with low scatter (e.g., Fig. F14A), as defined by the maximum angular deviation (MAD, as used in equations below) of the PCA fit. Second, the selected direction should trend toward the origin. Deviation from the origin (e.g., Fig. F14B, F14F) may indicate that an unresolved higher coercivity component is present or that a spurious

magnetization was acquired during demagnetization. Deviation of the fit from the origin is calculated from the solid angle (α) between the unconstrained PCA fit and the fit anchored to the origin. Third, a particular fit is generally judged to be more reliable if a large percentage of the remanence (f) is used for the calculation (e.g., Fig. F14A, F14C). We use the vector difference sum (the cumulative sum of the magnetization vector removed at each demagnetization step) to characterize the percentage of the remanence, as this is monotonically decreasing. By selecting target values (α_o , MAD_o , and f_o) for each of these criteria, a single misfit value may be calculated for each trial PCA fit:

$$\text{misfit} = \{(\alpha/\alpha_o) + [(1-f)/(1-f_o)] + (MAD/MAD_o)\}.$$

Although minimizing the above misfit value finds a suitable best-fit direction in many cases, two additional constraints were introduced. Selecting the largest percentage of the remanence has the unfortunate side effect of preferentially excluding particularly high coercivity intervals (which in fact may provide the highest quality remanence data). We therefore allowed a best-fit direction to be anchored to the origin if the anchored fit represents a significant improvement (enforced through a penalty, arbitrarily set at 1.5, on anchored fits). The misfit for such anchored fits is given by

$$\text{misfit}_A = \{(CSD/\alpha_o) + [(1-f)/(1-f_o)] + (MAD/MAD_o)\} \times 1.5,$$

where the circular standard deviation (CSD) of the remanence vectors used for the fit replaces α for the unconstrained fit. Finally, where a substantial low-coercivity component (e.g., from drilling) is present, the natural remanent magnetization step, and optionally the first demagnetization step, may be eliminated prior to finding the lowest misfit.

The best-fit PCA was calculated using target values of $\alpha_o = 5^\circ$, $MAD_o = 3^\circ$, and $f_o = 0.6$, unless otherwise noted. The values of the misfit parameters provide a qualitative measure of reliability and have been used to filter out less reliable data. If all three parameters contributing to the misfit equal the target values, the misfit value will be equal to 3.0 for a free (not anchored) PCA fit. The minimum misfit distributions for the three data sets from Holes U1372A, U1373A, and U1374A are shown in Figure F15. The three cumulative distribution curves intersect at a misfit value of ~ 3.4 , and for each data set $\sim 40\%$ of the data have misfit values lower than this value. We elected to retain only the most reliable 40% of the data for further analysis, which corresponds to a cutoff value of 3.40 for Hole U1372A and 3.42 for Holes U1373A

and U1374A. The histograms in Figure F15 illustrate the distributions of MAD , α , and f values for the 40% of the data with misfit values below the cutoff value.

This automated selection routine generally provides a reasonable fit to the demagnetization data (Fig. F14). Low-coercivity overprints, such as drilling-induced remanent magnetization, are ignored whether they constitute a small or substantial percentage of the natural remanent magnetization (Fig. F14C, F14D, F14E, F14G). The program does not find a satisfactory straight line fit for samples exhibiting curvilinear behavior, as one would expect (Fig. F14B). Anchored PCA fits constitute 12% of the directions with misfits less than the cutoff value. Although some high-coercivity samples with apparently reliable directions are excluded (Fig. F14H), any inclination bias due to such anchored fits is minimized.

Note that the intensity reported for such PCA directions represents the length of the projection of the lowest- and highest-treatment vectors used in the PCA calculation onto the best-fit direction. Because the origin is not included in the PCA calculation and the remanence remaining after the highest treatment may be significant, the resulting characteristic remanent magnetization intensity values are systematically lower than those derived from the remanence at the lowest demagnetization step adopted for the PCA calculation.

Piece-average directions

The mean remanent magnetization of individual archive-half pieces >9 cm was calculated as an additional internal reliability check. All 2 cm individual PCA directions with sufficiently low misfits (see above) were averaged using Fisher statistics; the reported PCA intensity is the vector mean. Heterogeneous magnetization directions in a single piece can be identified from high values of the associated CSD. Figure F16 shows the data from a single piece and illustrates two aspects of the adopted piece-averaging approach that should be kept in mind. First, the piece average is calculated using the curated piece lengths assuming that all subpieces have the same relative orientation. Thus, any subpieces that have rotated relative to one another may adversely affect the mean direction (e.g., the break between subpieces at ~ 65 cm in Section 330-U1372A-9R-2 [Piece 1] in Fig. F16). Second, when boundaries separating flows or lithologic units with different directions or intensities occur within a piece, the average direction may be erroneous. Conversely, if they are sufficiently different, inclination variations in a piece may facilitate recognition of unit boundaries. Hence, piece averages with $CSD > 20^\circ$ were excluded from further shipboard analysis. However, it is likely that

careful analysis of changes at subpiece boundaries would allow some of these rejected data to be retained in later shore-based analysis of the data.

Discrete sample data

All discrete samples taken from the working halves for shipboard magnetic analysis were 8 cm³ cubes. Although standard 2.5 cm diameter minicores are more commonly used, the cubic samples were preferred because they should have a more reproducible vertical reference (based on a double-bladed saw cut perpendicular to the core length) than the minicores (where the fiducial arrow on the split-core face must be transferred to the long axis of the sample). Discrete samples for shipboard analysis were selected on the basis of identified flow boundaries, the in situ confidence index (see “[Igneous petrology and volcanology](#)”), and results from archive-half stepwise AF demagnetization.

The remanent magnetization of discrete samples was measured exclusively with the JR-6A spinner magnetometer following tests of discrete sample measurements on the cryogenic magnetometer (described below). For samples measured on the spinner magnetometer, the automated sample holder was used, providing the most accurate discrete sample remanent magnetization directions and intensities. A set of four standard samples (previously measured in the shielded room at the Scripps Institution of Oceanography and archived as SIO 1, SIO 2, SIO 6, and SIO 8) was measured on the spinner magnetometer. The directions obtained were typically within 1°–2° of the known values, and intensities were accurate to within a few percent.

The current version of the software for discrete sample measurements on the cryogenic magnetometer (SRM_DISCRETE, Build 1.0.0.1) allows for measurement in 24 separate orientations. The four SIO standards were measured in all orientations (Fig. F17). These experiments revealed considerable scatter among these 24 positions, ranging from ~10°–15° for strongly magnetized samples (~1–10 A/m) up to and exceeding 30° for weaker samples. The origin of this scatter is unknown. For this reason, all discrete samples were measured using the spinner magnetometer. The archive-half data measured on the cryogenic magnetometer agree with discrete sample data, and we have no reason to question their validity.

Discrete samples were subjected to stepwise AF demagnetization using a DTech AF demagnetizer (model D-2000) capable of peak fields as high as 200 mT. Typically 12–15 AF demagnetization steps were used, with the peak field values selected according to sample coercivity. The residual magnetic field

at the demagnetizing position in this equipment was 5–50 nT, with the higher value apparently associated with vessel headings that are nearly east–west (the ambient field in this case is parallel to the mu-metal shield housing the instrument). Despite this low residual field, spurious magnetizations were nonetheless observed at high peak fields for some samples. At peak fields of >40 mT, samples were therefore typically demagnetized and measured twice (once after demagnetization along the sample +x, +y, and +z directions and again after demagnetization along the –x, –y, and –z directions) to identify and compensate for any spurious remanent magnetization acquisition caused by a bias field in the demagnetizing coil. An alternative method in which the last axis demagnetized was systematically varied was also used for some discrete sample demagnetizations.

Discrete samples were thermally demagnetized using a Schonstedt Thermal Specimen Demagnetizer (model TSD-1) capable of demagnetizing specimens up to 700°C. Each sample boat for thermal demagnetization included as many as nine samples, and sample orientations were varied at alternative steps to allow any interactions between adjacent samples to be identified. Samples were held at the desired temperature for 40 min and then cooled in a chamber with a residual magnetic field of <30 nT. Magnetic susceptibility was measured using a Bartington MS2F point magnetic susceptibility meter after every heating step to monitor thermal alteration of magnetic minerals during heating.

In addition to standard paleomagnetic measurements, the anisotropy of magnetic susceptibility was determined for all discrete samples using the KLY 4S Kappabridge with the software AMSSpin (Gee et al., 2008). The susceptibility tensor and associated eigenvectors and eigenvalues were calculated off-line following the method of Hext (1963). All bulk susceptibility values reported for discrete samples are based on a nominal 8 cm³ volume.

Inclination-only analysis

For azimuthally unoriented cores the simple arithmetic mean of inclination data will be biased to shallower values (e.g., Kono, 1980; McFadden and Reid, 1982; Arason and Levi, 2010). To compensate for this bias, we used the inclination-only statistics of Arason and Levi (2010) to calculate the overall mean inclination from discrete sample demagnetization data from each drill site, as well as the mean inclinations for each lithologic unit from the more abundant archive-half data. As one estimate, we simply calculate the inclination-only mean and associated α_{95} uncertainties (Arason and Levi, 2010) from all 2 cm PCA

directions (with misfit below the cutoff value) from a single lithologic unit. Alternatively, the same inclination-only technique may be applied by averaging all Fisher piece-average inclinations from a single lithologic unit. These two approaches provide similar results, differing primarily in the uncertainty estimates where n is small: the α_{95} values for the piece-average data are necessarily larger than those calculated from the greater number of 2 cm measurements. The former error estimate is likely more realistic because the individual 2 cm data points are not all statistically independent.

Although the Arason and Levi technique is more robust than previous inclination-only methods (e.g., Kono, 1980; McFadden and Reid, 1982), this technique nonetheless fails to converge under certain circumstances. For example, if inclinations are steep and the scatter is substantial or if dual polarities (also with steep inclination) are present, no maximum likelihood estimate is possible. If initially no solution was found, we recalculated with only the dominant polarity data if <10% of the data were of opposite polarity (splitting the data set arbitrarily at an inclination of 0°). For unit average inclinations based on 2 cm archive-half data, means are reported only for units with more than one inclination measurement. In the case of piece-average directions, single inclination measurements were retained because each typically represents the mean direction from multiple samples.

Downhole logging

Downhole logs are used to determine the physical, chemical, and structural properties of the formation penetrated by drilling. The data are rapidly collected, continuous with depth, and measured in situ; they can then be interpreted in terms of stratigraphy, lithology, mineralogy, magnetic characteristics, and geochemical composition of the penetrated formation. Where core recovery is incomplete or disturbed, log data may provide the only way to characterize the borehole section. Where core recovery is good, log and core data complement one another and may be interpreted jointly.

Downhole logs are sensitive to formation properties on a scale that is intermediate between those obtained from laboratory measurements on core samples and geophysical surveys. They are useful in calibrating the interpretation of geophysical site survey data (e.g., through the use of synthetic seismograms) and provide a necessary link for the integrated understanding of physical properties on all scales.

During Expedition 330, downhole measurements were taken in Holes U1374A and U1376A.

Wireline logging

During wireline logging, logs were made with a variety of Schlumberger logging tools and the third-party Göttingen Borehole Magnetometer (GBM) (Stevelling et al., 1991). These tools were combined into several tool strings that were run down the hole after coring operations were completed. Four wireline tool strings were used during Expedition 330 (Fig. F18; Table T11):

1. The triple combination (triple combo), which recorded density, porosity, electrical resistivity, and gamma ray;
2. The Formation MicroScanner (FMS)-sonic, which recorded gamma ray, microresistivity images of the borehole wall, and compressional and shear wave velocities;
3. The Ultrasonic Borehole Imager (UBI), which recorded transit times, amplitudes, and borehole radii; and
4. The GBM, which logged a three-component magnetic field.

The first three tool strings also contained a telemetry cartridge for communicating through the wireline to the Schlumberger data acquisition system on the drillship. The GBM communicates with its own dedicated acquisition unit on the drillship through the standard logging wireline.

In preparation for logging, the boreholes were flushed of debris by circulating viscous drilling fluid (sepiolite) mud mixed with seawater (approximate density ≈ 1.08 g/cm³) through the drill pipe to the bottom of the hole. The boreholes were reamed and displaced with heavy (approximate density ≈ 1.26 g/cm³) mud (barite). The bottom-hole assembly was pulled up to ~ 130 mbsf in Hole U1374A and ~ 80 mbsf in Hole U1376A. The tool strings were then lowered downhole by a seven-conductor wireline cable during sequential runs. A wireline heave compensator was employed to minimize the effect of ship heave on tool position in the borehole (see “[Wireline heave compensator](#)”). During each Schlumberger logging run, incoming data were recorded and monitored in real time on the MCM MAXIS logging computer. The tool strings were then pulled up at constant speed, typically 250–300 m/h, to provide continuous measurements as a function of depth of several properties simultaneously.

Logged formation properties and tool measurement principles

The logged properties and the methods by which they are measured are briefly described below. The main logs taken by the tools are listed in Table T12.

More detailed information on individual tools and their geological applications may be found in Serra (1984, 1986, 1989), Schlumberger (1989, 1994), Rider (1996), Goldberg (1997), Lovell et al. (1998), Ellis and Singer (2007), and Robinson et al. (2008). A complete list of acronyms for Schlumberger tools and measurement curves is available at www.slb.com/modules/mnemonics/index.aspx.

Natural radioactivity

The Hostile Environment Natural Gamma Ray Sonde (HNRS), a spectral gamma ray tool, uses two bismuth germanate scintillation detectors and five-window spectroscopy to determine concentrations of ^{40}K , ^{232}Th , and ^{238}U in the formation. The isotopes of these elements dominate the natural radiation spectrum. The HNRS filters out gamma ray energies <500 keV, eliminating sensitivity to bentonite or KCl in the drilling mud and improving measurement accuracy. The computation of the elemental abundances uses a least-squares method of extracting thorium, uranium, and potassium elemental concentrations from the spectral measurements.

Density and photoelectric effect

Formation density was determined with the Hostile Environment Litho-Density Sonde (HLDS), which contains a radioactive cesium (^{137}Cs) gamma ray source (622 keV) and far and near gamma ray detectors mounted on a shielded skid that is pressed against the borehole wall by a hydraulically activated decentralizing arm. Gamma rays emitted by the source undergo Compton scattering, which involves the transfer of energy from the gamma rays to the electrons in the formation via elastic collision. The number of scattered gamma rays that reach the detectors is directly related to the density of electrons in the formation, which is in turn related to bulk density. Porosity may also be derived from bulk density if the matrix density is known.

The HLDS also measures photoelectric absorption as the photoelectric effect. Photoelectric absorption of gamma rays occurs when their energy is reduced below 150 keV after being repeatedly scattered by electrons in the formation. Because photoelectric effect depends on the atomic number of the elements in the formation, it also varies according to the chemical composition of the minerals present and therefore can be used to identify some minerals (for example, the photoelectric effect of calcite is 5.08 barns per electron [b/e^-] and that of quartz is 1.81 b/e^-). Good contact between the tool and borehole wall is essential for good logs. Poor contact typically results in underestimation of density values.

Porosity

Formation porosity was measured with the Accelerator Porosity Sonde (APS), which incorporates a minitron neutron generator that produces fast (14.4 MeV) neutrons and five neutron detectors (four epithermal and one thermal) positioned at different spacings from the minitron. The tool's detectors count neutrons that arrive at the detectors after being scattered and slowed by collisions with atomic nuclei in the formation. The near detector is centered in the tool and is used to normalize the count rates for differences in the minitron source. The remaining detectors are decentered, and neutron backshielding is used to focus them toward the formation to minimize the effect of the borehole environment.

Neutrons leaving the tool travel through the surrounding borehole and formation and interact primarily with hydrogen atoms present in the common formation fluids. Because neutrons and hydrogen atoms have about the same mass, successive collisions rapidly reduce the energy of the neutrons to the thermal energy level of the formation (0.025 eV). Because water contains about the same quantity of hydrogen per unit volume, the detector count-rate ratios can be calibrated in terms of liquid-filled porosity in clean formations. However, because hydrogen bound in minerals such as clay or in hydrocarbons also contributes to the measurement, the raw porosity value is often an overestimate.

A mineral's ability to absorb thermal neutrons is defined as its capture cross section, Sigma (Σ_c). Formations and formation fluids containing chlorine atoms are the most effective capturers of thermal neutrons. Thus, the rate of thermal neutron decay in the formation can be measured and used to differentiate between hydrocarbons in the pore space and salt water. Sigma is measured in capture units. Higher values of Sigma equate to a greater ability to capture thermal neutrons.

Electrical resistivity

The phasor Dual Induction Tool (DIT) was used to measure electrical resistivity. This tool provides three measures of electrical resistivity, each with a different depth of investigation into the formation. The two induction devices (deep and medium depths of penetration) transmit high-frequency alternating currents through transmitter coils, creating magnetic fields that induce secondary currents in the formation. These currents produce a new inductive signal, proportional to the conductivity of the formation, which is measured by the receiving coils. The measured conductivities are then converted to resistivity (in units of ohm-meters). For shallow-penetration re-

sistivity, the current necessary to maintain a constant drop in voltage across a fixed interval is measured, which is a direct measurement of resistivity. Typically, igneous minerals found in crustal rocks are electrical insulators, whereas sulfide and oxide minerals, as well as ionic solutions like pore water, are conductors. Electrical resistivity, therefore, can be used to evaluate porosity (via Archie's law) and fluid salinity.

Acoustic velocity

The Dipole Shear Sonic Imager (DSI) measures the transit times between sonic transmitters and an array of eight receivers. It combines replicate measurements, thus providing a direct measurement of sound velocity through formations that is relatively free from the effects of formation damage and an enlarged borehole (Schlumberger, 1989). Along with the monopole transmitters found on most sonic tools, it also has two crossed-dipole transmitters, which allow the measurement of shear wave velocity in addition to compressional wave velocity. Dipole measurements are necessary to measure shear velocities in slow formations whose shear velocity is less than the velocity of sound in the borehole fluid. Such slow formations are typically encountered in deep ocean drilling (e.g., for Expedition 330 the sediments overlying igneous basement).

Formation MicroScanner

The FMS tool provides high-resolution electrical resistivity-based images of borehole walls. The tool has four orthogonal arms and pads, each containing 16 button electrodes that are pressed against the borehole wall during the recording. The electrodes are arranged in two diagonally offset rows of eight electrodes each. A focused current is emitted from the button electrodes into the formation, with a return electrode near the top of the tool. Resistivity of the formation at the button electrodes is derived from the intensity of current passing through the button electrodes. Processing transforms these measurements into oriented high-resolution images that reveal the geologic structures of the borehole wall. Further analysis can provide measurements of dip and direction (azimuth) of planar features in the formation.

The development of the FMS tool has added a new dimension to wireline logging (Luthi, 1990; Salimullah and Stow, 1992; Lovell et al., 1998). Features such as vesicles, veins, fractures, and volcanoclastic breccia can be resolved, and the fact that the images are oriented means that fabric analysis can be carried out and structural feature (e.g., fracture) orientations can

be measured. If the same features in these high-resolution electrical images can be identified in the recovered core samples, individual core pieces can be reoriented with respect to true north.

The maximum extension of the caliper arms is 38.1 cm (15 inches). For holes with a diameter larger than 38.1 cm, pad contact at the end of the caliper arms will be inconsistent, and the FMS images may appear out of focus and too conductive. Irregular (rough) borehole walls will also adversely affect the images if contact with the wall is poor. Standard procedure is to make two full passes up the borehole with the FMS to maximize the chance of getting full borehole coverage with the pads.

Ultrasonic Borehole Imager

The UBI features a high-resolution transducer that provides acoustic images of the borehole wall. The transducer emits ultrasonic pulses at a frequency of 250 or 500 kHz (low and high resolution, respectively) that are reflected at the borehole wall and then received by the same transducer. The amplitude and traveltime of the reflected signal are determined. Continuous rotation of the transducer and the upward motion of the tool produce a complete map of the borehole wall. The amplitude depends on the reflection coefficient of the borehole fluid/rock interface, the position of the UBI tool in the borehole, the shape of the borehole, and the roughness of the borehole wall. Changes in the borehole wall roughness (e.g., at fractures intersecting the borehole) are responsible for the modulation of the reflected signal. Therefore, fractures or other variations in the character of the drilled rocks can be recognized in the amplitude image. The recorded traveltime image gives detailed information about the shape of the borehole, which allows calculation of one caliper value of the borehole from each recorded traveltime. Amplitude and traveltime are recorded together with a reference to magnetic north by means of a magnetometer (General Purpose Inclination Tool [GPIT]), permitting the orientation of images. If features (e.g., fractures) recognized in the core are observed in the UBI images, orientation of the core is possible. The UBI oriented images can also be used to measure stress in the borehole through identification of borehole breakouts and slip along fault surfaces penetrated by the borehole (Paillet and Kim, 1987). In an isotropic, linearly elastic rock formation that is subjected to an anisotropic stress field, drilling a subvertical borehole causes breakouts in the direction of the minimum principal horizontal stress (Bell and Gough, 1983). Because of time constraints, the UBI was only run in Hole U1374A.

Borehole inclination and magnetic field measurement

Three-component acceleration and magnetic field measurements were made with the GPIT. The primary purpose of this tool, which incorporates a three-component accelerometer and a three-component magnetometer, is to determine the acceleration and orientation of the FMS-sonic and UBI tool strings during logging. This information allows the FMS and UBI images to be corrected for irregular tool motion and the dip and direction (azimuth) of features in the images to be determined. The GPIT was also run on the triple combo tool string in order to provide data to optimize the wireline heave compensator before logging began and to acquire the best possible downhole data. The GPIT is run with other tools on the triple combo and FMS-sonic tool strings that can carry remanent or induced magnetization; therefore, its magnetic measurements can be affected. However, on the FMS-sonic tool string the GPIT has greater nonmagnetic insulation from the other tools, which greatly reduces the effects on its magnetic measurements.

Göttingen Borehole Magnetometer

The GBM was designed and developed in 1989 by the Geophysical Institute of the University of Göttingen, Germany (Fig. F19A). The tool consists of three fluxgate sensors that log the horizontal (x and y) and the vertical (z) components of magnetic flux density (Stevelling et al., 1991). In the first version of the tool, orientation was determined by two inclinometers, which still can be used to measure deviation of the tool from vertical. In 2001 the first fiber-optic gyro was installed in the GBM to measure rotations around the vertical axis of the tool. Since then, two additional angular rate sensors have been added to the tool to monitor variations around the tool's x - and y -axes during a logging run.

The tool connects directly to the Schlumberger cable head and is deployed with a centralizer and two sinker bars (a Schlumberger sinker bar and a new virtually nonmagnetic aluminum sinker bar, the latter being especially developed for Expedition 330 by the Scripps Institution of Oceanography). The nonmagnetic sinker bar was found to be essential following extensive tests in August 2010 in Houston, Texas. The tests revealed that the Schlumberger sinker bar and the centralizer both carried nonnegligible remanent magnetization (with the centralizer being much more magnetic than the sinker bar) and, together with induced magnetization, caused an error of up to 350 nT in the magnetic measurements of the GBM when used in a common tool string configuration. The truly nonmagnetic aluminum sinker

bar reduced this influence to <50 nT by almost doubling the distance of the magnetometers from the other parts of the tool string. The Schlumberger sinker bar had to be deployed in conjunction with the nonmagnetic aluminum sinker bar to increase the weight of the tool string, and the centralizer was necessary to both center the tool in the borehole and reduce tool rotation. The GBM housing is made of low-magnetic monel and is not affected by pressures or temperatures up to 70 MPa and 100°C, respectively. Specifications are listed in Table T13.

The GBM was deployed during Expedition 330 because the tool's fiber-optic gyros allow independent determination of both inclination and declination of the magnetic field in the borehole (and hence estimation of declination and inclination of the magnetization of penetrated lava flows). In addition, the better quality of the GBM magnetic data, especially the low magnetic influence of the other parts of the tool string (thanks to the aluminum sinker bar), can possibly help to better orient the FMS and UBI data (postexpedition). The fluxgate magnetometers incorporated in the GPIT are sufficient for orienting the FMS tool string; however, these sensors have relatively poor sensitivity (50 nT) and, more importantly, substantial (~1000 nT) offsets that limit interpretation of the data (e.g., Ito et al., 1995). The fluxgate magnetometers in the GBM have better resolution (12 nT) and are well calibrated. For example, when the ambient field was measured with the GBM above the HSDP-2 drill hole on Hawaii (Stevelling et al., 2003), the inclination of 36.5° compares well with the International Geomagnetic Reference Field inclination of 36.6°, and the measured total field was compatible with that determined by aeromagnetic surveys.

GBM angular rate sensors

LITEF miniature fiber-optic rate sensors were used to provide angular rate output during the entire run (downlog and uplog) of the GBM. The tool contains three of these gyros, each of which has a small volume and low weight and requires very little power (2 VA) (Fig. F19B). Free from gravity-induced errors and with no moving parts, the sensors are insensitive to shock and vibration. The rate sensors are unconventional gyros because they do not have a spinning wheel. The sensor detects and measures angular rates by measuring the frequency difference between two contra-rotating light beams. The light source is a superluminescent diode, and its broad spectrum provides light with a short coherence length to keep the undesirable backscattering effects in the optical path to sufficiently low levels. The beam is polarized, split, and phase modulated. The output light travels

through a 110 m long fiber coil. The light travels to the detector, which converts the light into an electronic output signal. When a gyro is at rest, the two beams have identical frequencies. When the gyro is subjected to an angular turning rate around an axis perpendicular to the plane of the two beams, one beam then has a greater optical path length and the other beam has a shorter optical path length. Therefore, the two resonant frequencies change, and the frequency differential is measured by optical means, resulting in a digital output. Readings are output at 1 Hz. The angular rate, sampled at 5 Hz, is a function of time and corresponds to the accumulated angle.

The angular rate measured by the sensor is influenced by the Earth's rotation, which depends on latitude (ϑ) and varies from 15.04°/h at the poles to 0°/h at the Equator (Fig. F19C). From Equator to pole, Earth's measured rotation increases by $\sin(\vartheta)$. To obtain the rotation rate about an inertial system, the effect of Earth's rotation must be eliminated. To do so, the orientation of the tool relative to the Earth's reference frame at the beginning of a measurement has to be known exactly. The x -gyro of the GBM was aligned with the axis of the ship using a scope mounted to the tool and a sighting plate positioned in the center of the helideck at the aft of the ship. Knowing that the tool was identically oriented with the ship, information from the ship's gyro and two GPS antennas was then used to determine the heading of the ship (at the time of sighting) and thus the orientation of the tool at the start of logging. This procedure was repeated at the end of each logging run to compare the true heading of the gyro with the heading calculated by the data-processing algorithm. This was done to check for errors in the reorientation procedure. If the corrected rotation rate around each axis is known, the orientation of the tool can be derived as a function of depth from the rotation history, and thus the three components of the magnetic field can be calculated for every data point collected by the GBM.

The maximum operation temperature for the fiber-optic gyros is 70°C. The gyros have a temperature-dependent drift that is lowest between 35° and 50°C, so the gyros were heated. The temperature of the gyros was measured during the logging run, and the temperature drift was corrected for during data processing. However, depending on the resistance of the wireline, the voltage received by the tool is not sufficient to heat against the cold seawater. As a result, during Expedition 330 the temperature of the gyros typically decreased to values below 35°C but never fell below 28°C, which is still an acceptable temperature range (Fig. F20). Data were acquired from the tool using GBMlog software (written by E. Steveling,

University of Göttingen) and processed with GBM-datenverarbeitung software (developed by S. Ehmann, University of Braunschweig).

Logging data quality

The principal influence on log data quality is the condition of the borehole wall. If the borehole diameter is variable over short intervals (resulting from washouts during drilling or ledges caused by layers of harder material) the logs from some tools (e.g., FMS, density, and porosity tools) may be degraded. Deep (0.23–1.5 m) investigation measurements such as resistivity and sonic velocity, which do not require contact with the borehole wall, are generally less sensitive to borehole conditions. Very narrow bridged sections also cause irregular log results. The quality of the borehole is improved by minimizing the circulation of drilling fluid while drilling, flushing the borehole to remove debris, performing a full wiper trip, and logging as soon as possible after drilling and conditioning are completed.

The quality of the depth determination depends on a series of factors. The depth of the wireline-logged measurement is determined from the length of the logging cable played out at the winch on the ship. The seafloor is identified on the natural gamma ray log by the abrupt decrease in gamma ray count at the sediment/water interface ("mudline"). Discrepancies between drillers and core depth and wireline log depth occur because of core expansion, incomplete core recovery, incomplete heave compensation, and drill pipe stretch, in the case of drillers depth. In the case of log depth, discrepancies occur because of incomplete heave compensation, incomplete correction for cable stretch, and cable slip. Tidal changes in sea level also have an effect. To minimize the wireline tool motion caused by ship heave, a hydraulic wireline heave compensator (see below) was used to adjust the wireline length for rig motion during wireline logging operations.

Wireline heave compensator

The new wireline heave compensator system installed during the recent refit (first used during Expedition 320T in February 2009) is designed to compensate for the vertical motion of the ship and maintain a steady motion of the logging tools. It uses vertical acceleration measurements made by a motion reference unit located under the rig floor near the ship's center of gravity to calculate the vertical motion of the ship. It then adjusts the length of the wireline by varying the distance between two sets of pulleys through which the cable passes. Real-time measurements of uphole (surface) and downhole acceleration are made simultaneously by the

motion reference unit and the GPIT tool, respectively. A software package developed by Lamont-Doherty Earth Observatory allows these data to be analyzed and compared in real time, displaying the actual motion of the logging tool string and enabling monitoring of the efficiency of the compensator. In addition to an improved design and smaller footprint compared to the previous system, the location of the wireline heave compensator with the winch unit on the starboard side of the derrick contributes to a significant reduction in the time necessary to prepare for logging operations.

Logging data flow and log depth scales

Data for each wireline logging run were monitored in real time and recorded using the Schlumberger MAXIS 500 system. The initial logging data were referenced to the rig floor (wireline log depth below rig floor). After logging was completed, the data were shifted to a seafloor reference (wireline log depth below seafloor), which was based on the step in gamma radiation at the sediment/water interface. These data were made available to the science party as a provisional data set.

The data were transferred on shore to Lamont-Doherty Earth Observatory, where standardized data processing took place. The main part of the processing is depth matching to remove depth offsets between data from different logging runs, which results in a new depth scale (wireline log matched depth below seafloor). In addition, corrections are made to certain tools and logs, documentation for the logs (with an assessment of log quality) is prepared, and the data are converted to ASCII for the conventional logs and GIF for the FMS images. Schlumberger Geo-Quest's GeoFrame software package is used for most of the processing. The data were transferred back to the ship within a few days of logging, and this processed data set was made available to the science party (in ASCII and DLIS formats) through the shipboard IODP logging database.

Core-log-seismic integration

GeoFrame's IESX seismic interpretation software package was available during Expedition 330 to display site-survey seismic sections acquired before the expedition. Velocity and density logs, together with equivalent measurements made on core in the physical properties laboratory, can be used to create synthetic seismograms. The depth-traveltime relation must be adjusted until the features in the synthetic seismogram match the features in the seismic section. In this way, lithostratigraphic units in the core

may be correlated with reflectors and sequences in the seismic section. Should the quality of the shipboard sonic and density logs be sufficient, synthetic seismograms can be produced postexpedition.

Microbiology

Starting in the 1990s, microbiologists participating in ODP and IODP expeditions have documented the presence of microbial life in deeply buried sediment and the basaltic basement (Fisk et al., 1998; Parkes et al., 1994). Active microbial life has been detected as deep as 1626 mbsf (Roussel et al., 2008), and the introduction of molecular biology into marine ecology has led to great advances in our understanding of microbial life below the seafloor (Biddle et al., 2008; Cowen et al., 2003; Inagaki et al., 2006; Mason et al., 2010). Much of the microbiology performed during ODP and IODP expeditions has concentrated on sediment (e.g., ODP Leg 201 to the Peru margin), with the notable exception of expeditions to the Juan de Fuca Ridge (Cowen et al., 2003; Lever et al., 2006) and Atlantis Massif (Mason et al., 2010). Sampling for microbiological studies during Expedition 330 focused primarily on the microbiology of basement rocks. Differences in microbial population between the overlying sediment and volcanoclastic layers and the basaltic basement were also targeted. Drilling during Expedition 330 provided a unique sample set because at several sites there is a thin layer of sediment overlying volcanoclastic breccia, followed by igneous basement. As much as 505 m of basement was drilled at Site U1374, providing one of the most complete sets of igneous basement samples to date for microbiological investigation.

Sediment sampling

Whole-round core samples are required for microbiological studies to avoid contamination introduced by sample handling before and during the core splitting process. For sediment samples, whole rounds were sampled on the catwalk. After the core liner was cut, whole-round sediment samples were cut off with a sterile spatula, transferred onto a precombusted (450°C for 2 h) aluminum foil sheet, and immediately transported to the cold room in the microbiology laboratory, where they were processed.

Sediment samples were collected for molecular biology and cell counts. One of the goals of this sampling was to trace the change, if any, in microbial community composition across the sediment/basement transition. The sampling was carried out on unconsolidated sediment recovered from the uppermost ~10–20 m at each drill site where such sediment was recovered.

One 5 cm whole round of sediment was collected from each core in the 5 cm interval immediately adjacent to the core catcher. Once the samples were transported to the microbiology cold room, a sterile syringe with the top cut off (creating a cookie cutter type of coring device) was used to collect 2 cm³ for cell counts, 2 cm³ for carbon-hydrogen-nitrogen-sulfur and total organic carbon analyses (see “[Geochemistry](#)”), and ~20 cm³ for molecular biological work. For cell counts, 2 cm³ of sediment was added to 8 mL of 2% formalin in 3% NaCl (sterile filtered) in a 15 mL Falcon tube.

Molecular biology samples were collected in sterile 5 mL centrifuge tubes and frozen at –80°C for shore-based analysis. After microbiology sampling, an extruded polystyrene foam plug was placed in the void left in the center of the whole round, preventing the collapse of its outer rim (which was likely contaminated by drilling fluids and therefore not used for microbiological analysis) and allowing it to be returned to the curator for further sampling by other laboratory groups.

Igneous rock sampling

For volcanoclastic breccia and basement samples, whole rounds were selected in the core splitting room and collected from the core liner onto precombusted (450°C for 2 h) aluminum foil before the core was cleaned with water. Samples were chosen with a petrologist present to ensure that no samples critical to the main objectives of the cruise were lost because of microbiological sampling, which destroys nearly the entire sample. Before samples were transported to the microbiology laboratory, photographs of each side of the whole-round sample were taken while the sample was on the combusted foil. During sampling and photography, samples were handled with gloved hands only.

Prior work has shown that the interiors of rock cores are generally free from contamination (Lever et al., 2006). Therefore, efforts were taken to sample only the core interiors. Sections that showed some sign of alteration or fluid flow conduits were specifically chosen because these are likely locations for microbial life. Microbiology samples on average were 5–10 cm long. All samples were divided into subsamples for cell counts, molecular biological analyses (DNA and RNA extraction, to be carried out on shore), and in situ stable isotope analysis ($\delta^{34}\text{S}$ and $\delta^{13}\text{C}$). For some samples, stable isotope addition bioassays and cultivation experiments were also performed.

The undisturbed whole round was washed three times with artificial seawater in a fresh, resealable storage bag before subsampling to avoid contamination from drilling fluids. Next, the rock was split

with a sterile chisel and sampled from the interior. For those samples on which culturing or stable isotope bioassays were to be performed on board, a portion of the sample was sectioned off immediately, and placed in a N₂ environment in a glove bag or the anaerobic chamber to minimize exposure of anaerobic cells to O₂ while the rock was being processed. These precautions were taken because basement rocks at Sites 801, 1272, and 1274 have been shown to be anaerobic based on detection of sulfate reduction, a strictly anaerobic process (Alt et al., 2007; Rouxel et al., 2008). Therefore, we assumed that the basement rocks here were also anaerobic. Whenever pieces of the whole round remained, including the outer portions of the rock, they were returned to the curator to be placed back into the working and archive sections of the core.

Molecular biology

Samples were placed in 5 mL autoclaved centrifuge tubes and immediately stored at –80°C for DNA analysis or were placed in 15 or 50 mL centrifuge tubes with LifeGuard Soil Preservation Solution (MoBio Laboratories, Inc., Carlsbad, CA) and held at 4°C overnight before freezing at –80°C for RNA analysis. LifeGuard protects the viability of microbial cells while keeping them in stasis, allowing for efficient DNA and RNA extractions from samples collected in the field. These samples will be analyzed during postexpedition research.

Stable isotope analysis

Analysis of in situ $\delta^{34}\text{S}$ fractionation in the rocks can indicate the presence of microbially mediated sulfate reduction (Alt et al., 2007; Rouxel et al., 2008), even in basalts older than 50 Ma. Analysis of in situ $\delta^{13}\text{C}$ fractionation provides insight into the production mechanism of carbon present in the rocks (Mason et al., 2010). Samples for stable isotope analysis were subsamples of the whole round sampled for molecular biology. At least 20 cm³ of rock chunks were placed in Whirl-Pak bags and set in the anaerobic chamber in the cold room for a few hours, after which the bags were sealed in the chamber (so that the atmosphere of the closed bag remained anaerobic) and stored at 4°C. Isotopic analysis will be carried out as part of postexpedition research. Alteration rims were specifically targeted for this work because they are more likely to harbor microbes (Fisk et al., 1998).

Cultivation experiments

Based on prior work with both subsurface and surface-exposed basalts, the functional groups of microbes likely to be found in the subsurface basalts

along the Louisville Seamount Trail include sulfur oxidizers, sulfate reducers, methanogens, iron reducers, and iron oxidizers (Cowen et al., 2003; Mason et al., 2009, 2010; Santelli et al., 2009). Media targeting enrichment of these groups were prepared prior to the expedition and used to culture subsurface microbes. Details of the media recipes can be found in Table T14. Samples used for culturing were maintained in an anaerobic environment following collection and splitting of whole rounds into rock fragments for culturing and molecular biology sampling. Rock fragments were placed in 5 mL serum vials filled with different media and sealed. The vials were kept at 4°C (the assumed temperature of the volcanically inactive subsurface seamount environment) until the end of the expedition and then were shipped in refrigerated containers for onshore assessment of growth. If any enrichments prove successful, further steps will be taken to isolate and characterize pure cultures of microorganisms during postexpedition research.

Stable isotope bioassays

¹³C-labeled bicarbonate was used to measure incorporation rates of inorganic carbon into subsurface microbes as an indicator of autotrophic production in this environment. In addition, ¹³C-labeled glucose and acetate were used to measure incorporation rates of organic carbon by heterotrophic microbes, ¹⁵N-labeled ammonia and nitrate were used to estimate rates of N uptake by subsurface microbes, and ³⁴S elemental sulfur was used to measure rates of sulfur cycling.

In each experiment, 100 mL of artificial seawater (Sigma-Aldrich; St. Louis, Missouri [USA]) modified with 50 µM sodium nitrate, 3 µM potassium phosphate, and 0.5 µM ammonium chloride was added to a precombusted serum vial. We herein refer to this as the basic seawater medium. Sigma sterile seawater is collected from surface water in the Gulf Stream, which is low in N and P. However, deep seawater has N and P concentrations closer to those of the modified Sigma sterile seawater. Note that the composition of pore water in the subsurface rocks collected during Expedition 330 is unknown, so we chose to simulate typical deep seawater. Enough rock chips were added to cover the bottom of the vial. This amount depended on the amount obtained during sample processing.

A more persuasive “enhanced extraction” method for obtaining large amounts of uncontaminated rock samples for these bioassays was developed during sample processing of Sample 330-U1374A-15R-2, 79–

89 cm. For all other (nonstable isotope addition bioassay) microbiology sampling during Expedition 330, subsamples were retrieved only from the center-most portion of the whole-round sample to avoid potential contamination from drilling fluids on the outside of the whole-round sample. This method provided enough uncontaminated sample suitable for cell counts, culturing experiments, and molecular biology analysis. However, analysis of stable isotope addition bioassays requires more rock than can be collected solely from the center of the whole-round sample. Therefore, the following enhanced extraction method was carried out on all samples for stable isotope analyses from Holes U1374A–U1377A:

1. The whole-round sample was rinsed three times with sterile filtered seawater in the same manner as all other microbiology samples.
2. The outside of the rock was flamed with a propane blowtorch by laying the whole round on its side in the rock box, flaming it for 5 s, and then rotating it. All four quadrants of the rock were flamed to ensure the entire outside of the whole round was sterilized. The top and bottom of the whole round were also flamed for 5 s.
3. An ethanol- and flame-sterilized chisel was used to remove the outer portion of the whole round, and rock chips from the inside of the rock were selected and preserved for cell counts and molecular biological analysis. Sections of the whole round were also preserved for shore-based analysis of in situ ³⁴S and ¹³C.
4. The remainder of the rock was broken into rock chips ~2–3 cm in diameter with the sterilized chisel. These chips were then placed in unused Whirl-Pak bags.
5. The Whirl-Pak bags were placed between two autoclaved polytetrafluoroethylene Delrin plugs inside an autoclaved section of core liner (~20 cm long) and crushed using a Spex 3624B X-Press hydraulic press, with pressure not exceeding 2 tons.
6. The rocks were removed from the bags and collected in unused 50 mL centrifuge tubes for transportation to the radiation van, where they were used in the stable isotope addition bioassays.

The advantages of the enhanced extraction method are twofold. First, sterilizing the outside of the entire whole round allows samples from all parts of the rock to be collected with minimal fear of contamination, which allows collection of a greater volume of rock than that which could be obtained solely from the interior of the whole-round sample. Although some of the rock chips collected (those pieces containing portions of the outside of the whole round)

will contain no live microbes because of the sterilization, the gain of volume versus the loss of cells makes this a valuable sampling method. Second, using the hydraulic press allows a large volume of small rock chips to be collected, which is important because the mouth of the serum vial used for these incubations is only 17 mm wide. Enough rock material was collected using the enhanced extraction method to add 15–30 cm³ per serum vial for bioassays, starting with Site U1374.

Following sampling using the enhanced extraction method, two different sets of treatments were prepared for the stable isotope bioassays: (1) ¹³C bicarbonate, ¹⁵N ammonia, and ³⁴S sulfate, which targeted metabolic rates specifically among autotrophic microbes, and (2) ¹³C glucose, ¹³C acetate, ¹⁵N nitrate, and ³⁴S, which targeted metabolic rates among heterotrophic microbes. Varying concentrations of each stable isotope were added during the expedition as experimental strategies were adjusted. For the range of concentrations for each label, see Table T15.

After a stable isotope label was added to each vial, the vials were sealed with a rubber stopper and crimped. Incubations were kept at 4°C until termination. At the end of each incubation, 5 mL of fluid was removed from each vial with a syringe and transferred to a crimp-sealed 20 mL serum vial containing 1 mL of 2 g/30 mL NaOH solution (for dissolved inorganic carbon), and the excess fluid was poured into a 50 mL Falcon tube. The remaining rock chips were collected in a separate Falcon tube.

For each stable isotope bioassay, there were four time points (t_0 – t_3). The first (t_0) was when the rock was collected during routine microbiology sampling, which provided the background stable isotope fractionation value. No manipulation of this rock was performed after sampling. The remaining time points were taken from the incubation vials as described above. The second time point (t_1) was taken after 2 weeks (most were processed on the ship), the third time point (t_2) was taken after 2 months, and the fourth time point (t_3) was taken after 6 months. Both t_2 and t_3 were sent to shore, and the incubations will be terminated during shore-based research. The long duration of the experiments allows for detection of potentially slow metabolisms of subsurface microbes.

Cell counts

During Expedition 330, we attempted to enumerate cell abundances for the basaltic rock samples to determine biomass concentrations in the subsurface basalt environment. Crushed and powdered basalt (1 cm³) samples were fixed with 4 mL of 4% parafor-

maldehyde in 3% NaCl at 4°C overnight. The fixed basalt suspensions were then subjected to cell counting according to the following protocol:

1. After vigorous stirring of the paraformaldehyde-fixed slurry, 100 µL of the suspension was immediately dispensed in 10 mL of filtered 1× phosphate-buffered saline (PBS) buffer (pH 7.4).
2. The second suspension was placed in an ultrasonic bath for 30 s.
3. The ultrasonically treated suspension was filtered through a 25 mm diameter, 0.2 µm pore size black polycarbonate filter underlain by 25 mm diameter, 0.45 µm pore size cellulose.
4. Cells on the polycarbonate filter were stained with filtered 1× SYBR Green I (Invitrogen; Ann Arbor, Michigan [USA]) DNA stain in filtered 1× tris-EDTA (TE) buffer for 5 min.
5. The stained filter was washed twice with 5 mL of filtered 1× PBS buffer.
6. The washed filter was mounted on a slide with one drop of immersion oil and covered with a cover glass.
7. The SYBR-stained cells were directly observed by using a Zeiss Axiophot epifluorescence microscope with a band-path filter slit (excitation at 470 nm; fluorescence > 515 nm) at 1000× magnification (100× objective; 10× eyepiece).

For each cell count, at least 20 microscopic fields were observed, and cell-shaped forms that produced bright green fluorescence were enumerated as cells.

The minimum detection limit was estimated by counting blank filter samples that were treated with 100 µL of filtered 1× PBS with 4% paraformaldehyde, as described above. Cell numbers in the blank filters were calculated as the average of all blanks processed during the expedition. The minimum detection limit was set to be the blank value plus three times the standard deviation. For completely negative control samples, crushed basalt pieces were combusted at 500°C for 3 h and then counted using the same method.

Unfortunately, shipboard cell counts on rock samples proved impossible because of a combination of fluorescence from the rocks themselves and focusing difficulties caused by ship movement. These two factors made it extremely difficult to distinguish between microbial cells and rock particles. We will endeavor to develop successful counting methods for subsurface rock samples during postexpedition research.

Quantitative polymerase chain reaction (qPCR), a modification of classic PCR, is essentially a fluorogenic assay used to quantify the number of target genes, and hence cells, in a given environmental

sample. During postexpedition research, qPCR will be applied to the samples collected. Then the two biomass estimation methods (cell counts and qPCR) will be compared (Einen et al., 2008; Santelli et al., 2008).

Contamination testing of drilling fluids

As part of the drilling process, a huge amount of surface seawater is injected into each borehole and is the major source of contamination with microorganisms in the cores collected. As a check for contamination, the microbial composition of the drilling fluid (surface ocean water) was assessed, and organisms present in both the drilling fluid and rock samples will be considered a sign of contamination. These organisms will be presented as contaminants, not subsurface residents. If there are any samples in which all of the organisms detected were also detected in the drill fluid, these samples will not be included in further analyses. Although it is possible that some species may be present both in surface seawater and the subsurface biosphere, we feel it will be more informative and conclusive to focus on microbes known to be present in subsurface samples only. Water samples were collected directly from the injection pipe in sterile bottles with screw caps and were handled using sterile equipment. Microorganisms present in the drilling fluid were extracted by filtration using a vacuum pump through 0.2 μm pore polycarbonate filters. Filters were frozen in cryotubes at -80°C for shored-based DNA extraction and analysis.

Fluorescent microsphere contamination testing

Bags of yellow-green fluorescent microspheres (Fluoresbrite carboxylate microspheres; Polysciences, Inc., 15700) with a diameter of $0.52 \pm 0.01 \mu\text{m}$ were occasionally used (i.e., for 1–2 cores per site) as a particulate tracer that mimics the movement and dispersal of microbial cells in the drill pipe during coring. The microspheres were then counted in core samples, in drill fluid caught as the drill core arrived on the rig floor, and in each of three sterile seawater rinses of the whole-round samples.

The concentration of microspheres was set at 10^{10} spheres/mL (Smith et al., 2000), and the microspheres were deployed in Whirl-Pak bags containing 40 mL of microsphere suspension in deionized water (2×10^{11} microspheres in a 40 mL bag). The bag was then heat-sealed, leaving some extra plastic (not filled with beads) at each end. By attaching the loose plastic ends using para-aramid synthetic cord, the bag was wedged into a shim above the core catcher

and stretched across the throat of the core barrel. Cores were consequently forced to burst through the bead bag when a core was taken.

The microspheres are highly fluorescent (458 nm excitation; 540 nm emission) and appear bright green when they are observed by epifluorescence microscopy (Smith et al., 2000). Concentrations of fluorescent microspheres in core samples were quantified using a Zeiss Axiophot epifluorescence microscope fitted with a mercury lamp (HBO 100 W), a blue filter set, and a 100 \AA Plan-NEOFLUAR oil-immersion objective. Nonfluorescent immersion oil was used for all observations. Aliquots (100 μL) of the crushed rock suspension or sediment slurry were re-suspended in 10 mL of filtered $1\times$ PBS solution and filtered onto black, 25 mm diameter polycarbonate filters (0.2 μm pore size) in a filtration tower. The filters were then mounted on microscope slides with a drop of nonfluorescent immersion oil and covered with a coverslip. The microspheres on the filter were then counted using the epifluorescence microscope. Microsphere abundance on the filters was determined by averaging the total number seen in at least 20 randomly selected fields of view.

References

- Agnini, C., Fornaciari, E., Raffi, I., Rio, D., Röhl, U., and Westerhold, T., 2007. High-resolution nannofossil biochronology of middle Paleocene to early Eocene at ODP Site 1262: implications for calcareous nannoplankton evolution. *Mar. Micropaleontol.*, 64(3–4):215–248. doi:10.1016/j.marmicro.2007.05.003
- Agnini, C., Muttoni, G., Kent, D.V., and Rio, D., 2006. Eocene biostratigraphy and magnetic stratigraphy from Possagno, Italy: the calcareous nannofossil response to climate variability. *Earth Planet Sci. Lett.*, 241(3–4):815–830. doi:10.1016/j.epsl.2005.11.005
- Alt, J.C., Shanks, W.C., III, Bach, W., Paulick, H., Garrido, C.J., and Beaudoin, G., 2007. Hydrothermal alteration and microbial sulfate reduction in peridotite and gabbro exposed by detachment faulting at the Mid-Atlantic Ridge, $15^{\circ}20'N$ (ODP Leg 209): a sulfur and oxygen isotope study. *Geochem., Geophys., Geosyst.*, 8(8):Q08002–Q08023. doi:10.1029/2007GC001617
- Arason, P., and Levi, S., 2010. Maximum likelihood solution for inclination-only data in paleomagnetism. *Geophys. J. Int.*, 182(2):753–771. doi:10.1111/j.1365-246X.2010.04671.x
- Aubele, J.C., Crumpler, L.S., and Elston, W.E., 1988. Vesicle zonation and vertical structure of basalt flows. *J. Volcanol. Geotherm. Res.*, 35(4):349–374. doi:10.1016/0377-0273(88)90028-5
- Bach, W., Erzinger, J., Alt, J.C., and Teagle, D.A.H., 1996. Chemistry of the lower sheeted dike complex, Hole 504B (Leg 148): influence of magmatic differentiation and hydrothermal alteration. In Alt, J.C., Kinoshita, H.,

- Stokking, L.B., and Michael, P.J. (Eds.), *Proc. ODP, Sci. Results*, 148: College Station, TX (Ocean Drilling Program), 39–55. doi:10.2973/odp.proc.sr.148.114.1996
- Backman, J., 1984. Late Paleocene to middle Eocene calcareous nannofossil biochronology from the Shatsky Rise, Walvis Ridge and Italy. *Palaeogeogr., Palaeoclimatol., Palaeoecol.*, 57(1):43–59. doi:10.1016/0031-0182(86)90005-2
- Backman, J., 1987. Quantitative calcareous nannofossil biochronology of middle Eocene through early Oligocene sediment from DSDP Sites 522 and 523. *Abh. Geol. Bundesanst. (Austria)*, 39:21–31.
- Batiza, R., and White, J.D.L., 2000. Submarine lavas and hyaloclastite. In Sigurdsson, H., Houghton, B.F., McNutt, S.R., Rymer, H., and Stix, J. (Eds.), *Encyclopedia of Volcanoes*: San Diego (Acad. Press), 361–381.
- Bell, J.S., and Gough, D.I., 1983. The use of borehole breakouts in the study of crustal stress. In Zoback, M.D., and Haimson, B.C. (Eds.), *Hydraulic Fracturing Stress Measurements*: Washington (Natl. Acad. Press), 201–209.
- Berggren, W.A., Kent, D.V., and Flynn, J.J., 1985. Jurassic to Paleogene, Part 2. Paleogene geochronology and chronostratigraphy. In Snelling, N.J. (Ed.), *The Chronology of the Geological Record*. Mem.—Geol. Soc. London, 10:141–195.
- Berggren, W.A., Kent, D.V., Swisher, C.C., III, and Aubry, M.-P., 1995. A revised Cenozoic geochronology and chronostratigraphy. In Berggren, W.A., Kent, D.V., Aubry, M.-P., and Hardenbol, J. (Eds.), *Geochronology, Time Scales and Global Stratigraphic Correlation*. Spec. Publ.—SEPM (Soc. Sediment. Geol.), 54:129–212.
- Berggren, W.A., and Pearson, P.N., 2005. A revised tropical to subtropical Paleogene planktonic foraminiferal zonation. *J. Foraminiferal Res.*, 35(4):279–298. doi:10.2113/35.4.279
- Biddle, J.F., Fitz-Gibbon, S., Schuster, S.C., Brenchley, J.E., and House, C.H., 2008. Metagenomic signatures of the Peru margin seafloor biosphere show a genetically distinct environment. *Proc. Natl. Acad. Sci. U. S. A.*, 105(30):10583–10588. doi:10.1073/pnas.0709942105
- Blackman, D.K., Ildefonse, B., John, B.E., Ohara, Y., Miller, D.J., MacLeod, C.J., and the Expedition 304/305 Scientists, 2006. *Proc IODP, 304/305*: College Station, TX (Integrated Ocean Drilling Program Management International, Inc.). doi:10.2204/iodp.proc.304305.2006
- Blaj, T., Backman, J., and Raffi, I., 2009. Late Eocene to Oligocene preservation history and biochronology of calcareous nannofossils from paleo-equatorial Pacific Ocean sediments. *Riv. Ital. Paleontol. Stratigr.*, 115(1):67–84.
- Blum, P., 1997. Physical properties handbook: a guide to the shipboard measurement of physical properties of deep-sea cores. *ODP Tech. Note*, 26. doi:10.2973/odp.tn.26.1997
- Bolli, H.M., and Saunders, J.B., 1985. Oligocene to Holocene low latitude planktic foraminifera. In Bolli, H.M., Saunders, J.B., and Perch-Nielsen, K. (Eds.), *Plankton Stratigraphy* (Vol. 1): *Planktic Foraminifera, Calcareous Nannofossils and Calpionellids*: Cambridge (Cambridge Univ. Press), 155–262.
- Bown, P.R. (Ed.), 1998. *Calcareous Nannofossil Biostratigraphy*: Dordrecht, The Netherlands (Kluwer Academic Publ.).
- Bralower, T.J., Fullagar, P.D., Paull, C.K., Dwyer, G.S., and Leckie, R.M., 1997. Mid-Cretaceous strontium-isotope stratigraphy of deep-sea sections. *Geol. Soc. Am. Bull.*, 109(11):1421–1442. doi:10.1130/0016-7606(1997)109<1421:MCSISO>2.3.CO;2
- Cande, S.C., and Kent, D.V., 1995. Revised calibration of the geomagnetic polarity timescale for the Late Cretaceous and Cenozoic. *J. Geophys. Res., [Solid Earth]*, 100(B4):6093–6095. doi:10.1029/94JB03098
- Carlisle, D., 1963. Pillow breccias and their aquagene tuffs, Quadra Island, British Columbia. *J. Geol.*, 71(1):48–71. doi:10.1086/626875
- Caron, M., 1985. Cretaceous planktic foraminifera. In Bolli, H.M., Saunders, J.B., and Perch-Nielsen, K. (Eds.), *Plankton Stratigraphy*: Cambridge (Cambridge Univ. Press), 17–86.
- Chaisson, W.P., and Leckie, R.M., 1993. High-resolution Neogene planktonic foraminifer biostratigraphy of Site 806, Ontong Java Plateau (western equatorial Pacific). In Berger, W.H., Kroenke, L.W., Mayer, L.A., et al., *Proc. ODP, Sci. Results*, 130: College Station, TX (Ocean Drilling Program), 137–178. doi:10.2973/odp.proc.sr.130.010.1993
- Chaisson, W.P., and Pearson, P.N., 1997. Planktonic foraminifer biostratigraphy at Site 925: middle Miocene–Pleistocene. In Shackleton, N.J., Curry, W.B., Richter, C., and Bralower, T.J. (Eds.), *Proc. ODP, Sci. Results*, 154: College Station, TX (Ocean Drilling Program), 3–31. doi:10.2973/odp.proc.sr.154.104.1997
- Channell, J.E.T., Erba, E., Nakanishi, M., and Tamaki, K., 1995. Late Jurassic–Early Cretaceous time scales and oceanic magnetic anomaly block models. In Berggren, W.A., Kent, D.V., Aubry, M.-P., and Hardenbol, J. (Eds.), *Geochronology, Time Scales, and Global Stratigraphic Correlation*. Spec. Publ.—SEPM (Soc. Sediment. Geol.), 54:51–63. <http://sp.sepmonline.org/content/sepspecpub/sepspec/1/SEC4.body.pdf>
- Clague, D.A., Paduan, J.B., and Davis, A.S., 2009. Widespread strombolian eruptions of mid-ocean ridge basalt. *J. Volcanol. Geotherm. Res.*, 180(2–4):171–188. doi:10.1016/j.jvolgeores.2008.08.007
- Cowen, J.P., Giovannoni, S.J., Kenig, F., Johnson, H.P., Butterfield, D., Rappé, M.S., Hutnak, M., and Lam, P., 2003. Fluids from aging ocean crust that support microbial life. *Science*, 299(5603):120–123. doi:10.1126/science.1075653
- Droser, M.L., and Bottjer, D.J., 1986. A semiquantitative field classification of ichnofabric. *J. Sediment. Res.*, 56(4):558–559. <http://jsedres.sepmonline.org/cgi/content/abstract/56/4/558>
- Einen, J., Thorseth, I.H., and Øvreås, L., 2008. Enumeration of *Archaea* and *Bacteria* in seafloor basalt using real-time quantitative PCR and fluorescence microscopy.

- FEMS Microbiol. Lett.*, 282(2):182–187. doi:10.1111/j.1574-6968.2008.01119.x
- Ellis, D.V., and Singer, J.M., 2007. *Well Logging for Earth Scientists*, (2nd ed.): Dordrecht, The Netherlands (Springer).
- Erba, E., Premoli Silva, I., and Watkins, D.K., 1995. Cretaceous calcareous plankton biostratigraphy of Sites 872 through 879. In Haggerty, J.A., Premoli Silva, I., Rack, F., and McNutt, M.K. (Eds.), *Proc. ODP, Sci. Results*, 144: College Station, TX (Ocean Drilling Program), 157–169. doi:10.2973/odp.proc.sr.144.071.1995
- Expedition 309/312 Scientists, 2006. Methods. In Teagle, D.A.H., Alt, J.C., Umino, S., Miyashita, S., Banerjee, N.R., Wilson, D.S., and the Expedition 309/312 Scientists. *Proc. IODP*, 309/312: Washington, DC (Integrated Ocean Drilling Program Management International, Inc.). doi:10.2204/iodp.proc.309312.102.2006
- Expedition 320T Scientists, 2009. USIO Sea Trials and Assessment of Readiness Transit (START): Ontong Java Plateau. *IODP Prel. Rept.*, 320T. doi:10.2204/iodp.pr.320T.2009
- Expedition 320/321 Scientists, 2010. Methods. In Pälke, H., Lyle, M., Nishi, H., Raffi, I., Gamage, K., Klaus, A., and the Expedition 320/321 Scientists. *Proc. IODP*, 320/321: Tokyo (Integrated Ocean Drilling Program Management International, Inc.). doi:10.2204/iodp.proc.320321.102.2010
- Expedition 324 Scientists, 2010. Methods. In Sager, W.W., Sano, T., Geldmacher, J., and the Expedition 324 Scientists. *Proc. IODP*, 324: Tokyo (Integrated Ocean Drilling Program Management International, Inc.). doi:10.2204/iodp.proc.324.102.2010
- Fisher, R.V., and Schmincke, H.-U., 1984. *Pyroclastic Rocks*: New York (Springer-Verlag).
- Fisk, M.R., Giovannoni, S.J., and Thorseth, I.H., 1998. Alteration of oceanic volcanic glass: textural evidence of microbial activity. *Science*, 281(5379):978–980. doi:10.1126/science.281.5379.978
- Gee, J.S., Tauxe, L., and Constable, C., 2008. AMSSpin: a LabVIEW program for measuring the anisotropy of magnetic susceptibility with the Kappabridge KLY-4S. *Geochem., Geophys., Geosyst.*, 9(8):Q08Y02–Q08Y21. doi:10.1029/2008GC001976
- Goldberg, D., 1997. The role of downhole measurements in marine geology and geophysics. *Rev. Geophys.*, 35(3):315–342. doi:10.1029/97RG00221
- Govindaraju, K., 1994. 1994 compilation of working values and sample description for 383 geostandards. *Geo-stand. Newsl.*, 18(1). doi:10.1111/j.1751-908X.1994.tb00502.x
- Gradstein, F.M., Agterberg, F.P., Ogg, J.G., Hardenbol, J., van Veen, P., Thierry, J., and Huang, Z., 1995. A Triassic, Jurassic and Cretaceous time scale. In Berggren, W.A., Kent, D.V., Aubry, M.-P., and Hardenbol, J. (Eds.), *Geochronology, Time Scales and Global Stratigraphic Correlation*. Spec. Publ.—SEPM (Soc. Sediment. Geol.), 54:95–126. <http://sp.seponline.org/content/sepspecpub/sepspecg/1/SEC7.body.pdf>
- Gregg, T.K.P., and Fink, J.H., 1995. Quantification of submarine lava-flow morphology through analog experiments. *Geology*, 23(1):73–76. doi:10.1130/0091-7613(1995)023<0073:QOSLFM>2.3.CO;2
- Grubbs, F.E., 1969. Procedures for detecting outlying observations in samples. *Technometrics*, 11(1):1–21. doi:10.2307/1266761
- Guilbaud, M.-N., Self, S., Thordarson, T., and Blake, S., 2005. Morphology, surface structures, and emplacement of lavas produced by Laki, A.D. 1783–1784. In Manga, M., and Ventura, G. (Eds.), *Kinematics and Dynamics of Lava Flows*. Spec. Pap.—Geol. Soc. Am., 396:81–102.
- Hancock, H.J.L., Chaproniere, G.C., Dickens, G.R., and Henderson, R.A., 2002. Early Palaeogene planktic foraminiferal and carbon isotope stratigraphy, Hole 762C, Exmouth Plateau, northwest Australian margin. *J. Micropalaeontol.*, 21(1):29–42. doi:10.1144/jm.21.1.29
- Hext, G.R., 1963. The estimation of second-order tensors, with related tests and designs. *Biometrika*, 50(3–4):353–373. doi:10.1093/biomet/50.3-4.353
- Inagaki, F., Nunoura, T., Nakagawa, S., Teske, A., Lever, M., Lauer, A., Suzuki, M., Takai, K., Delwiche, M., Colwell, F.S., Nealson, K.H., Horikoshi, K., D’Hondt, S., and Jørgensen, B.B., 2006. Biogeographical distribution and diversity of microbes in methane hydrate-bearing deep marine sediments on the Pacific Ocean margin. *Proc. Natl. Acad. Sci. U. S. A.*, 103(8):2815–2820. doi:10.1073/pnas.0511033103
- Ito, H., Nogi, Y., and Larson, R.L., 1995. Magnetic reversal stratigraphy of Jurassic oceanic crust from Hole 801C downhole magnetometer measurements. In Haggerty, J.A., Premoli Silva, I., Rack, F., and McNutt, M.K. (Eds.), *Proc. ODP, Sci. Results*, 144: College Station, TX (Ocean Drilling Program), 641–647. doi:10.2973/odp.proc.sr.144.024.1995
- Jarrard, R.D., and Kerneklian, M.J., 2007. Data report: physical properties of the upper oceanic crust of ODP Site 1256: multisensor track and moisture and density measurements. In Teagle, D.A.H., Wilson, D.S., Acton, G.D., and Vanko, D.A. (Eds.), *Proc. ODP, Sci. Results*, 206: College Station, TX (Ocean Drilling Program), 1–11. doi:10.2973/odp.proc.sr.206.011.2007
- Jovane, L., Florindo, F., Coccioni, R., Dinarès-Turell, J., Marsili, A., Monechi, S., Roberts, A.P., and Sprovieri, M., 2007. The middle Eocene climatic optimum event in the Contessa Highway section, Umbrian Apennines, Italy. *Geol. Soc. Am. Bull.*, 119(3–4):413–427. doi:10.1130/B25917.1
- Kennett, J.P., and Srinivasan, M.S., 1983. *Neogene Planktonic Foraminifera: A Phylogenetic Atlas*: Stroudsburg, PA (Hutchinson Ross).
- Kirschvink, J.L., 1980. The least-squares line and plane and the analysis of palaeomagnetic data. *Geophys. J. R. Astron. Soc.*, 62(3):699–718. doi:10.1111/j.1365-246X.1980.tb02601.x
- Kokelaar, B.P., 1982. Fluidization of wet sediments during the emplacement and cooling of various igneous bodies. *J. Geol. Soc. (London, U. K.)*, 139(1):21–33. doi:10.1144/gsjgs.139.1.0021
- Kono, M., 1980. Statistics of paleomagnetic inclination data. *J. Geophys. Res., [Solid Earth]*, 85(B7):3878–3882. doi:10.1029/JB085iB07p03878

- Leckie, R.M., Farnham, C., and Schmidt, M.G., 1993. Oligocene planktonic foraminifer biostratigraphy of Hole 803D (Ontong Java Plateau) and Hole 628A (Little Bahama Bank), and comparison with the southern high latitudes. *In* Berger, W.H., Kroenke, L.W., Mayer, L.A., et al., *Proc. ODP, Sci. Results*, 130: College Station, TX (Ocean Drilling Program), 113–136. doi:10.2973/odp.proc.sr.130.012.1993
- Lever, M.A., Alperin, M., Engelen, B., Inagaki, F., Nakagawa, S., Steinsbu, B.O., Teske, A., and IODP Expedition 301 Scientists, 2006. Trends in basalt and sediment core contamination during IODP Expedition 301. *Geomicrobiol. J.*, 23(7):517–530. doi:10.1080/01490450600897245
- Loeblich, A.R., Jr., and Tappan, H., 1988. *Foraminiferal Genera and Their Classification*: New York (Van Nostrand Reinhold).
- Lourens, L.J., Hilgen, F.J., Laskar, J., Shackleton, N.J., and Wilson, D., 2004. The Neogene period. *In* Gradstein, F.M., Ogg, J., et al. (Eds.), *A Geologic Time Scale 2004*: Cambridge (Cambridge Univ. Press), 409–440.
- Lovell, M.A., Harvey, P.K., Brewer, T.S., Williams, C., Jackson, P.D., and Williamson, G., 1998. Application of FMS images in the Ocean Drilling Program: an overview. *In* Cramp, A., MacLeod, C.J., Lee, S.V., and Jones, E.J.W. (Eds.), *Geological Evolution of Ocean Basins: Results from the Ocean Drilling Program*. Geol. Soc. Spec. Publ., 131(1):287–303. doi:10.1144/GSL.SP.1998.131.01.18
- Luthi, S.M., 1990. Sedimentary structures of clastic rocks identified from electrical borehole images. *In* Hurst, A., Lovell, M.A., and Morton, A.C. (Eds.), *Geological Applications of Wireline Logs*. Geol. Soc. Spec. Publ., 48(1):3–10. doi:10.1144/GSL.SP.1990.048.01.02
- Lyle, M., Wilson, P.A., Janecek, T.R., et al., 2002. *Proc. ODP, Init. Repts.*, 199: College Station, TX (Ocean Drilling Program). doi:10.2973/odp.proc.ir.199.2002
- MacKenzie, W.S., Donaldson, C.H., and Guilford, C., 1982. *Atlas of Igneous Rocks and Their Textures*: Essex, England (Longman Group UK Limited).
- Mahoney, J.J., Fitton, J.G., Wallace, P.J., et al., 2001. *Proc. ODP, Init. Repts.*, 192: College Station, TX (Ocean Drilling Program). doi:10.2973/odp.proc.ir.192.2001
- Mason O.U., Di Meo-Savoie, C.A., Van Nostrand, J.D., Zhou, J., Fisk, M.R., and Giovannoni, S.J., 2009. Prokaryotic diversity, distribution, and insights into their role in biogeochemical cycling in marine basalts. *ISME J.*, 3:231–242. doi:10.1038/ismej.2008.92
- Mason, O.U., Nakagawa, T., Rosner, M., Van Nostrand, J.D., Zhou, J., Maruyama, A., Fisk, M.R., and Giovannoni, S.J., 2010. First investigation of the microbiology of the deepest layer of ocean crust. *PLoS One*, 5(11):e15399. doi:10.1371/journal.pone.0015399
- Mazzullo, J.M., Meyer, A., and Kidd, R.B., 1988. New sediment classification scheme for the Ocean Drilling Program. *In* Mazzullo, J.M., and Graham, A.G. (Eds.), *Handbook for shipboard sedimentologists*. ODP Tech. Note, 8:45–67. doi:10.2973/odp.tn.8.1988
- McFadden, P.L., and Reid, A.B., 1982. Analysis of paleomagnetic inclination data. *Geophys. J. R. Astron. Soc.*, 69:307–319.
- Moore, D.M., and Reynolds, R.C., Jr., 1997. *X-Ray Diffraction and the Identification and Analysis of Clay Minerals* (2nd ed.): Oxford (Oxford Univ. Press).
- Munsell Color Company, Inc., 1994. *Munsell Soil Color Chart* (Revised ed.): Newburgh, MD (Munsell Color).
- Munsell Color Company, Inc., 2000. *Munsell Soil Color Chart*: New York (Gretag-Macbeth).
- Murray, R.W., Miller, D.J., and Kryc, K.A., 2000. Analysis of major and trace elements in rocks, sediments, and interstitial waters by inductively coupled plasma–atomic emission spectrometry (ICP–AES). *ODP Tech. Note*, 29. doi:10.2973/odp.tn.29.2000
- Nederbragt, A.J., 1991. Late Cretaceous biostratigraphy and development of Heterohelicidae (planktic foraminifera). *Micropaleontology*, 37(4):329–372. doi:10.2307/1485910
- Okada, H., and Bukry, D., 1980. Supplementary modification and introduction of code numbers to the low-latitude coccolith biostratigraphic zonation (Bukry, 1973; 1975). *Mar. Micropaleontol.*, 5:321–325. doi:10.1016/0377-8398(80)90016-X
- Olsson, R.K., Hemleben, C., Berggren, W.A., and Huber, B.T. (Eds.), 1999. *Atlas of Paleocene Planktonic Foraminifera*: Washington, DC (Smithsonian Institution Press). <http://hdl.handle.net/10088/2001>
- Paillet, F.L., and Kim, K., 1987. Character and distribution of borehole breakouts and their relationship to in situ stresses in deep Columbia River basalts. *J. Geophys. Res., [Solid Earth]*, 92(B7):6223–6234. doi:10.1029/JB092iB07p06223
- Pälike, H., Norris, R.D., Herrle, J.O., Wilson, P.A., Coxall, H.K., Lear, C.H., Shackleton, N.J., Tripati, A.K., and Wade, B.S., 2006. The heartbeat of the Oligocene climate system. *Science*, 314(5807):1894–1898. doi:10.1126/science.1133822
- Parker, R.L., and Gee, J.S., 2002. Calibration of the pass-through magnetometer—II. Application. *Geophys. J. Int.*, 150:140–152. doi:10.1046/j.1365-246X.2002.01692.x
- Parkes, R.J., Cragg, B.A., Bale, S.J., Getliff, J.M., Goodman, K., Rochelle, P.A., Fry, J.C., Weightman, A.J., and Harvey, S.M., 1994. Deep bacterial biosphere in Pacific Ocean sediments. *Nature (London, U. K.)*, 371(6496):410–413. doi:10.1038/371410a0
- Passchier, C.W., and Trouw, R.A.J., 1996. *Microtectonics*: Berlin (Springer-Verlag).
- Pearson, P.N., 1995. Planktonic foraminifer biostratigraphy and the development of pelagic caps on guyots in the Marshall Islands group. *In* Haggerty, J.A., Premoli Silva, I., Rack, F., and McNutt, M.K. (Eds.), *Proc. ODP, Sci. Results*, 144: College Station, TX (Ocean Drilling Program), 21–59. doi:10.2973/odp.proc.sr.144.013.1995
- Pearson, P.N., and Chaisson, W.P., 1997. Late Paleocene to middle Miocene planktonic foraminifer biostratigraphy of the Ceara Rise. *In* Shackleton, N.J., Curry, W.B., Richter, C., and Bralower, T.J. (Eds.), *Proc. ODP, Sci. Results*, 154: College Station, TX (Ocean Drilling Program), 33–68. doi:10.2973/odp.proc.sr.154.106.1997
- Pearson, P.N., Olsson, R.K., Huber, B.T., Hemleben, C., and Berggren, W.A. (Eds.), 2006. *Atlas of Eocene Planktonic*

- Foraminifera*. Spec. Publ.—Cushman Found. Foraminiferal Res., 41.
- Perch-Nielsen, K., 1985. Cenozoic calcareous nannofossils. In Bolli, H.M., Saunders, J.B., and Perch-Nielsen, K. (Eds.), *Plankton Stratigraphy*: Cambridge (Cambridge Univ. Press), 427–554.
- Petrizzo, M.R., 2000. Upper Turonian–lower Campanian planktonic foraminifera from southern mid–high latitudes (Exmouth Plateau, NW Australia): biostratigraphy and taxonomic notes. *Cretaceous Res.*, 21(4):479–505. doi:10.1006/cres.2000.0218
- Premoli Silva, I., and Sliter, W.V., 1999. Cretaceous paleoceanography: evidence from planktonic foraminiferal evolution. In Barrera, E., and Johnson, C.C. (Eds.), *The Evolution of Cretaceous Ocean-Climatic System*. Spec. Pap.—Geol. Soc. Am., 332:301–328.
- Raffi, I., Backman, J., Fornaciari, E., Pälike, H., Rio, D., Lourens, L., and Hilgen, F., 2006. A review of calcareous nannofossil astrobiochronology encompassing the past 25 million years. *Quat. Sci. Rev.*, 25(23–24):3113–3137. doi:10.1016/j.quascirev.2006.07.007
- Ramsay, J.G., and Huber, M.I., 1987. *The Techniques of Modern Structural Geology* (Vol. 2): *Folds and Fractures*: New York (Acad. Press).
- Rider, M.H., 1996. *The Geological Interpretation of Well Logs* (2nd ed.): Caithness (Whittles Publ.).
- Robaszynski, F., and Caron, M., 1979. Atlas de foraminifères planctoniques du Crétacé moyen (mer Boréale et Téthys) (Vols. 1 and 2). *Cah. Micropaleontol.*
- Robaszynski, F., and Caron, M., 1995. Foraminifères planctoniques du Crétacé: commentaire de la zonation Europe-Méditerranée. *Bull. Soc. Geol. Fr.*, 166:681–692.
- Robaszynski, F., Caron, M., Gonzales-Donoso, J.-M., Wonders, A.A.H., and the European Working Group on Planktonic Foraminifera, 1984. Atlas of Late Cretaceous globotruncanids. *Rev. Micropaleontol.*, 26:145–305.
- Robinson, S., Mrozewski, S., Hussein, T., Masterson, W., Meissner, E., Williams, T., Keogh, W., Myers, G., Bartington, G., and Goldberg, D., 2008. A new borehole magnetic susceptibility tool for high-resolution formation evaluation. In *SPWLA 49th Annual Logging Symposium: Abstracts*. Petrophys. Houston, 49(2):196–197.
- Rothwell, R.G., 1989. *Minerals and Mineraloids in Marine Sediments: An Optical Identification Guide*: London (Elsevier).
- Roussel, E.G., Bonavita, M.-A.C., Querellou, J., Cragg, B.A., Webster, G., Prieur, D., and Parkes, R.J., 2008. Extending the seafloor biosphere. *Science*, 320(5879):1046. doi:10.1126/science.1154545
- Rouxel, O., Ono, S., Alt, J., Rumble, D., and Ludden, J., 2008. Sulfur isotope evidence for microbial sulfate reduction in altered oceanic basalts at ODP Site 801. *Earth Planet. Sci. Lett.*, 268(1–2):110–123. doi:10.1016/j.epsl.2008.01.010
- Sager, W.W., Sano, T., Geldmacher, J., and the Expedition 324 Scientists, 2010. *Proc. IODP*, 324: Tokyo (Integrated Ocean Drilling Program Management International, Inc.). doi:10.2204/iodp.proc.324.2010
- Salimullah, A.R.M., and Stow, D.A.V., 1992. Application of FMS images in poorly recovered coring intervals: examples from ODP Leg 129. In Hurst, A., Griffiths, C.M., and Worthington, P.F. (Eds.), *Geological Application of Wireline Logs II*. Geol. Soc. Spec. Publ., 65(1):71–86. doi:10.1144/GSL.SP.1992.065.01.06
- Santelli, C.M., Edgcomb, V.P., Bach, W., and Edwards, K.J., 2009. The diversity and abundance of bacteria inhabiting seafloor lavas positively correlate with rock alteration. *Environ. Microbiol.*, 11(1):86–98. doi:10.1111/j.1462-2920.2008.01743.x
- Santelli, C.M., Orcutt, B.N., Banning, E., Bach, W., Moyer, C.L., Sogin, M.L., Staudigel, H., and Edwards, K.J., 2008. Abundance and diversity of microbial life in ocean crust. *Nature (London, U. K.)*, 453(7195):653–656. doi:10.1038/nature06899
- Schlumberger, 1989. *Log Interpretation Principles/Applications*: Houston (Schlumberger Educ. Serv.), SMP-7017.
- Schlumberger, 1994. *IPL Integrated Porosity Lithology*: Houston (Schlumberger Wireline Testing), SMP-9270.
- Serra, O., 1984. *Fundamentals of Well-Log Interpretation* (Vol. 1): *The Acquisition of Logging Data*: Amsterdam (Elsevier).
- Serra, O., 1986. *Fundamentals of Well-Log Interpretation* (Vol. 2): *The Interpretation of Logging Data*. Amsterdam (Elsevier).
- Serra, O., 1989. *Formation MicroScanner Image Interpretation*: Houston (Schlumberger Educ. Serv.), SMP-7028.
- Shackleton, N.J., Berger, A., and Peltier, W.A., 1990. An alternative astronomical calibration of the lower Pleistocene timescale based on ODP Site 677. *Trans. R. Soc. Edinburgh: Earth Sci.*, 81:251–261.
- Shackleton, N.J., Crowhurst, S., Hagemberg, T., Pisias, N.G., and Schneider, D.A., 1995. A new late Neogene time scale: application to Leg 138 sites. In Pisias, N.G., Mayer, L.A., Janecek, T.R., Palmer-Julson, A., and van Andel, T.H. (Eds.), *Proc. ODP, Sci. Results*, 138: College Station, TX (Ocean Drilling Program), 73–101. doi:10.2973/odp.proc.sr.138.106.1995
- Shackleton, N.J., Crowhurst, S.J., Weedon, G.P., and Laskar, J., 1999. Astronomical calibration of Oligocene–Miocene time. In Shackleton N.J., McCave, I.N., and Graham, P.W. (Eds.), *Astronomical (Milankovitch) Calibration of the Geological Time-Scale*. Philos. Trans. R. Soc., Ser. A., 357(1757):1907–1929. doi:10.1098/rsta.1999.0407
- Shepard, F.P., and Young, R., 1961. Distinguishing between beach and dune sands. *J. Sediment. Res.*, 31(2):196–214. doi:10.1306/74D70B37-2B21-11D7-8648000102C1865D
- Shipboard Scientific Party, 1997. Explanatory notes. In Kimura, G., Silver, E., Blum, P., et al., *Proc. ODP, Init. Repts.*, 170: College Station, TX (Ocean Drilling Program), 19–42. doi:10.2973/odp.proc.ir.170.102.1997
- Shipboard Scientific Party, 2002. Explanatory notes. In Tarduno, J.A., Duncan, R.A., Scholl, D.W., et al., *Proc. ODP, Init. Repts.*, 197: College Station, TX (Ocean Drilling Program), 1–89. doi:10.2973/odp.proc.ir.197.102.2002
- Shipboard Scientific Party, 2003. Explanatory notes. In Wilson, D.S., Teagle, D.A.H., Acton, G.D., *Proc. ODP, Init.*

- Repts., 206: College Station, TX (Ocean Drilling Program), 1–94. doi:10.2973/odp.proc.ir.206.102.2003
- Shipboard Scientific Party, 2004. Leg 207 summary. In Erbacher, J., Mosher, D.C., Malone, M.J., et al., *Proc. ODP, Init. Repts.*, 207: College Station, TX (Ocean Drilling Program), 1–89. doi:10.2973/odp.proc.ir.207.101.2004
- Sissingh, W., 1977. Biostratigraphy of Cretaceous calcareous nannoplankton. *Geol. Mijnbouw*, 56:37–65.
- Skilling, I.P., White, J.D.L., and McPhie, J., 2002. Peperite: a review of magma–sediment mingling. *J. Volcanol. Geotherm. Res.*, 114(1–2):1–17. doi:10.1016/S0377-0273(01)00278-5
- Sliter, W.V., 1989. Biostratigraphic zonation for Cretaceous planktonic foraminifers examined in thin section. *J. Foraminiferal Res.*, 19(1):1–19. doi:10.2113/gsjfr.19.1.1
- Smith, D.C., Spivack, A.J., Fisk, M.R., Haveman, S.A., Staudigel, H., and the Leg 185 Shipboard Scientific Party, 2000. Methods for quantifying potential microbial contamination during deep ocean coring. *ODP Tech. Note*, 28. doi:10.2973/odp.tn.28.2000
- Spezzaferri, S., 1994. Planktonic foraminiferal biostratigraphy and taxonomy of the Oligocene and lower Miocene in the oceanic record: an overview. *Palaeontographica Ital.*, 81:1–187.
- Spezzaferri, S., and Premoli Silva, I., 1991. Oligocene planktonic foraminiferal biostratigraphy and paleoclimatic interpretation from Hole 538A, DSDP Leg 77, Gulf of Mexico. *Palaeogeogr., Palaeoclimatol., Palaeoecol.*, 83(1–3):217–263. doi:10.1016/0031-0182(91)90080-B
- Srinivasan, M.S., and Sinha, D.K., 1992. Late Neogene planktonic foraminiferal events of the southwest Pacific and Indian Ocean: a comparison. In Tsuchi, R., and Ingle, J.C., Jr. (Eds.), *Pacific Neogene: Environment, Evolution and Events*: Tokyo (Univ. Tokyo Press), 203–220.
- Staudigel, H., and Schmincke, H.-U., 1984. The Pliocene seamount series of La Palma/Canary Islands. *J. Geophys. Res., [Solid Earth]*, 89(B13):11195–11215. doi:10.1029/JB089iB13p11195
- Stevelling, E., Spitzer, K., and Leven, M., 1991. Vertical gradient of horizontal geomagnetic variations—first results with the new Goettingen borehole magnetometer in the KTB-VB pilot hole. *Sci. Drill.*, 2:180–187.
- Stevelling, E., Stoll, J.B., and Leven, M., 2003. Quasi-continuous depth profiles of rock magnetization from magnetic logs in the HSDP-2 borehole, Island of Hawaii. *Geochem., Geophys., Geosyst.*, 4(4):8708–8734. doi:10.1029/2002GC000330
- Taylor, B., Huchon, P., Klaus, A., et al., 2000. *Proc. ODP, Init. Repts.*, 180: College Station, TX (Ocean Drilling Program). doi:10.2973/odp.proc.ir.180.2000
- Thordarson, T., and Self, S., 1998. The Roza Member, Columbia River Basalt Group: a gigantic pahoehoe lava flow field formed by endogenous processes. *J. Geophys. Res., [Solid Earth]*, 103(B11):27411–27445. doi:10.1029/98JB01355
- Toumarkine, M., and Luterbacher, H., 1985. Paleocene and Eocene planktic foraminifera. In Bolli, H.M., Saunders, J.B., and Perch-Nielsen, K. (Eds.), *Plankton Stratigraphy*: Cambridge (Cambridge Univ. Press), 87–154.
- Turco, E., Bambini, A.M., Foresi, L., Iaccarino, S., Lirer, F., Mazzei, R., and Salvatorini, G., 2002. Middle Miocene high-resolution calcareous plankton biostratigraphy at Site 926 (Leg 154, equatorial Atlantic Ocean): palaeoecological and palaeobiogeographical implications. *Geobios*, 35(1):257–276. doi:10.1016/S0016-6995(02)00064-5
- Twiss, R.J., and Moores, E.M., 1992. *Structural Geology*: New York (Freeman).
- Vacquier, V., 1985. The measurement of thermal conductivity of solids with a transient linear heat source on the plane surface of a poorly conducting body. *Earth Planet. Sci. Lett.*, 74(2–3):275–279. doi:10.1016/0012-821X(85)90027-5
- van Andel, T.H., and Ballard, R.D., 1979. The Galapagos Rift at 86°W, 2. Volcanism, structure, and evolution of the rift valley. *J. Geophys. Res., [Solid Earth]*, 84(B10):5379–5606. doi:10.1029/JB084iB10p05390
- Villa, G., Fioroni, C., Pea, L., Bohaty, S., and Persico, D., 2008. Middle Eocene–late Oligocene climate variability: calcareous nannofossil response at Kerguelen Plateau, Site 748. *Mar. Micropaleontol.*, 69(2):173–192. doi:10.1016/j.marmicro.2008.07.006
- Wade, B.S., 2004. Planktonic foraminiferal biostratigraphy and mechanisms in the extinction of *Morozovella* in the late middle Eocene. *Mar. Micropaleontol.*, 51(1–2):23–38. doi:10.1016/j.marmicro.2003.09.001
- Wade, B.S., Berggren, W.A., and Olsson, R.K., 2007. The biostratigraphy and paleobiology of Oligocene planktonic foraminifera from the equatorial Pacific Ocean (ODP Site 1218). *Mar. Micropaleontol.*, 62(3):167–179. doi:10.1016/j.marmicro.2006.08.005
- Walker, G.P.L., 1992. Morphometric study of pillow-size spectrum among pillow lavas. *Bull. Volcanol.*, 54(6):459–474. doi:10.1007/BF00301392
- Wentworth, C.K., 1922. A scale of grade and class terms for clastic sediments. *J. Geol.*, 30(5):377–392. doi:10.1086/622910
- Wilmoth, R.A., and Walker, G.P.L., 1993. P-type and S-type pahoehoe: a study of vesicle distribution patterns in Hawaiian lava flows. *J. Volcanol. Geotherm. Res.*, 55(1–2):129–142. doi:10.1016/0377-0273(93)90094-8

Publication: 11 February 2012
MS 330-102

Figure F1. Example of a sedimentary VCD standard graphic report, Expedition 330.

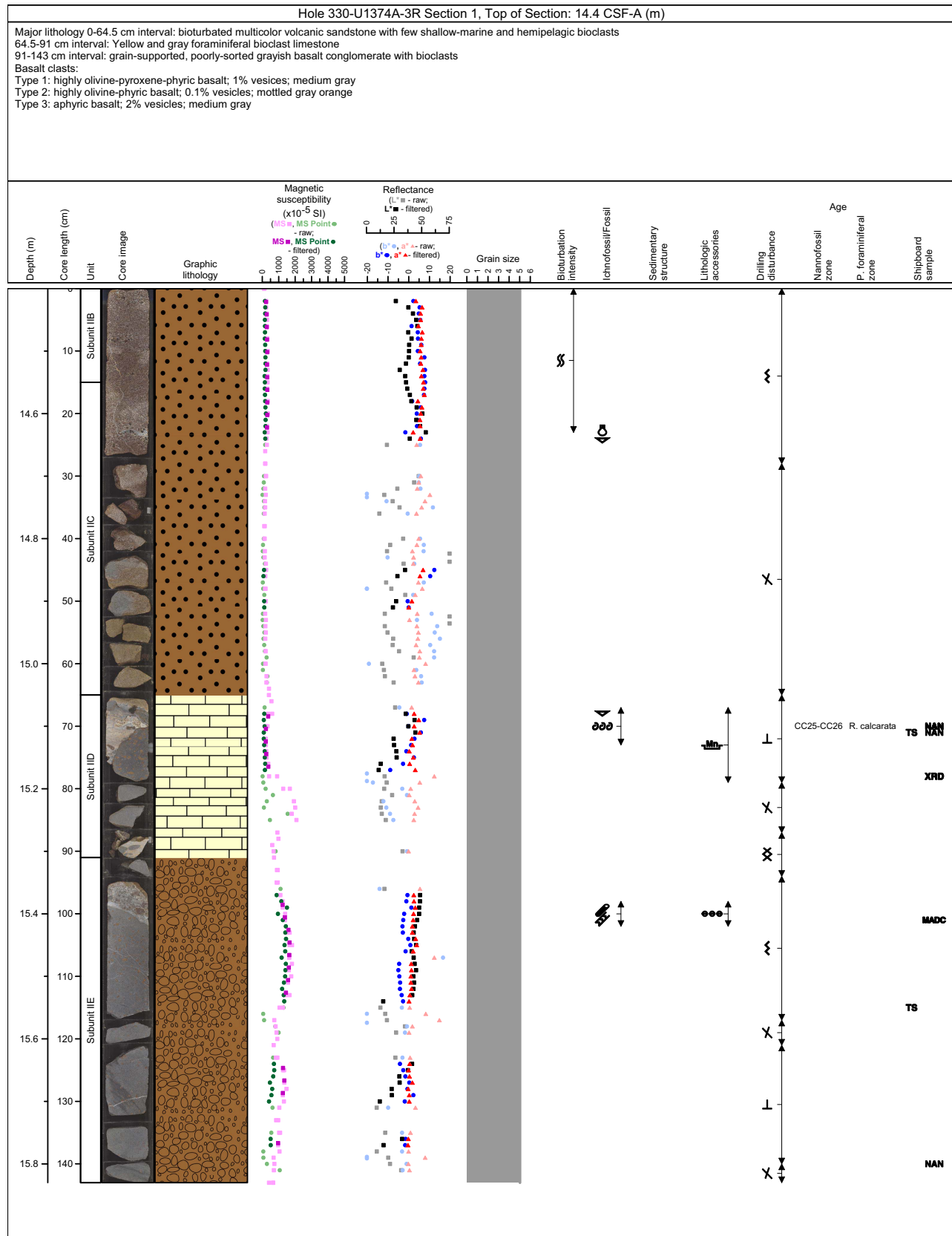








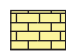

Figure F2. Symbols and nomenclature used in sedimentary VCD standard graphic reports, Expedition 330.

Lithology


Volcaniclastic and igneous rocks

 Volcanic sand/sandstone	 Ash/Tuff
 Volcanic breccia	 Hyaloclastite
 Volcanic conglomerate/Pumiceous gravel	 Basalt/Peperite







Pelagic rocks

 Limestone
 Calcareous ooze









Neritic rocks

 Boundstone

Contact, strata, and physical structures

 Loadcast	 Cross laminae/Cross-bedding	 Laminated/Bedded/Layered	 Grading/Fining upward	 Coarsening upward
 Erosional				










Lithologic accessories

 Pumice	 Concretion/Aggregate	 Coated grain/Biogenic encrustation	 Intraclast/Sediment clast	 Volcanic ash/Glass fragment
 Geopetal	 Basalt clast	 Manganese encrustation		











Degree of bioturbation

 Minor	 Moderate	 Intense
---	--	---

Fossils

 Bivalve	 Shell fragment	 Bryozoan	 Gastropod	 Foraminifer (planktonic/benthic)
 Annelid	 Bioclast	 Algae	 Echinoderm	

Drilling disturbance

 Soupy	 Slightly disturbed	 Slightly fractured	 Flow-in
 Drilling breccia	 Moderately disturbed	 Moderately fractured	 Fall-in
	 Highly disturbed	 Highly fractured	

Shipboard sampling

SS Smear slide	SED Sediment	NAN Nannofossils	ICP ICP-AES analysis	XRD X-ray diffraction
TS Thin section	PMG Paleomagnetism	PAL Paleontology	MBI Microbiology	CHNS Carbon-hydrogen-nitrogen-sulfur
Ph Close-up photograph	PP Physical properties	FOR Planktonic foraminifers	MADC Moisture and density Method C	XRF X-ray fluorescence

Grain size

1 Clay	2 Silt	3 Very fine to fine sand	4 Medium to very coarse sand	5 Gravel/Pebble/Cobble	6 Boulder
--------	--------	--------------------------	------------------------------	------------------------	-----------

Figure F3. Sediment classification scheme used during Expedition 330 (after Mazzullo et al., 1988). See “[Sedimentology](#)” for further explanation.

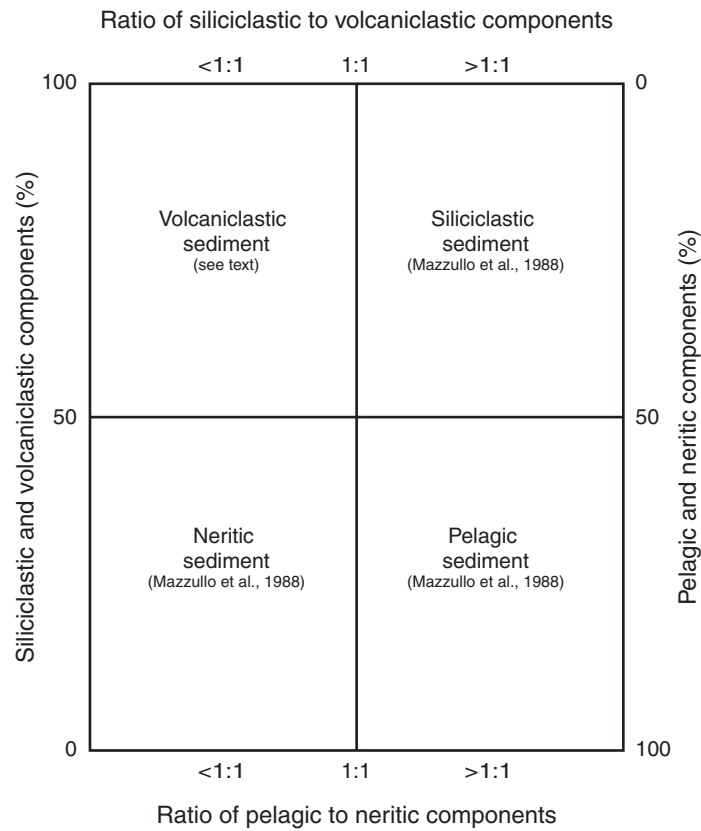


Figure F4. Timescale used for Expedition 330, including calcareous nannofossil and planktonic foraminifer zones and datums for 0–85 Ma. B = base, T = top, Tc = top common, Bc = base common, Br = base reentrance, X = abundance crossover (nannofossils) or coiling change (planktonic foraminifers). L = late, M = middle, E = early. Underlined species are foraminifers. A. 0–10 Ma. (Continued on next four pages.)

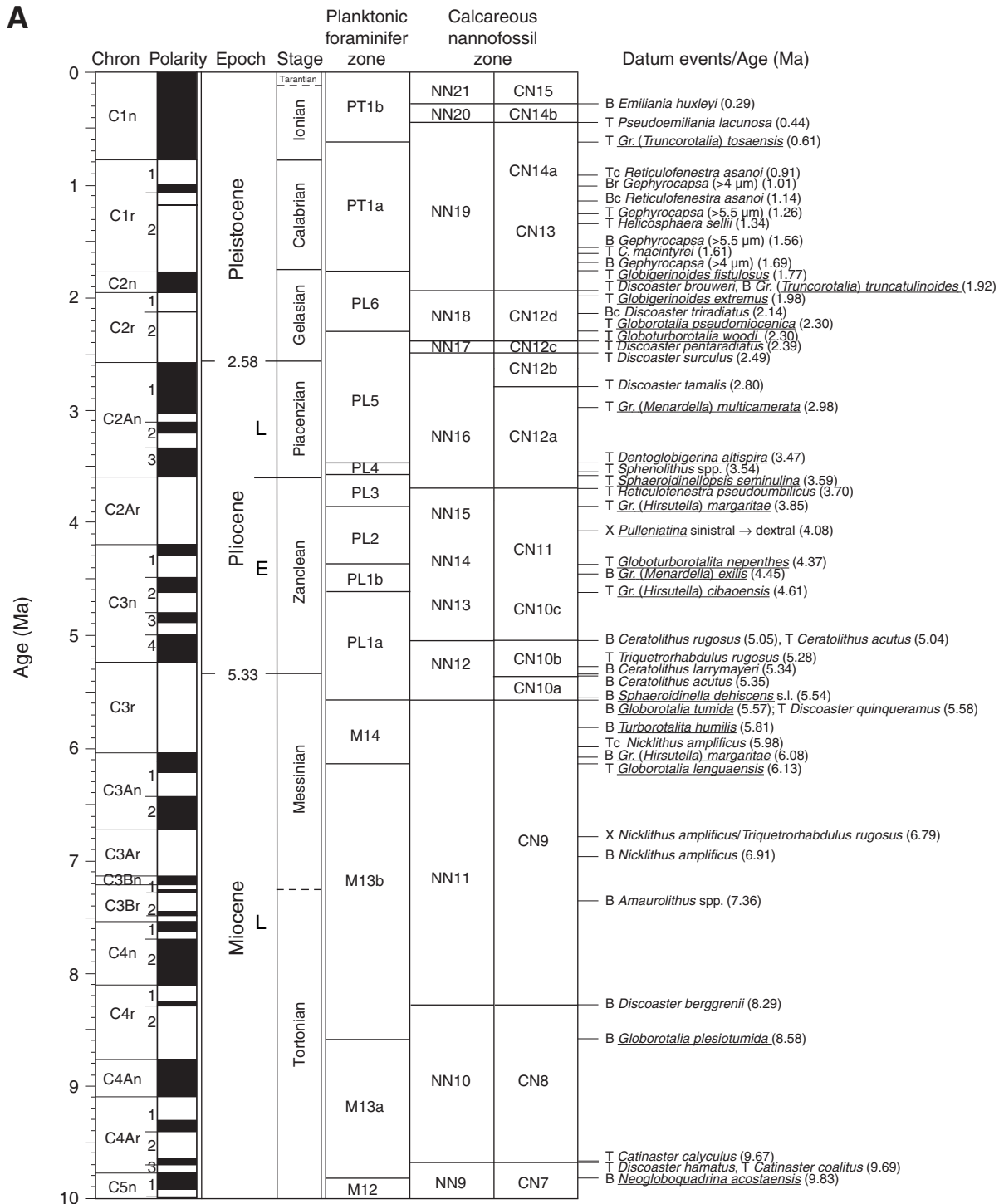


Figure F4 (continued). B. 10–20 Ma. (Continued on next page.)

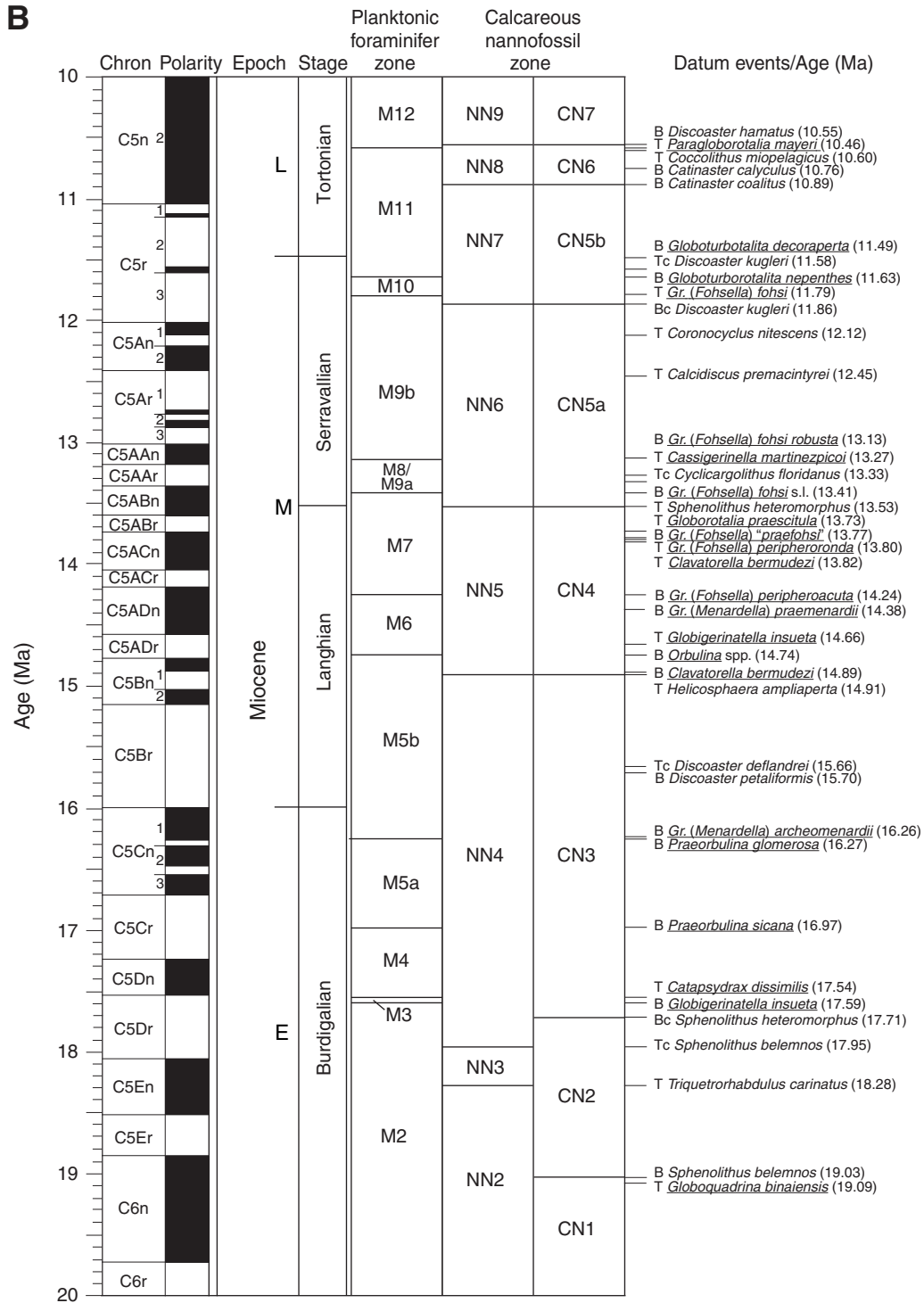


Figure F4 (continued). C. 20–40 Ma. (Continued on next page.)

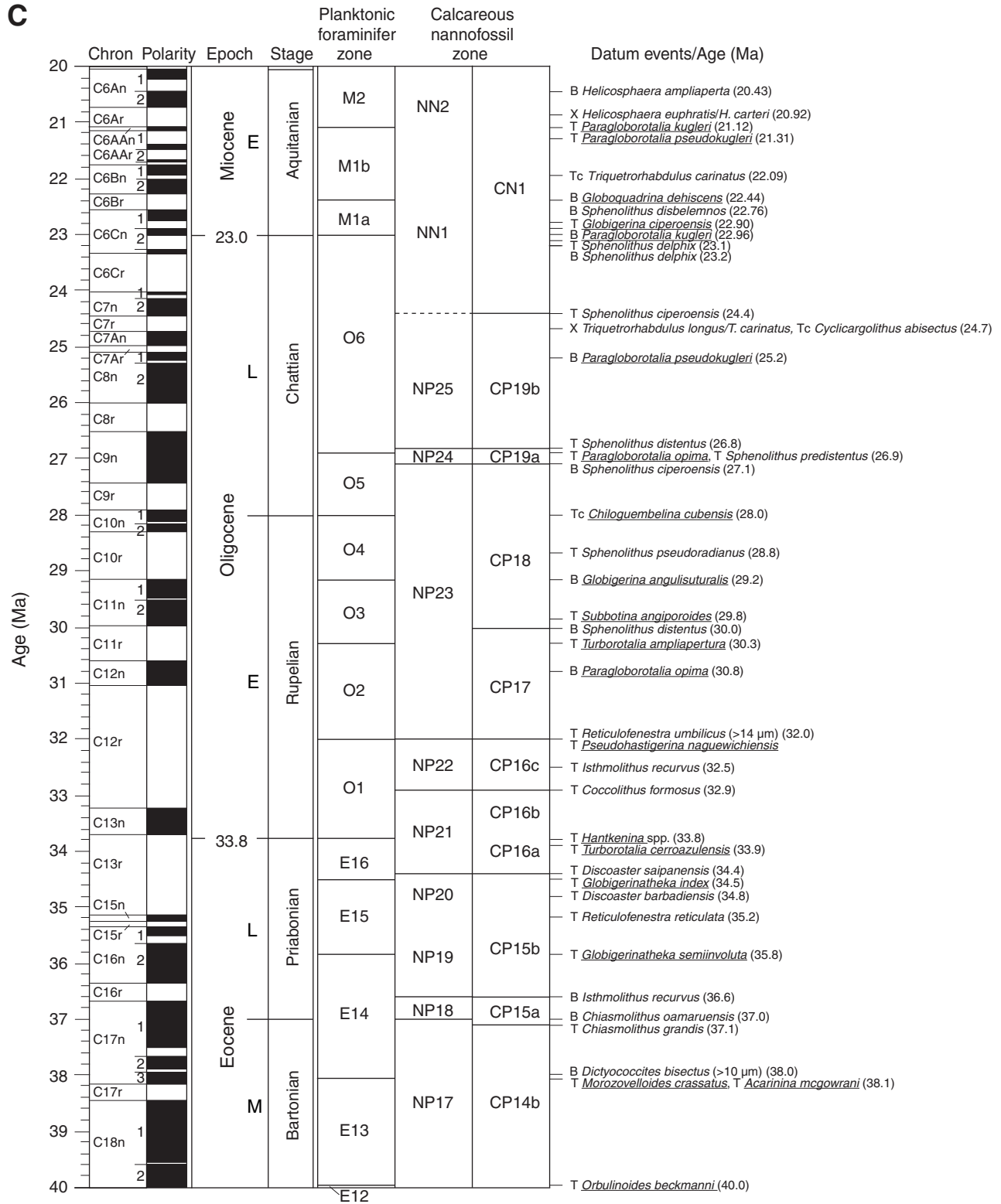


Figure F4 (continued). D. 40–60 Ma. (Continued on next page.)

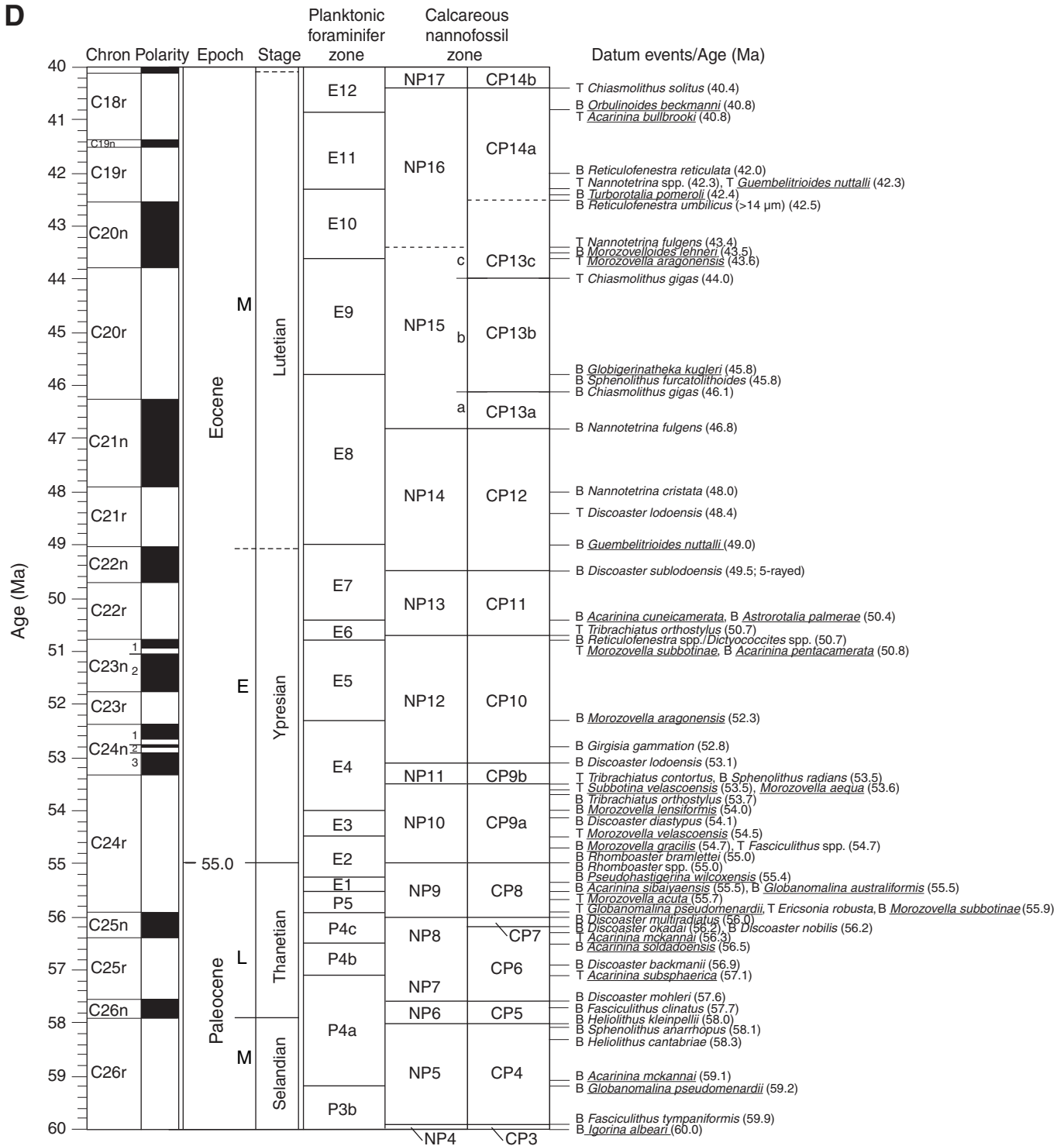


Figure F4 (continued). E. 60–85 Ma.

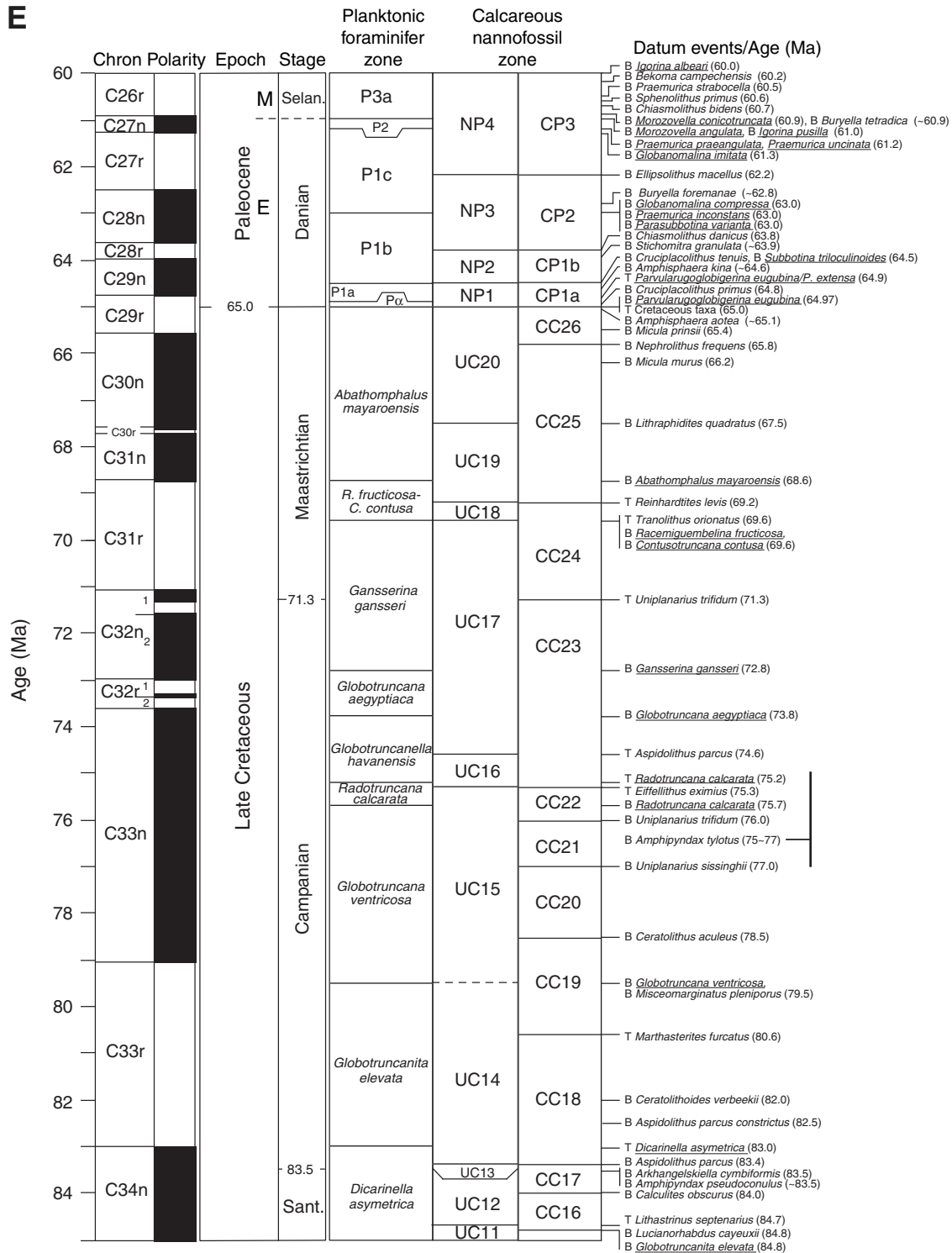


Figure F5. Modal shape and sphericity of vesicle populations, adapted from the Wentworth (1922) scheme for describing grain shape in sedimentary rocks.

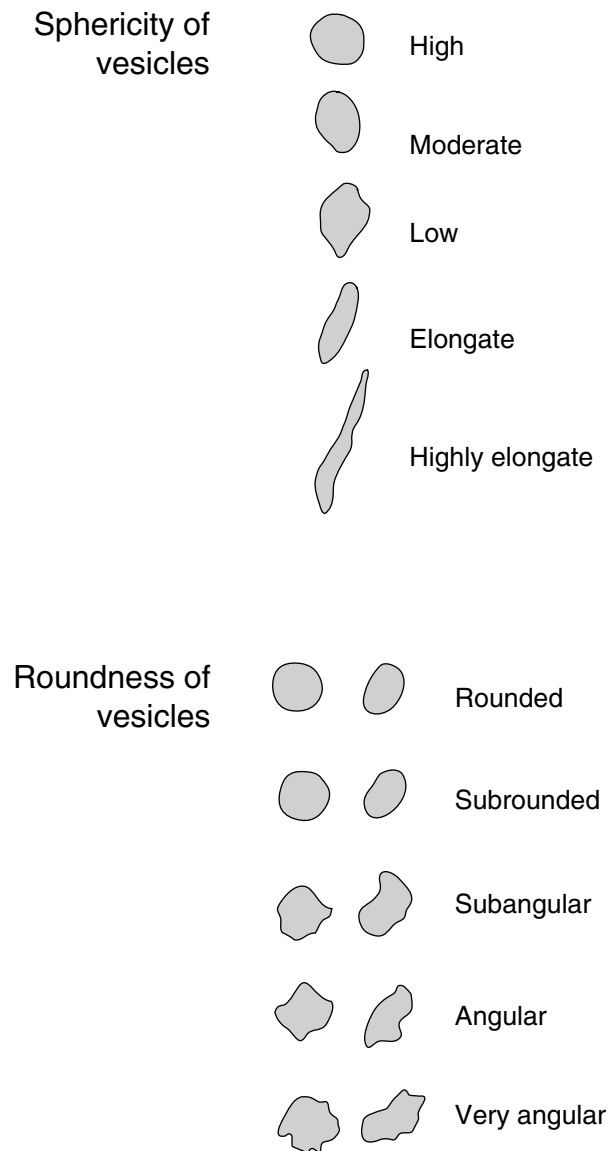


Figure F6. Example of igneous VCD standard graphic report, Expedition 330.

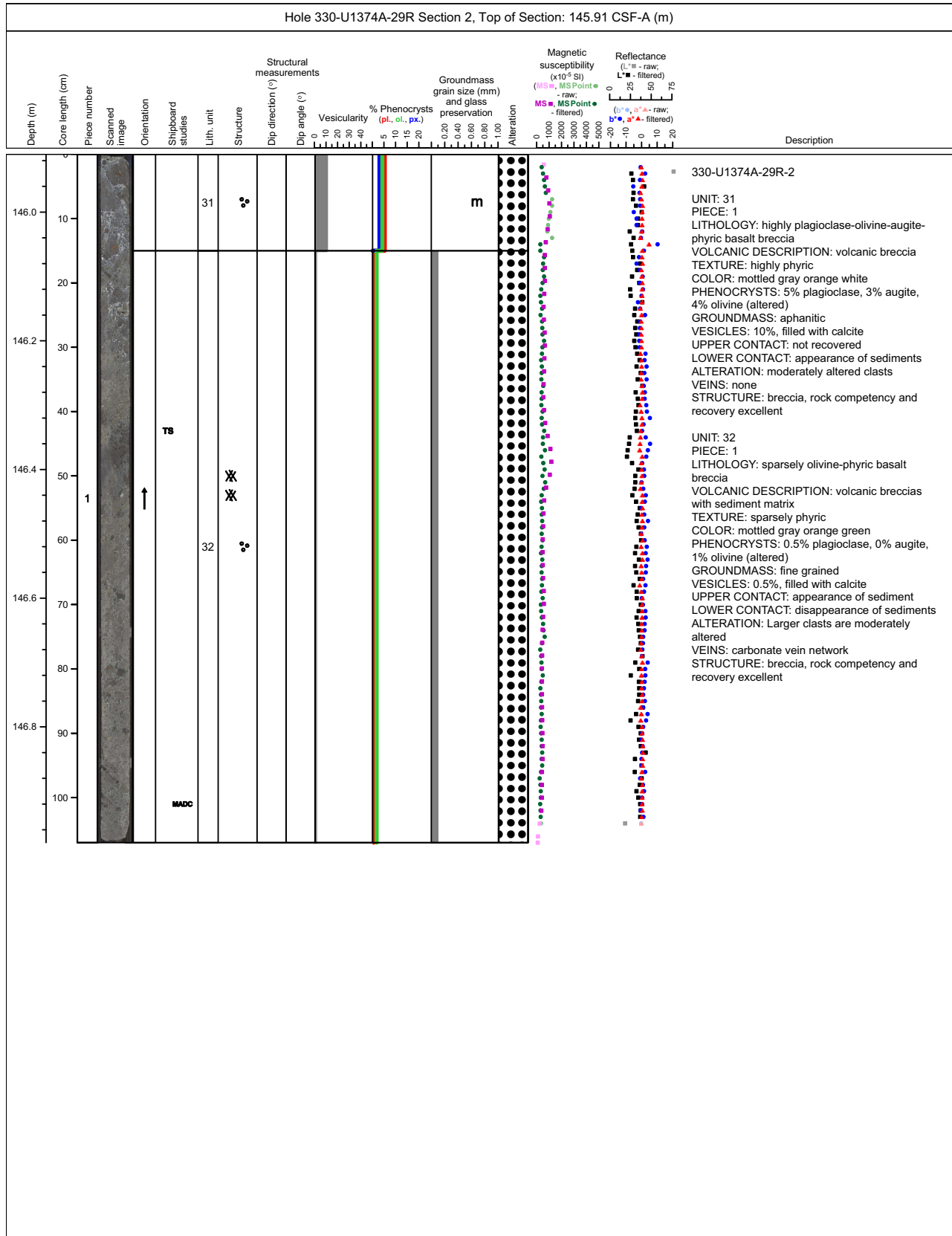


Figure F7. Symbols and nomenclature used for igneous VCD standard graphic reports, Expedition 330. ICP-AES = inductively coupled plasma–atomic emission spectroscopy. Modified after Expedition 324 Scientists (2010).

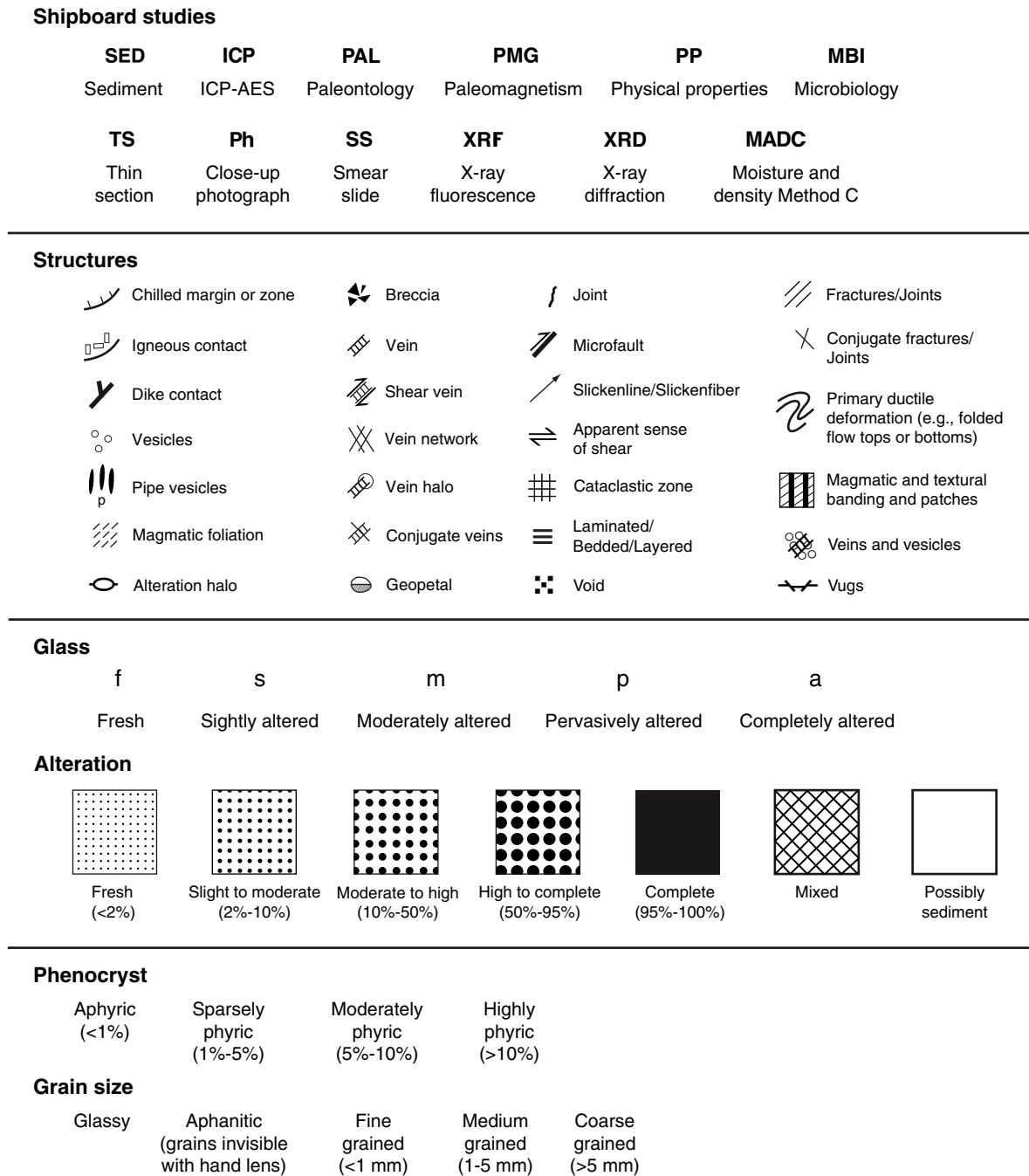


Figure F8. Vein description scheme, modified after Expedition 324 Scientists (2010).

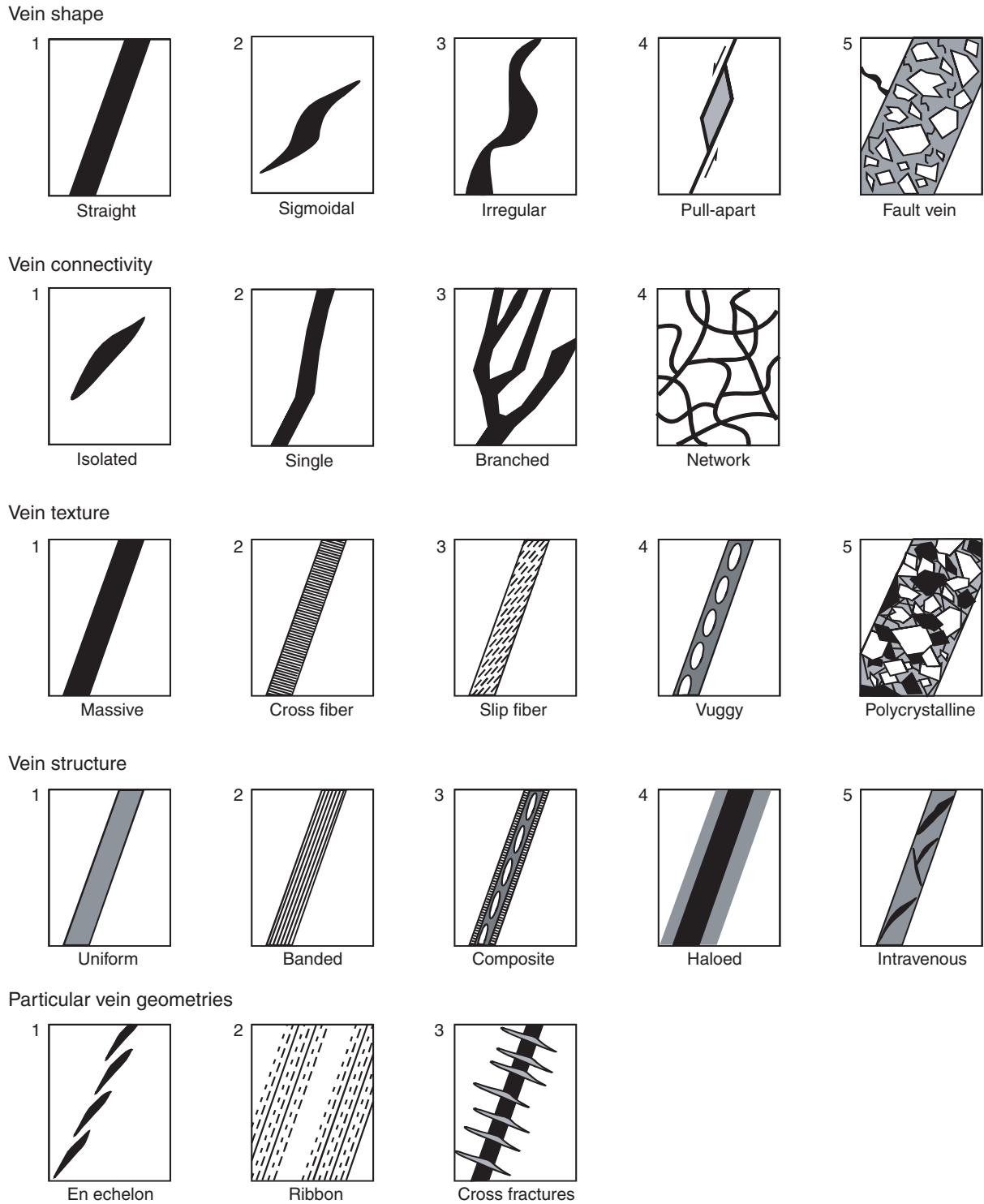
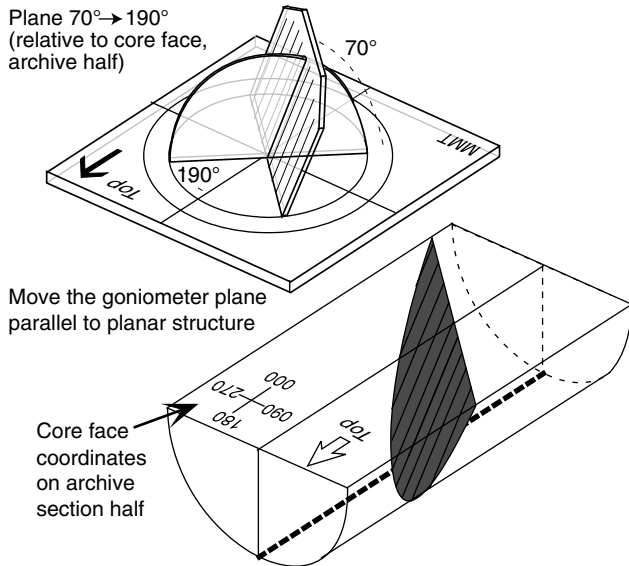
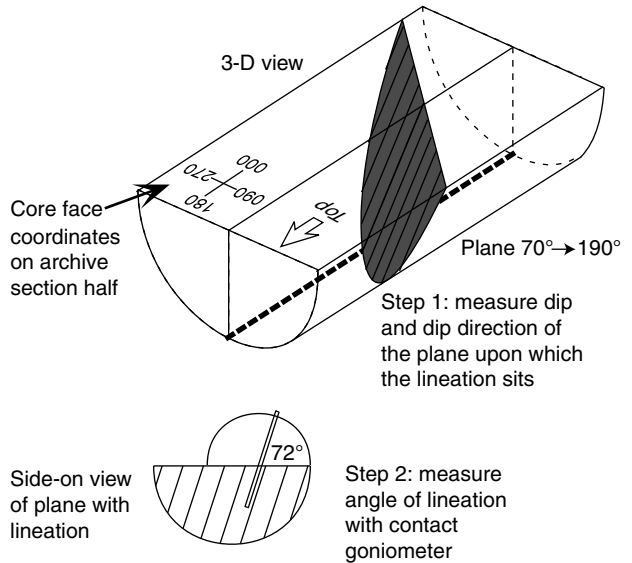


Figure F9. Conventions used to measure dip and dip direction of structural features during Expedition 330. **A, B.** Core face coordinates. The turnable (hinged) plane of the goniometer was rotated until parallel with the feature to be measured on the archive half. Data were recorded as dip angle and dip direction relative to archive-half core face coordinates. Values were then rotated to **(C)** core reference frame, with pseudonorth pointing out of the archive half. Dashed lines indicate obscured half of core. Modified from Shipboard Scientific Party (1997). MMT = M. Meschede tool (designed during ODP Leg 170).

A Measuring a plane in the archive-half core face frame



B Measuring a lineation in the archive-half core face frame



C Rotate from core face frame into core reference frame

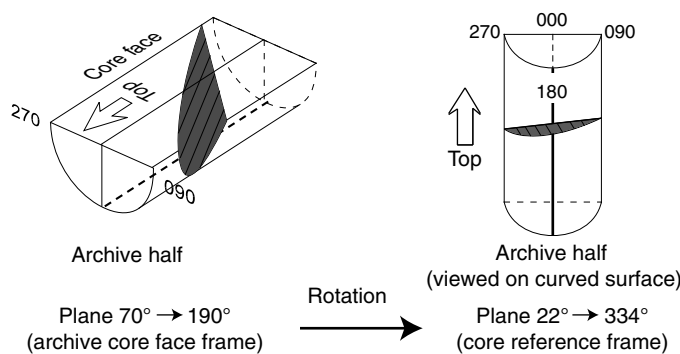


Figure F10. Example of igneous VCD standard graphic report showing several structural features, Expedition 330. Structural measurements are reported in the core reference frame; therefore, dip angles represent true angles of structures in situ. Dip directions, however, were affected by rotation during drilling and were measured relative to the split face of the core (Fig. F9).

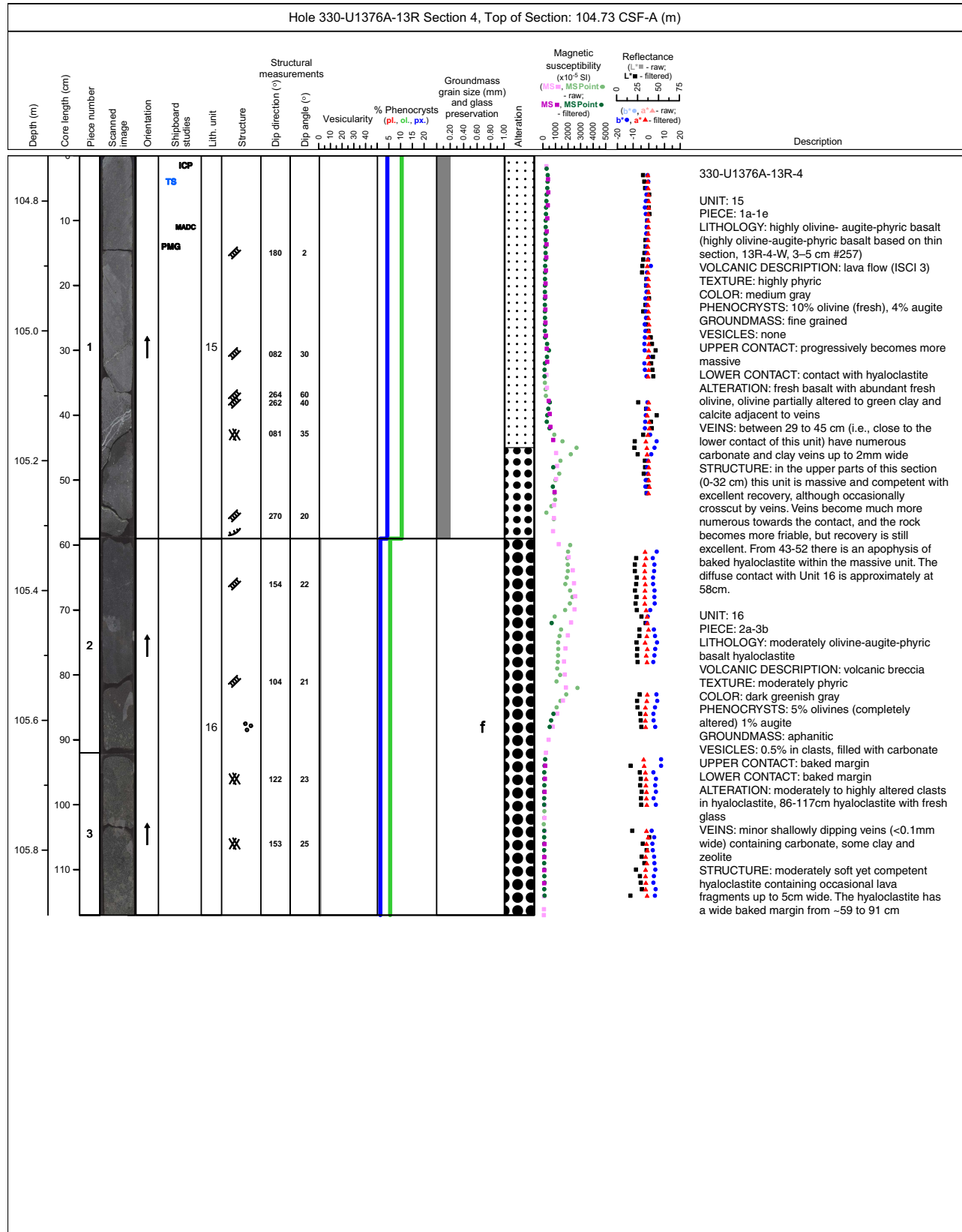


Figure F11. Photographs of goniometer used during Expedition 330 to measure dip and dip direction of planes in split cores (designed by M. Meschede, ODP Leg 170; Shipboard Scientific Party, 1997).

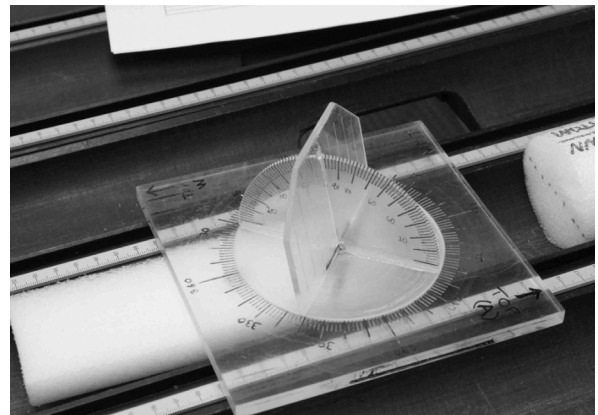
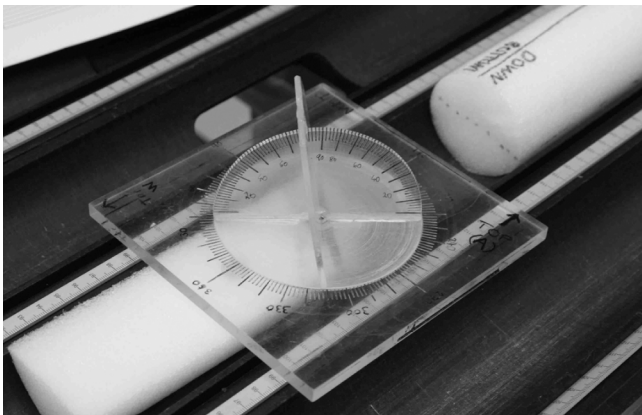
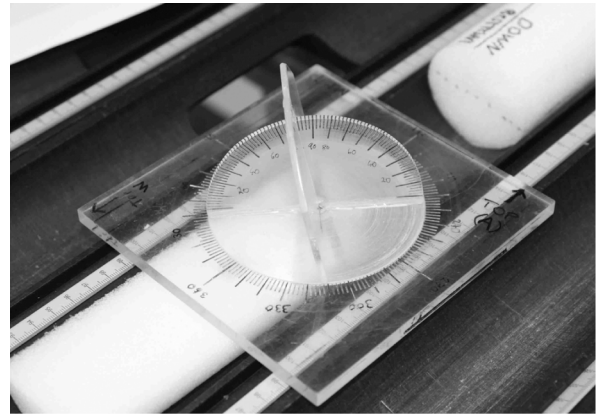
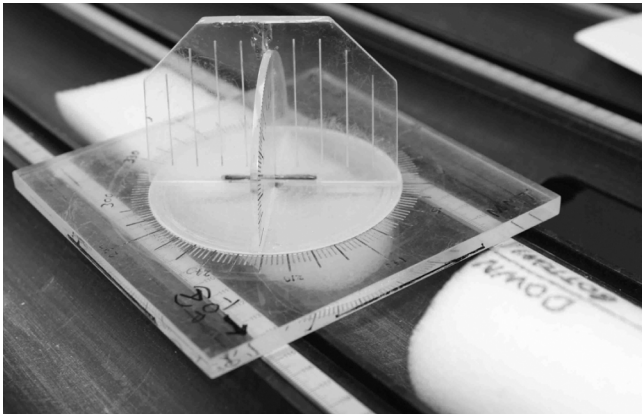


Figure F12. Sample coordinate system for (A) working and (B) archive core halves.

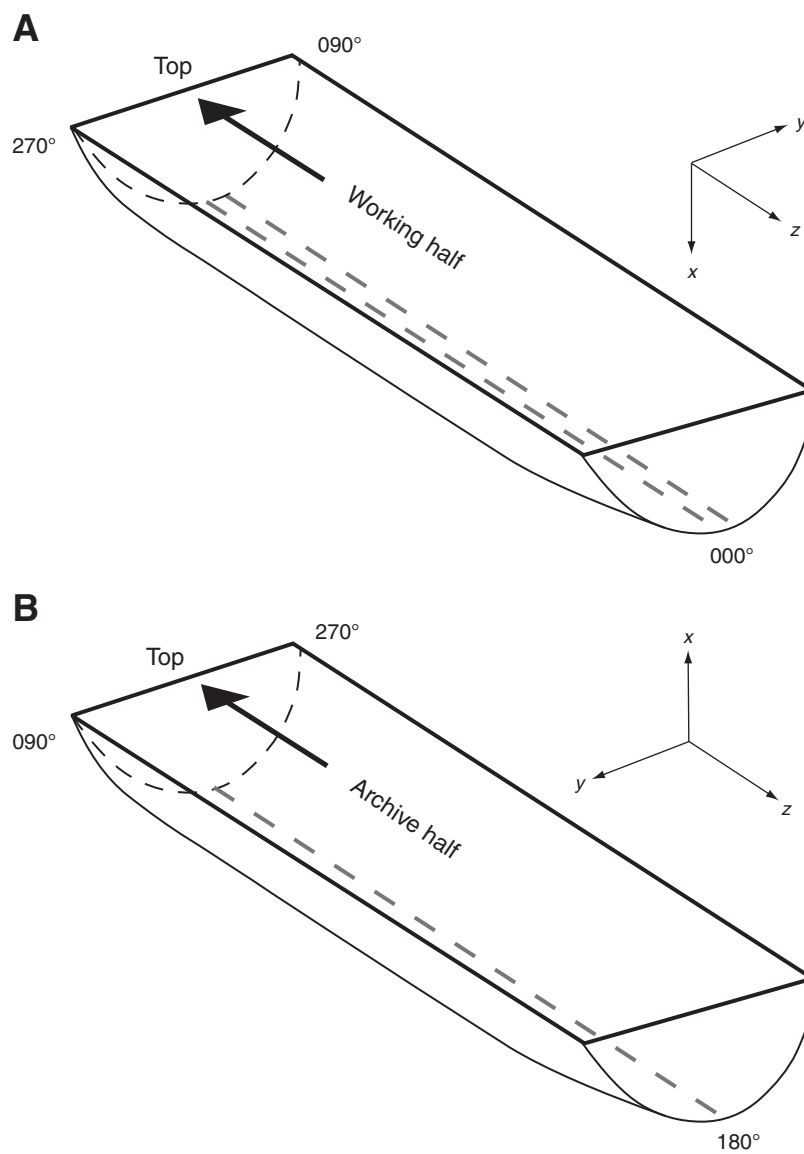


Figure F13. Power spectra for magnetic moments from the three axes of the superconducting quantum interference device (SQUID) cryogenic magnetometer. Note the prominent peaks near the dominant period of wave motion. Data were recorded at a ~ 2 Hz sampling rate on a relatively calm day on station. PSD = power spectral density.

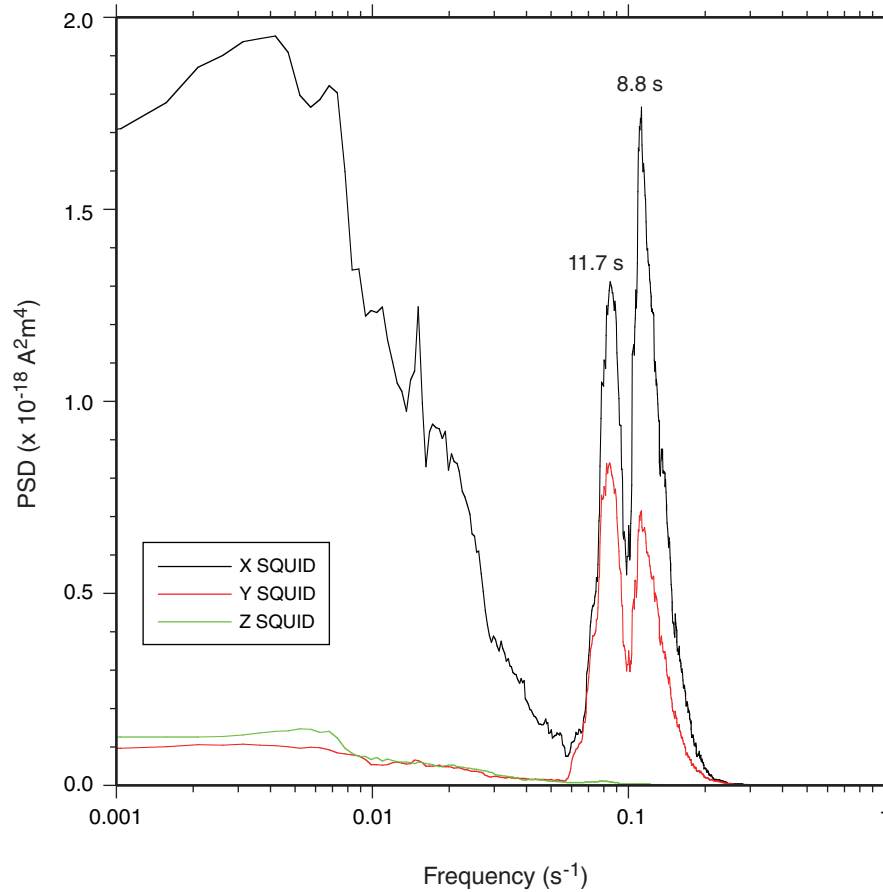




Figure F14. A–H. Zijderveld diagrams of representative archive-half core demagnetization data illustrating results of automated PCA technique. Open circles = projections of remanent magnetization onto vertical plane, solid circles = projections of remanent magnetization onto horizontal plane. Dark red arrows = PCA directions with misfits < 3.4, lighter red arrows = directions associated with misfits > 3.4. Inset box gives treatment range for PCA fit (A = anchored to origin, F = free of origin) and resulting misfit parameters. MAD = maximum angular deviation ($^{\circ}$), CSD = circular standard deviation, f = remanence, α = solid angle between unconstrained PCA fit and anchored to origin fit ($^{\circ}$). See “Paleomagnetism” for discussion of misfit parameters.

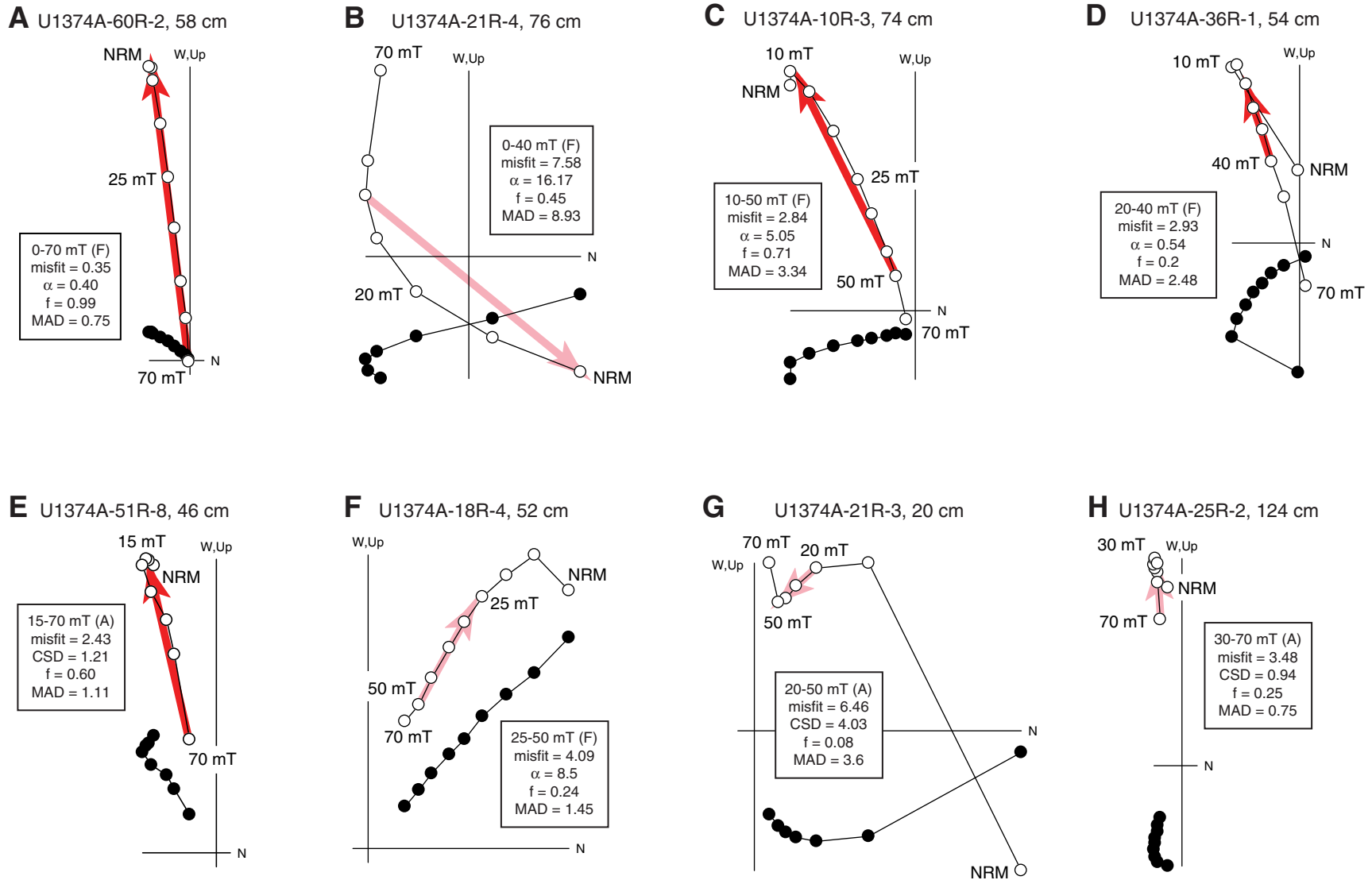


Figure F15. Summary statistics for automated PCA picks from archive-half core data. **A.** Distribution of misfit levels for data from Holes U1372A, U1373A, and U1374A. Note that all three cumulative distribution functions cross at a misfit value of ~3.4. **B–D.** Distribution of maximum angular deviation (MAD), deviation from origin (alpha), and percentage of vector difference sum (VDS) remanence. Their averages for the 40% of PCAs with misfit values < 3.4 are also presented.

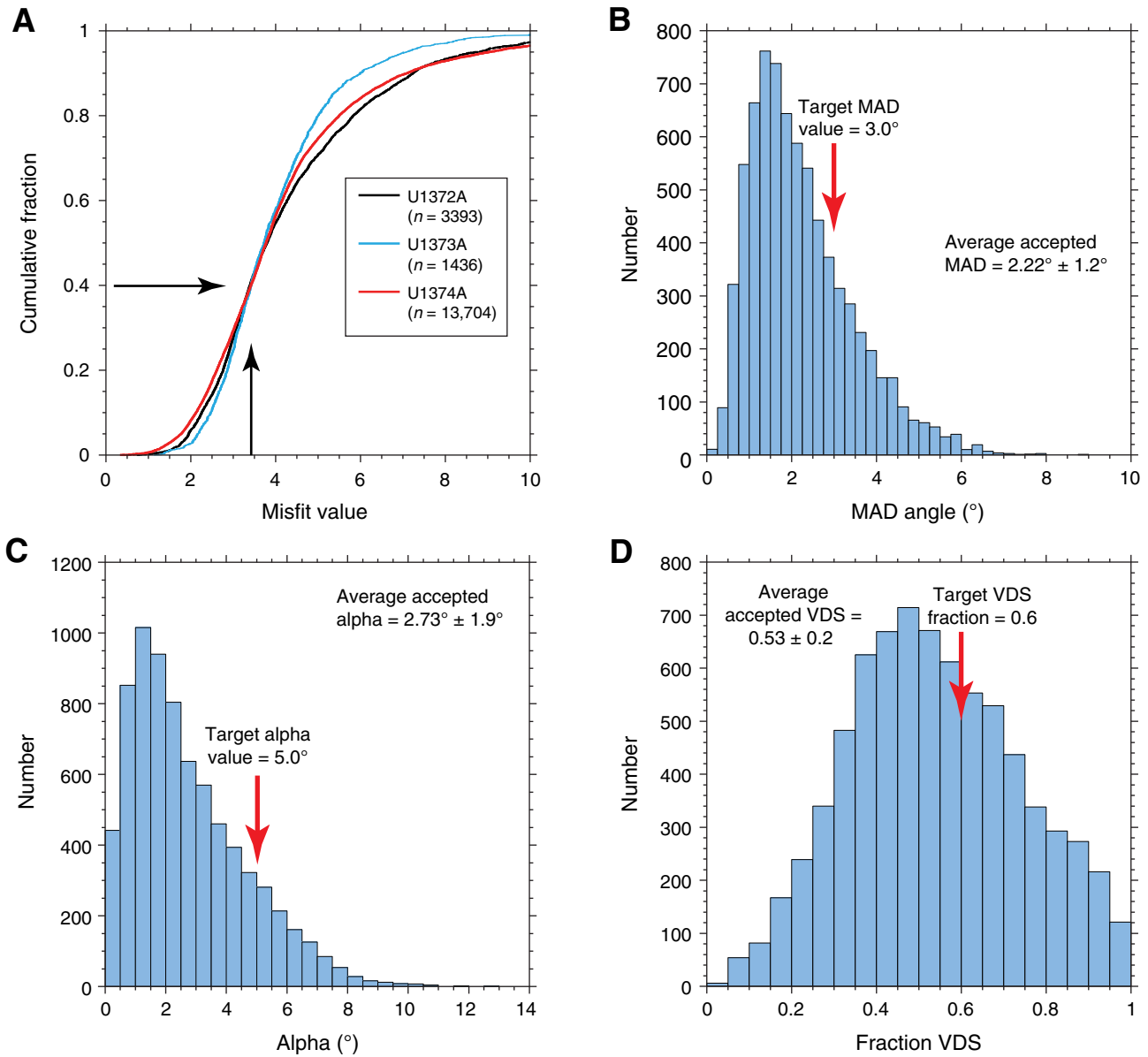


Figure F16. Data from Section 330-U1372A-9R-2 illustrating potential limitations of the piece-averaging technique. **A.** Archive-half demagnetization data (solid circles with lighter shading indicate a misfit > 3.4), discrete thermal demagnetization data (open squares), and discrete AF demagnetization data (open triangles). Average direction for entire piece (open circle) calculated from archive-half core data using Fisher statistics for individual PCA directions with misfit > 3.4. **B.** Vector endpoint diagrams for discrete samples and representative archive-half core intervals are shown in A. See Figure F14 caption for explanation of symbols. NRM = natural remanent magnetization.

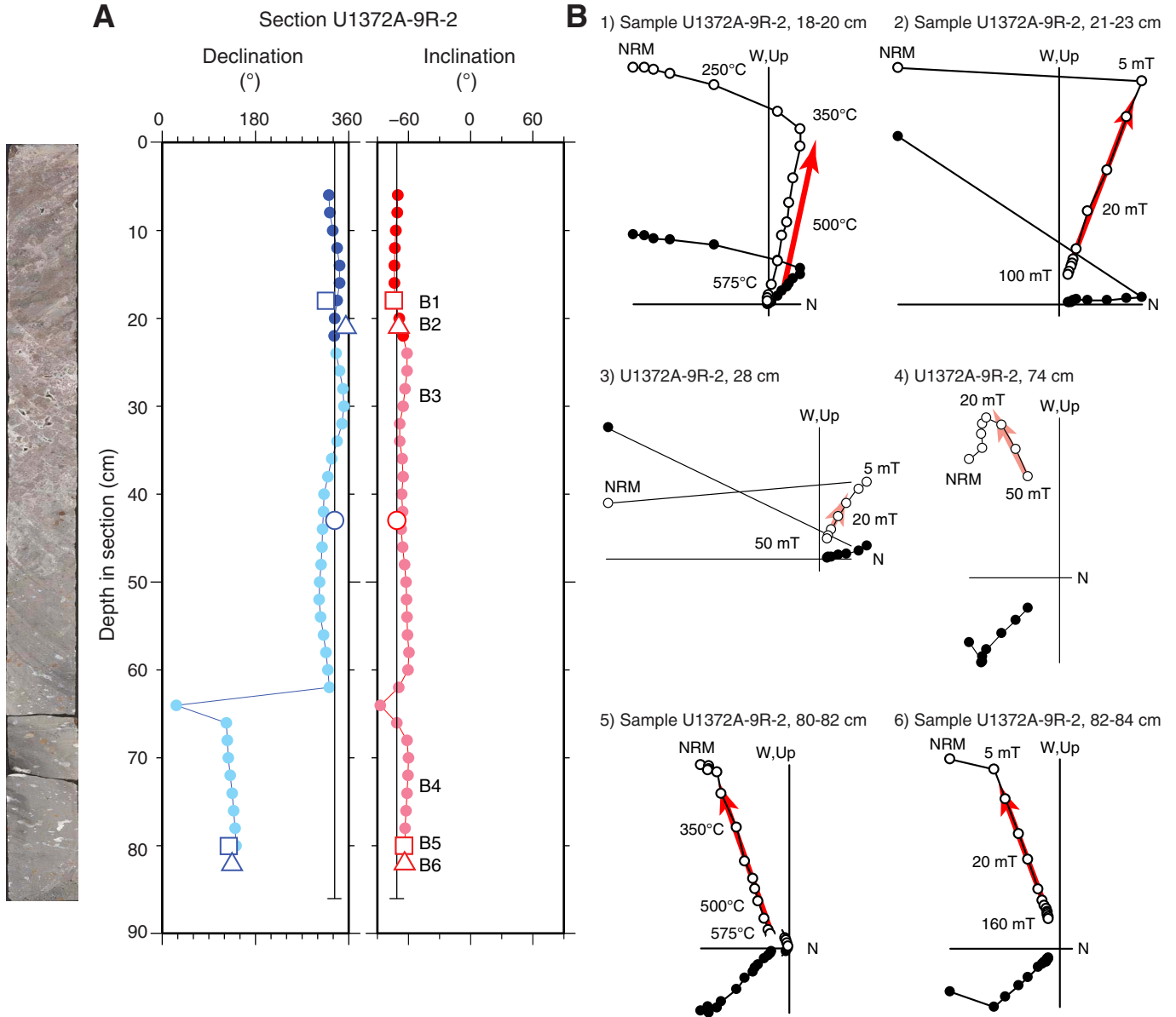


Figure F17. Equal-area plots showing discrete sample magnetization directions from standards (Std) measured in several positions on the cryogenic magnetometer. Open symbols = upper hemisphere, solid symbols = lower hemisphere. **A.** Representative results for two standard samples measured in all 24 positions using the SRM_DISCRETE program. Colors denote groups of orientations related by rotation about a common specimen coordinate axis. **B.** Results for four standards measured in a subset of six positions on the cryogenic magnetometer. Means and associated 95% confidence ellipses are indicated by blue circles and purple ellipses, respectively. These means are compared with the accepted values for these standards (black circles).

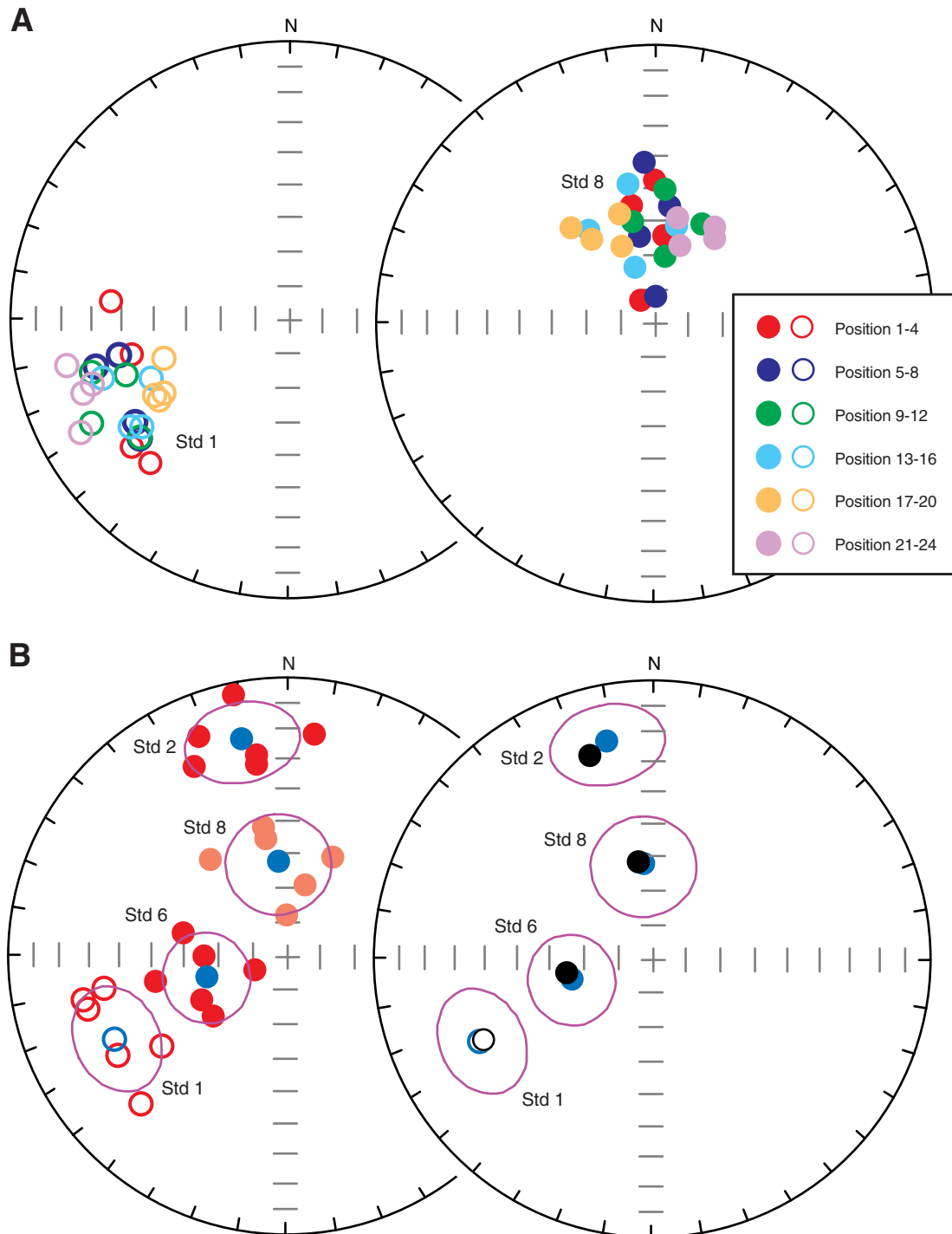


Figure F18. Wireline tool strings used during Expedition 330. HNGS = Hostile Environment Natural Gamma Ray Sonde, APS = Accelerator Porosity Sonde, HLDS = Hostile Environment Litho-Density Sonde, GPIT = General Purpose Inclinometry Tool, DIT = Dual Induction Tool, DSI = Dipole Shear Sonic Imager, FMS = Formation MicroScanner, UBI = Ultrasonic Borehole Imager, GBM = Göttingen Borehole Magnetometer.

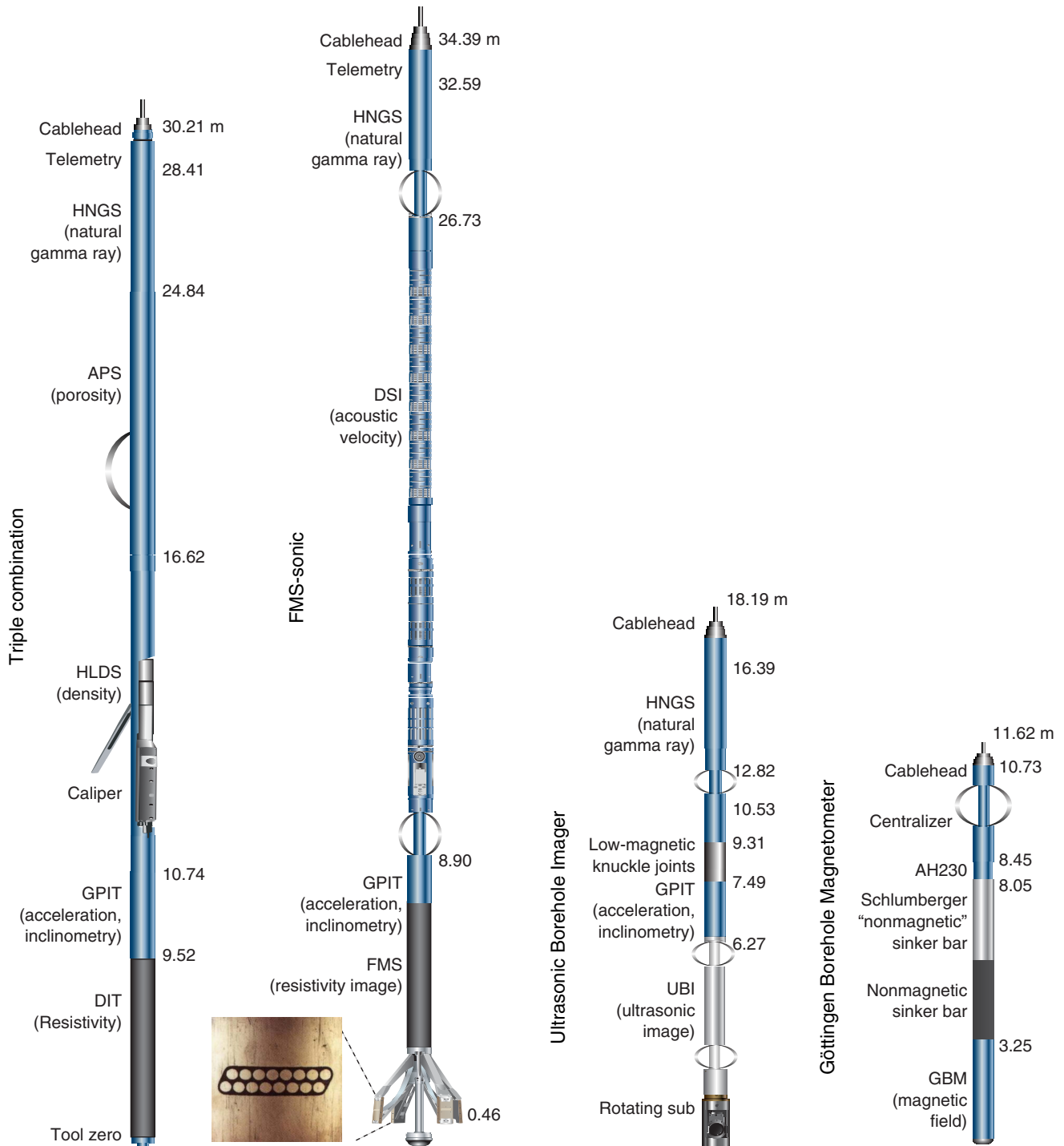


Figure F19. A. Schematic diagram of Göttingen Borehole Magnetometer. B. Specifications of μ FORS-36M fiber-optic rate sensor (LITEF). C. Dependence on Earth's rotation rate from latitude (θ) measured with fiber-optic rate sensors.

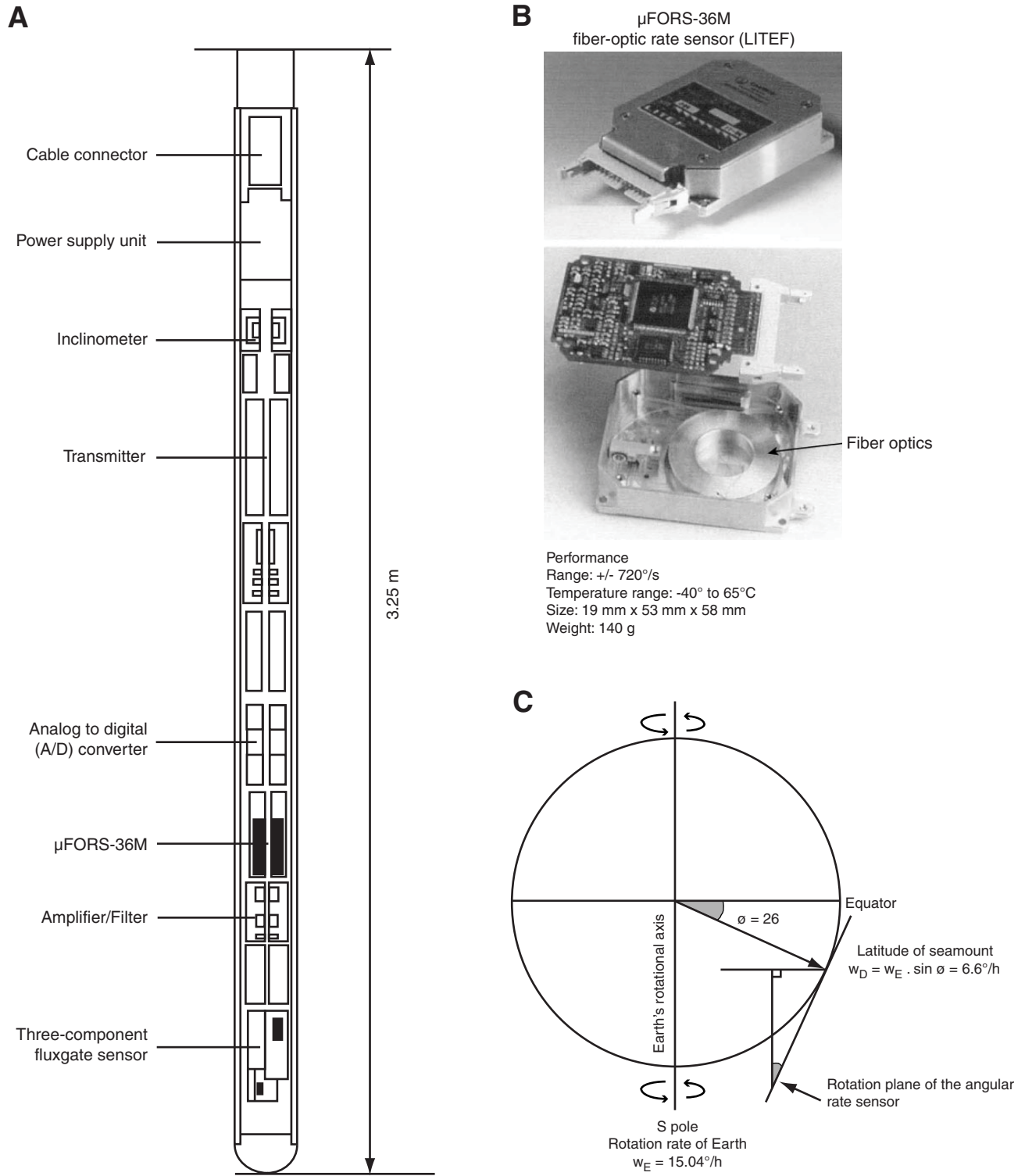


Figure F20. Temperature drift of GBM fiber-optic gyros (FOGs).

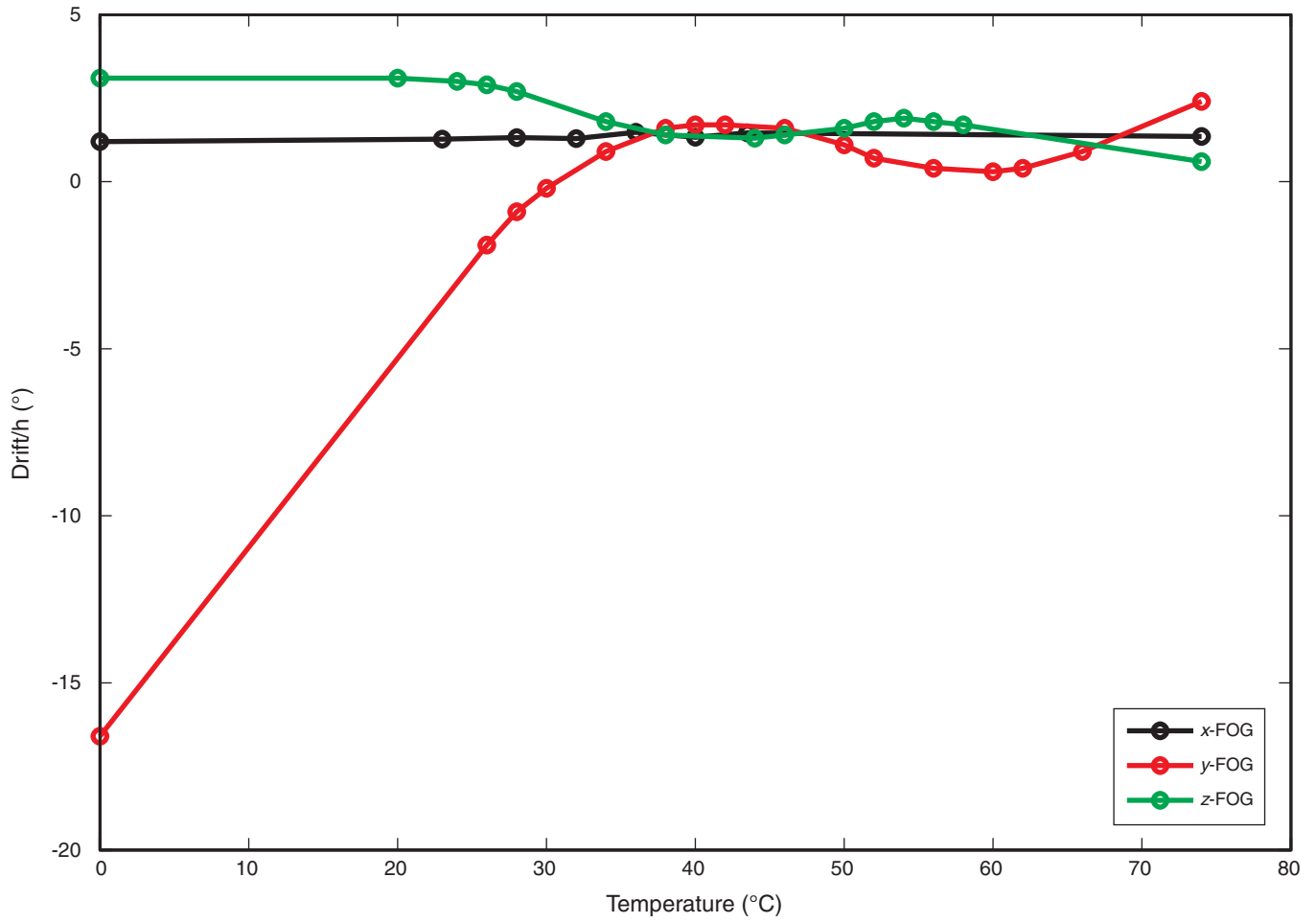


Table T1. Age estimates of Cenozoic calcareous nannofossil datum events, Expedition 330. (Continued on next page.)

Biostratigraphic event	Age (Ma)	Zone/Subzone base	Reference
B <i>Emiliana huxleyi</i>	0.29	CN15	Lourens et al., 2004
T <i>Pseudoemiliana lacunosa</i>	0.44	CN14b	Lourens et al., 2004
Tc <i>Reticulofenestra asanoi</i>	0.91		Lourens et al., 2004
Br <i>Gephyrocapsa</i> (>4 µm)	1.01		Lourens et al., 2004
Bc <i>Reticulofenestra asanoi</i>	1.14		Lourens et al., 2004
T <i>Gephyrocapsa</i> (>5.5 µm)	1.26		Lourens et al., 2004
T <i>Helicosphaera sellii</i>	1.34		Lourens et al., 2004
B <i>Gephyrocapsa</i> (>5.5 µm)	1.56		Lourens et al., 2004
T <i>Calcidiscus macintyreii</i>	1.61		Lourens et al., 2004
B <i>Gephyrocapsa</i> (>4 µm)	1.69		Lourens et al., 2004
T <i>Discoaster brouweri</i>	1.93	CN13	Lourens et al., 2004
Bc <i>Discoaster triradiatus</i>	2.14		Lourens et al., 2004
T <i>Discoaster pentaradiatus</i>	2.39	CN12d	Lourens et al., 2004
T <i>Discoaster surculus</i>	2.49	CN12c	Lourens et al., 2004
T <i>Discoaster tamalis</i>	2.80	CN12b	Lourens et al., 2004
T <i>Sphenolithus</i> spp.	3.54		Lourens et al., 2004
T <i>Reticulofenestra pseudoumbilicus</i>	3.70	CN12a	Lourens et al., 2004
T <i>Ceratolithus acutus</i>	5.04		Lourens et al., 2004
B <i>Ceratolithus rugosus</i>	5.05		Lourens et al., 2004
T <i>Triquetrorhabdulus rugosus</i>	5.28	CN10c	Lourens et al., 2004
B <i>Ceratolithus larrymayeri</i>	5.34		Lourens et al., 2004
B <i>Ceratolithus acutus</i>	5.35	CN10b	Lourens et al., 2004
T <i>Discoaster quinqueramus</i>	5.58	CN10a	Lourens et al., 2004
Tc <i>Nicklithus amplificus</i>	5.98		Lourens et al., 2004
X <i>Nicklithus amplificus</i> / <i>T. rugosus</i>	6.79		Lourens et al., 2004
B <i>Nicklithus amplificus</i>	6.91		Lourens et al., 2004
B <i>Amaurolithus</i> spp.	7.36		Lourens et al., 2004
B <i>Discoaster berggrenii</i>	8.29	CN9a	Lourens et al., 2004
T <i>Catinaster calyculus</i>	9.67		Lourens et al., 2004
T <i>Discoaster hamatus</i>	9.69	CN8	Lourens et al., 2004
T <i>Catinaster coalitus</i>	9.69		Lourens et al., 2004
B <i>Discoaster hamatus</i>	10.55	CN7	Lourens et al., 2004
T <i>Coccolithus miopelagicus</i>	10.60		Raffi et al., 2006
B <i>Catinaster calyculus</i>	10.76		Lourens et al., 2004
B <i>Catinaster coalitus</i>	10.89	CN6	Lourens et al., 2004
Tc <i>Discoaster kugleri</i>	11.58		Lourens et al., 2004
Bc <i>Discoaster kugleri</i>	11.86	CN5b	Lourens et al., 2004
T <i>Coronocyclus nitescens</i>	12.12		Lourens et al., 2004
T <i>Calcidiscus premacintyreii</i>	12.45		Lourens et al., 2004
Tc <i>Cyclicargolithus floridanus</i>	13.33		Lourens et al., 2004
T <i>Sphenolithus heteromorphus</i>	13.53	CN5a	Lourens et al., 2004
T <i>Helicosphaera ampliaptera</i>	14.91	CN4	Lourens et al., 2004
Tc <i>Discoaster deflandrei</i>	15.66		Raffi et al., 2006
B <i>Discoaster petaliformis</i> *	15.70		Raffi et al., 2006
Bc <i>Sphenolithus heteromorphus</i>	17.71	CN3	Lourens et al., 2004
Tc <i>Sphenolithus belemnus</i>	17.95		Lourens et al., 2004
T <i>Triquetrorhabdulus carinatus</i>	18.28		Lourens et al., 2004
B <i>Sphenolithus belemnus</i>	19.03	CN2	Lourens et al., 2004
B <i>Helicosphaera ampliaptera</i>	20.43		Lourens et al., 2004
X <i>Helicosphaera euphratis</i> / <i>H. carteri</i>	20.92		Lourens et al., 2004
Tc <i>Triquetrorhabdulus carinatus</i>	22.09		Raffi et al., 2006
B <i>Sphenolithus disbelemnus</i>	22.76		Lourens et al., 2004
T <i>Sphenolithus delphix</i>	23.1		Lourens et al., 2004
B <i>Sphenolithus delphix</i>	23.2		Lourens et al., 2004
T <i>Sphenolithus ciproensis</i>	24.4	CN1	Blaj et al., 2009
X <i>Triquetrorhabdulus longus</i> / <i>T. carinatus</i>	24.7		Blaj et al., 2009
Tc <i>Cyclicargolithus abisectus</i>	24.7		Lyle, Wilson, Janacek, et al., 2002
T <i>Sphenolithus distentus</i>	26.8	CP19b	Blaj et al., 2009
T <i>Sphenolithus predistentus</i>	26.9		Blaj et al., 2009
B <i>Sphenolithus ciproensis</i>	27.1	CP19a	Blaj et al., 2009
T <i>Sphenolithus pseudoradians</i>	28.8		Berggren et al., 1995
B <i>Sphenolithus distentus</i>	30.0	CP18	Blaj et al., 2009
T <i>Reticulofenestra umbilicus</i> (>14 µm)	32.0	CP17	Blaj et al., 2009
T <i>Isthmolithus recurvus</i>	32.5		Villa et al., 2008
T <i>Coccolithus formosus</i>	32.9	CP16c	Blaj et al., 2009
T <i>Discoaster saipanensis</i>	34.4	CP16a	Blaj et al., 2009
T <i>Discoaster barbadiensis</i>	34.8		Blaj et al., 2009

Table T1 (continued).

Biostratigraphic event	Age (Ma)	Zone/Subzone base	Reference
T <i>Reticulofenestra reticulata</i>	35.2		Backman, 1987
B <i>Isthmolithus recurvus</i>	36.6	CP15b	Backman, 1984
B <i>Chiasmolithus oamaruensis</i>	37.0		Berggren et al., 1995
T <i>Chiasmolithus grandis</i>	37.1	CP15a	Backman, 1987
B <i>Dictyococcites bisectus</i> (>10 µm)	38.0		Berggren et al., 1995
T <i>Chiasmolithus solitus</i>	40.4	CP14b	Berggren et al., 1995
B <i>Reticulofenestra reticulata</i>	42.0		Berggren et al., 1995
T <i>Nannotetrina</i> spp.	42.3		Backman, 1987
B <i>Reticulofenestra umbilicus</i> (>14 µm)	42.5		Backman, 1987
T <i>Nannotetrina fulgens</i>	43.4		Backman, 1984
T <i>Chiasmolithus gigas</i>	44.0	CP13c	Backman, 1984
B <i>Sphenolithus furcatolithoides</i>	45.8		Jovane et al., 2007
B <i>Chiasmolithus gigas</i>	46.1	CP13b	Agnini et al., 2006
B <i>Nannotetrina fulgens</i>	46.8	CP13a	Agnini et al., 2006
B <i>Nannotetrina cristata</i>	48.0		Agnini et al., 2006
T <i>Discoaster lodoensis</i>	48.4		Agnini et al., 2006
B <i>Discoaster sublodoensis</i> (5 rayed)	49.5	CP12	Agnini et al., 2006
B <i>Dictyococcites/Reticulofenestra</i>	50.7		Agnini et al., 2006
T <i>Tribrachiatus orthostylus</i>	50.7	CP11	Agnini et al., 2006
B <i>Girgisia gammation</i>	52.8		Agnini et al., 2007
B <i>Discoaster lodoensis</i>	53.1	CP10	Agnini et al., 2007
T <i>Tribrachiatus contortus</i>	53.5	CP9b	Agnini et al., 2007
B <i>Sphenolithus radians</i>	53.5	CP9b	Agnini et al., 2007
B <i>Tribrachiatus orthostylus</i>	53.7		Agnini et al., 2007
B <i>Discoaster diastypus</i>	54.1		Agnini et al., 2007
T <i>Fasciculithus</i> spp.	54.7		Agnini et al., 2007
B <i>Rhomboaster bramlettei</i>	55.0	CP9a	Agnini et al., 2007
B <i>Rhomboaster</i> spp.	55.0		Agnini et al., 2007
T <i>Ericsonia robusta</i>	55.9		Agnini et al., 2007
B <i>Discoaster multiradiatus</i>	56.0	CP8	Agnini et al., 2007
B <i>Discoaster okadai</i>	56.2		Agnini et al., 2007
B <i>Discoaster nobilis</i>	56.2	CP7	Agnini et al., 2007
B <i>Discoaster backmanii</i>	56.9		Agnini et al., 2007
B <i>Discoaster mohleri</i>	57.6	CP6	Agnini et al., 2007
B <i>Fasciculithus clinatus</i>	57.7		Agnini et al., 2007
B <i>Heliolithus kleinpellii</i>	58.0	CP5	Agnini et al., 2007
B <i>Sphenolithus anarrhopus</i>	58.1		Agnini et al., 2007
B <i>Heliolithus cantabriae</i>	58.3		Agnini et al., 2007
B <i>Fasciculithus tympaniformis</i>	59.9	CP4	Agnini et al., 2007
B <i>Ellipsolithus macellus</i>	62.2	CP3	Berggren et al., 1995
B <i>Chiasmolithus danicus</i>	63.8	CP2	Berggren et al., 1995
B <i>Cruciplacolithus tenuis</i>	64.5	CP1b	Berggren et al., 1995
B <i>Cruciplacolithus primus</i>		CP1a	Berggren et al., 1995
B <i>Biantholithus sparsus</i>		CP1	Berggren et al., 1995

B = base, T = top, Tc = top common, Bc = base common, Br = base reentrance, X = abundance crossover. * = *Discoaster signus* in Raffi et al. (2006).

Table T2. Age estimates of Cretaceous calcareous nannofossil datum events, Expedition 330.

Biostratigraphic event	Age (Ma)	Zone/Subzone base	Reference
T Cretaceous taxa (<i>Micula prinsii</i>)	65.0		Berggren et al., 1995
B <i>Micula prinsii</i>	65.4	CC26b	Erba et al., 1995
B <i>Nephrolithus frequens</i>	65.8	CC26	Erba et al., 1995; Sissingh, 1977
B <i>Micula murus</i>	66.2	CC25c	Erba et al., 1995
B <i>Lithraphidites quadratus</i>	67.5	CC25b	Erba et al., 1995
T <i>Reinhardtites levis</i>	69.2	CC24	Erba et al., 1995; Sissingh, 1977
T <i>Tranolithus orionatus</i>	69.6	CC24	Erba et al., 1995; Sissingh, 1977
T <i>Uniplanarius trifidum</i>	71.3		Erba et al., 1995
T <i>Aspidolithus parvus</i>	74.6	CC23a	Erba et al., 1995
T <i>Eiffelithus eximius</i>	75.3		Erba et al., 1995; Sissingh, 1977
B <i>Uniplanarius trifidum</i>	76.0	CC22	Erba et al., 1995; Sissingh, 1977
B <i>Uniplanarius sissinghii</i>	77.0	CC21	Erba et al., 1995; Sissingh, 1977
B <i>Ceratolithoides aculeus</i>	78.5	CC20	Erba et al., 1995; Sissingh, 1977
B <i>Misceomarginatus pleniporus</i>	79.5		Erba et al., 1995
T <i>Marthasterites furcatus</i>	80.6	CC19	Erba et al., 1995; Sissingh, 1977
B <i>Ceratolithoides verbeekii</i>	82.0		Erba et al., 1995
B <i>Aspidolithus parvus constrictus</i>	82.5	CC18c	Erba et al., 1995
B <i>Aspidolithus parvus</i>	83.4	CC18	Erba et al., 1995; Sissingh, 1977
B <i>Arkhangelskiella cymbiformis</i>	83.5		Erba et al., 1995

B = base, T = top.

Table T3. Age estimates of Cenozoic planktonic foraminifer datum events, Expedition 330. (Continued on next page.)

Biostratigraphic event	Age (Ma)	Zone/Subzone base	Reference
T <i>Globorotalia (Truncorotalia) tosaensis</i>	0.61	PT1b	Srinivasan and Sinha, 1992
T <i>Globigerinoides fistulosus</i>	1.77	PT1a	Shackleton et al., 1990
B <i>Globorotalia (Truncorotalia) truncatulinoides</i>	1.92		Chaisson and Pearson, 1997
T <i>Globigerinoides extremus</i>	1.98		Chaisson and Pearson, 1997
T <i>Globorotalia pseudomiocenica</i>	2.30	PL6	Berggren et al., 1995
T <i>Globoturborotalita woodi</i>	2.30		Chaisson and Pearson, 1997
T <i>Globorotalia (Menardella) multicamerata</i>	2.98		Berggren et al., 1995
T <i>Dentoglobigerina altispira</i>	3.47	PL5	Shackleton et al., 1995
T <i>Sphaeroidinellopsis seminulina</i>	3.59	PL4	Shackleton et al., 1995
T <i>Globorotalia (Hirsutella) margaritae</i>	3.85	PL3	Chaisson and Pearson, 1997
X <i>Pulleniatina sinistral</i> → dextral	4.08		Chaisson and Pearson, 1997
T <i>Globoturborotalita nepenthes</i>	4.37	PL2	Chaisson and Pearson, 1997
B <i>Globorotalia (Menardella) exilis</i>	4.45		Chaisson and Pearson, 1997
T <i>Globorotalia (Hirsutella) cibaensis</i>	4.61	PL1b	Berggren et al., 1995
B <i>Sphaeroidinella dehiscens</i> s.l.	5.54		Chaisson and Pearson, 1997
B <i>Globorotalia tumida</i>	5.57	PL1a	Shackleton et al., 1995
B <i>Turborotalita humilis</i>	5.81		Chaisson and Pearson, 1997
B <i>Globorotalia (Hirsutella) margaritae</i>	6.08		Chaisson and Pearson, 1997
T <i>Globorotalia languaensis</i>	6.13	M14	Berggren et al., 1995
B <i>Globorotalia plesiotumida</i>	8.58	M13b	Chaisson and Pearson, 1997
B <i>Neogloboquadrina acostaensis</i>	9.83	M13a	Chaisson and Pearson, 1997
T <i>Paragloborotalia mayeri</i>	10.46	M12	Chaisson and Pearson, 1997
B <i>Globoturborotalita decoraperta</i>	11.49		Chaisson and Pearson, 1997
B <i>Globoturborotalita nepenthes</i>	11.63	M11	Turco et al., 2002
T <i>Globorotalia (Fohsella) fohsi</i> s.l. (inc. <i>lobata</i> and <i>robusta</i>)	11.79	M10	Chaisson and Pearson, 1997
B <i>Globorotalia (Fohsella) fohsi robusta</i>	13.13	M9b	Chaisson and Pearson, 1997
B <i>Globorotalia (Fohsella) fohsi</i> s.l.	13.41	M8/M9a	Chaisson and Pearson, 1997
T <i>Globorotalia praescitula</i>	13.73		Turco et al., 2002
B <i>Globorotalia (Fohsella) "praefohsi"</i>	13.77		Turco et al., 2002
T <i>Globorotalia (Fohsella) peripheroronda</i>	13.80		Turco et al., 2002
T <i>Clavatorella bermudezi</i>	13.82		Shackleton et al., 1999
B <i>Globorotalia (Fohsella) peripheroacuta</i>	14.24	M7	Pearson and Chaisson, 1997
B <i>Globorotalia (Menardella) praemenardii</i>	14.38		Lourens et al., 2004
T <i>Globigerinatella insueta</i>	14.66		Pearson and Chaisson, 1997
B <i>Orbulina</i> spp.	14.74	M6	Shackleton et al., 1999
B <i>Clavatorella bermudezi</i>	14.89		Pearson and Chaisson, 1997
B <i>Globorotalia (Menardella) archeomenardii</i>	16.26		Pearson and Chaisson, 1997
B <i>Praeorbulina glomerosa</i>	16.27	M5b	Berggren et al., 1995
B <i>Praeorbulina sicana</i>	16.97	M5a	Berggren et al., 1995
T <i>Catapsydrax dissimilis</i>	17.54	M4	Berggren et al., 1995
B <i>Globigerinatella insueta</i>	17.59	M3	Pearson and Chaisson, 1997
T <i>Globoquadrina binaiensis</i>	19.09		Pearson and Chaisson, 1997
T <i>Paragloborotalia kugleri</i>	21.12	M2	Berggren et al., 1995
T <i>Paragloborotalia pseudokugleri</i>	21.31		Berggren et al., 1995
B <i>Globoquadrina dehiscens</i>	22.44	M1b	Berggren et al., 1995
T <i>Globigerina ciperensis</i>	22.90		Pearson and Chaisson, 1997
B <i>Paragloborotalia kugleri</i>	22.96	M1a	Berggren et al., 1995
B <i>Paragloborotalia pseudokugleri</i>	25.2		Berggren et al., 1995
T <i>Paragloborotalia opima</i>	26.9	O6	Wade et al., 2007
Tc <i>Chiloguembelina cubensis</i>	28.0	O5	Wade et al., 2007
B <i>Globigerina angulisuturalis</i>	29.2	O4	Berggren et al., 1995
T <i>Subbotina angiporoides</i>	29.8		Berggren et al., 1995
T <i>Turborotalia ampliapertura</i>	30.3	O3	Berggren et al., 1995
B <i>Paragloborotalia opima</i>	30.8		Berggren et al., 1995
T <i>Pseudohastigerina naguewichiensis</i>	32.0	O2	Berggren et al., 1995
T <i>Hantkenina</i> spp.	33.8	O1	Berggren and Pearson, 2005
T <i>Turborotalia cerroazulensis</i>	33.9		Berggren and Pearson, 2005
T <i>Globigerinatheka index</i>	34.5	E16	Berggren and Pearson, 2005
T <i>Globigerinatheka semiinvoluta</i>	35.8	E15	Berggren and Pearson, 2005
T <i>Morozovelloides crassatus</i>	38.1	E14	Wade, 2004
T <i>Acarinina mcgowrani</i>	38.1		Wade, 2004
T <i>Orbulinoides beckmanni</i>	40.0	E13	Wade, 2004
B <i>Orbulinoides beckmanni</i>	40.8	E12	Berggren et al., 1995
T <i>Acarinina bullbrooki</i>	40.8		Berggren et al., 1995
T <i>Guembelitrinoides nuttalli</i>	42.3	E11	Berggren and Pearson, 2005
B <i>Turborotalia pomeroli</i>	42.4		Berggren et al., 1995
B <i>Morozovelloides lehneri</i>	43.5		Berggren et al., 1995

Table T3 (continued).

Biostratigraphic event	Age (Ma)	Zone/Subzone base	Reference
T <i>Morozovella aragonensis</i>	43.6	E10	Berggren et al., 1995
B <i>Globigerinatheka kugleri</i>	45.8	E9	Berggren et al., 1995
B <i>Guembelitrinoides nutalli</i>	49.0	E8	Hancock et al., 2002
B <i>Acarinina cuneicamerata</i>	50.4	E7	Hancock et al., 2002
B <i>Astrorotalia palmerae</i>	50.4		Berggren et al., 1985
T <i>Morozovella subbotinae</i>	50.8	E6	Berggren and Pearson, 2005
B <i>Acarinina pentacamerata</i>	50.8		Berggren and Pearson, 2005
B <i>Morozovella aragonensis</i>	52.3	E5	Berggren et al., 1995
T <i>Subbotina velascoensis</i>	53.5		Berggren et al., 1995
T <i>Morozovella aequa</i>	53.6		Berggren et al., 1995
B <i>Morozovella lensiformis</i>	54.0	E4	Berggren et al., 1995
T <i>Morozovella velascoensis</i>	54.5	E3	Berggren and Pearson, 2005
B <i>Morozovella gracilis</i>	54.7		Berggren et al., 1995
B <i>Pseudohastigerina wilcoxensis</i>	55.4	E2	Berggren and Pearson, 2005
B <i>Globanomalina australiformis</i>	55.5		Berggren et al., 1995
B <i>Acarinina sibaiyaensis</i>	55.5	E1	Berggren and Pearson, 2005
T <i>Morozovella acuta</i>	55.7		Berggren et al., 1995
B <i>Morozovella subbotinae</i>	55.9		Berggren et al., 1995
T <i>Globanomalina pseudomenardii</i>	55.9	P5	Berggren et al., 1995
T <i>Acarinina mckannai</i>	56.3		Berggren et al., 1995
B <i>Acarinina soldadoensis</i>	56.5	P4c	Berggren et al., 1995
T <i>Acarinina subsphaerica</i>	57.1	P4b	Berggren et al., 1995
B <i>Acarinina mckannai</i>	59.1		Berggren et al., 1995
B <i>Globanomalina pseudomenardii</i>	59.2	P4a	Berggren et al., 1995
B <i>Igorina albeari</i>	60.0	P3b	Berggren et al., 1995
B <i>Acarinina strabocella</i>	60.5		Olsson et al., 1999
B <i>Morozovella conicotruncata</i>	60.9		Berggren et al., 1995
B <i>Morozovella angulata</i>	61.0	P3a	Berggren et al., 1995
B <i>Igorina pusilla</i>	61.0		Berggren et al., 1995
B <i>Praemurica praeangulata</i>	61.2		Berggren et al., 1995
B <i>Praemurica uncinata</i>	61.2	P2	Berggren et al., 1995
B <i>Globanomalina imitata</i>	61.3		Berggren et al., 1995
B <i>Globanomalina compressa</i>	63.0	P1c	Berggren et al., 1995
B <i>Praemurica inconstans</i>	63.0		Berggren et al., 1995
B <i>Parasubbotina varianta</i>	63.0		Berggren et al., 1995
B <i>Subbotina triloculinoides</i>	64.5	P1b	Berggren et al., 1995
T <i>Parvularugoglobigerina extensa</i>	64.9		Olsson et al., 1999
T <i>Parvularugoglobigerina eugubina</i>	64.9	P1a	Berggren et al., 1995
B <i>Parvularugoglobigerina eugubina</i>	65.0	P α	Berggren et al., 1995

B = base, T = top, Tc = top common, X = coiling change.

Table T4. Age estimates of Cretaceous planktonic foraminifer datum events, Expedition 330.

Biostratigraphic event	Age (Ma)	Zone/Subzone base	Reference
T <i>Abathomphalus mayaroensis</i>	65.0		
B <i>Abathomphalus mayaroensis</i>	68.6	<i>Abathomphalus mayaroensis</i>	Sliter, 1989; Premoli Silva and Sliter, 1999
B <i>Racemiguembelina fructicosa</i>	69.6	<i>Racemiguembelina fructicosa</i>	Premoli Silva and Sliter, 1999
B <i>Contusotruncana contusa</i>	69.6		Premoli Silva and Sliter, 1999
B <i>Gansserina gansseri</i>	72.8	<i>Gansserina gansseri</i>	Sliter, 1989; Caron, 1985; Erba et al., 1995
B <i>Globotruncana aegyptiaca</i>	73.8	<i>Globotruncana aegyptiaca</i>	Sliter, 1989; Caron, 1985; Erba et al., 1995
T <i>Radotruncana calcarata</i>	75.2	<i>Globotruncanella havanensis</i>	Sliter, 1989; Caron, 1985; Erba et al., 1995
B <i>Radotruncana calcarata</i>	75.7	<i>Radotruncana calcarata</i>	Sliter, 1989; Caron, 1985; Erba et al., 1995
B <i>Globotruncana ventricosa</i>	79.5	<i>Globotruncana ventricosa</i>	Sliter, 1989; Caron, 1985; Erba et al., 1995
T <i>Dicarinella asymetrica</i>	83.0	<i>Globotruncanita elevata</i>	Sliter, 1989; Caron, 1985; Erba et al., 1995
B <i>Globotruncanita elevata</i>	84.8		Erba et al., 1995
B <i>Dicarinella asymetrica</i>	85.4	<i>Dicarinella asymetrica</i>	Sliter, 1989; Caron, 1985; Erba et al., 1995

T = top, B = base.

Table T5. List of observations recorded in the DESClogik log template for alteration, veins, and vesicles, Expedition 330.

Overall alteration	Veins	Vesicles
Sample	Sample	Sample
Top (cm)	Top (cm)	Top (cm)
Bottom (cm)	Bottom (cm)	Bottom (cm)
Top depth (m)	Top depth (m)	Top depth (m)
Bottom depth (m)	Bottom depth (m)	Bottom depth (m)
Alteration intensity name	Structure name	Structure name
Alteration intensity rank	Generation name	Vesicle abundance (%)
Alteration color	Total number of instance (<i>N</i>)	Vesicle sphericity
Groundmass altered (%)	Vein density (<i>N/cm</i> ²)	Vesicle roundness
Glass altered (%)	Vein maximum size (mm)	Vesicle maximum size (mm)
Olivine altered (%)	Vein modal size (mm)	Vesicle modal size (mm)
Olivine replacement mineral	Geometry name	Vesicle density (<i>N/cm</i> ²)
Plagioclase altered (%)	Vein filling crystal habit	Vesicle infilling (%)
Plagioclase replacement mineral	Vein filling mineral (%)	Vesicle infilling mineral
Alteration comment and interpretation	Vein halo thickness (mm)	Vesicle halo color
File data	Vein halo color	Vesicle halo thickness (mm)
	Thickness average (cm)	Vesicle description and comment
	Vein description and comment	File data
	File data	

Table T6. Wavelengths used for rock measurements by ICP-AES, Expedition 330.

Element	Wavelength (nm)		
	1	2	3
Major element:			
Si	250.690	251.611	
Ti	336.122	337.280	
Al	308.215		
Fe	238.204	239.563	
Mn	257.610	259.372	
Mg	280.271	285.213	
Ca	317.933	393.396	396.847
Na	588.995	589.592	
K	766.491		
P	214.914		
Trace element:			
Ba	233.527	493.409	
Sr	407.771	421.552	
Zr	339.198	343.823	
Y	360.073		
V	292.401	310.230	
Sc	361.383		
Cu	324.754		
Zn	206.200	213.856	
Co	228.615		
Cr	267.716	283.563	
Ni	231.604		

For elements listed with more than one wavelength, concentrations derived from each measurement were averaged if calibration lines for each wavelength were of similar quality. Otherwise, the wavelength yielding the best calibration line was used.

Table T7. Typical sequence of analyses in ICP-AES run, Expedition 330.

Analysis no.	Identifier/Type
1	DRIFT 1 (BHVO-2)
2	BLANK - 1
3	BHVO-2 STD
4	BIR-1 STD
5	BCR-2 STD
6	DRIFT 2 (BHVO-2)
7	JGB-1 STD
8	JA-3 STD
9	SCO-1 STD
10	JR-1 STD
11	DRIFT 3 (BHVO-2)
12	MRG-1 STD
13	NBS-1C STD
14	Check
15	Check
16	DRIFT 4 (BHVO-2)
17	Sample
18	Sample
19	Sample
20	Sample
21	DRIFT 5 (BHVO-2)
22	Sample
23	Sample
24	Sample
25	Sample
26	DRIFT 6 (BHVO-2)
27	Sample
28	Sample
29	Sample
30	Sample
31	DRIFT 7 (BHVO-2)
32	BLANK - 2
33	Check
34	Check
35	Sample
36	DRIFT 8 (BHVO-2)
37	Sample
38	Sample
39	Sample
40	Sample
41	DRIFT 9 (BHVO-2)
42	Check
43	Check
44	BLANK - 3
45	DRIFT 10 (BHVO-2)

STD = calibration standard, check = check standard, DRIFT = drift correction standard. As many as 22 samples were included in a batch.

Table T8. BHVO-2 check standard data for ICP-AES analysis, Expedition 330.

Element	Mean (<i>N</i> = 4)	2σ	Recommended
Major element (wt%):			
SiO ₂	49.61	0.30	49.90
TiO ₂	2.70	0.04	2.73
Al ₂ O ₃	13.63	0.31	13.50
Fe ₂ O ₃ ^T	12.29	0.43	12.30
MnO	0.16	0.00	0.17
MgO	7.22	0.10	7.23
CaO	11.47	0.30	11.40
Na ₂ O	2.20	0.23	2.22
K ₂ O	0.48	0.08	0.43
P ₂ O ₅	0.25	0.05	0.27
Trace element (ppm):			
Ba	128	14	130
Sr	388	25	389
Zr	163	10	172
Y	24	8	26
V	317	12	317
Sc	29	6	32
Cu	126	6	127
Zn	101	5	103
Co	53	2	45
Cr	266	58	280
Ni	117	7	119

Mean values of four analyses are indicated, except for Sc, for which the mean of three analyses is shown (Sc data were not obtained in one run). Uncertainties are listed as ±2 standard deviations (σ). Recommended values are from Govindaraju (1994). Fe₂O₃^T is total iron calculated as ferric oxide.

Table T9. MAD variables, units, and calculations, Expedition 330.

Quantity and variable	Unit	Value or calculation
Density of salt, ρ _{salt}	g/cm ³	2.22
Density of pore water, ρ _{PW}	g/cm ³	1.024
Mass ratio (salinity correction)	None	0.965
Wet mass, <i>M_W</i>	g	Measured
Dry mass, <i>M_D</i>	g	Measured
Dry volume, <i>V_D</i>	cm ³	Measured
Mass of pore water, <i>M_{PW}</i>	g	(<i>M_W</i> - <i>M_D</i>)/Mass ratio
Volume of pore water, <i>V_{PW}</i>	cm ³	<i>M_{PW}</i> /ρ _{PW}
Mass of salts, <i>M_{salt}</i>	g	<i>M_{PW}</i> - <i>M_W</i> + <i>M_D</i>
Volume of salts, <i>V_{salt}</i>	cm ³	<i>M_{salt}</i> /ρ _{salt}
Wet volume, <i>V_W</i>	cm ³	<i>V_D</i> - <i>V_{salt}</i> + <i>V_{PW}</i>
Mass of solids, <i>M_{solids}</i>	g	<i>M_W</i> - <i>M_{PW}</i>
Volume of solids, <i>V_{solids}</i>	cm ³	<i>V_W</i> - <i>V_{PW}</i>
Porosity, φ	None	<i>V_{PW}</i> / <i>V_W</i>
Wet density, ρ _W	g/cm ³	<i>M_W</i> / <i>V_W</i>
Dry density, ρ _D	g/cm ³	<i>M_{solids}</i> / <i>V_W</i>
Grain density, ρ _{grain}	g/cm ³	<i>M_{solids}</i> / <i>V_{solids}</i>
Void ratio	None	<i>V_{PW}</i> / <i>V_{solids}</i>

Table T10. MATLAB data filtering parameters, Expedition 330.

Instrument	Minimum detectable gap (cm)	Edge effect (cm)	Minimum piece length (cm)
GRA	0.05	1.0	2.0
MS	0.05	2.0	4.0
MS point	0.05	1.5	3.0
L*	0.05	1.5	3.0
a*	0.05	1.5	3.0
b*	0.05	1.5	3.0

GRA = gamma ray attenuation densitometer, MS = magnetic susceptibility measured with the WRMSL, MS point = magnetic susceptibility measured with the SHMSL.

Table T11. Type of measurements made by wireline logging tool strings, Expedition 330.

Tool string	Tool	Measurement	Sampling interval [†] (cm)	Approximate vertical resolution (cm)
Triple combination*	HNGS	Spectral gamma ray	15	51
	GPIT	Tool orientation	0.25 and 15	NA
	APS	Porosity	5 and 15	43
	HLDS	Bulk density	2.5 and 15	38/46
	DIT	Resistivity	15	200/150/76
Formation MicroScanner-sonic combination*	HNGS	Spectral gamma ray	15	51
	GPIT	Tool orientation	0.25 and 15	NA
	FMS	Microresistivity imaging	0.25	0.5
	DSI	Acoustic velocity	15	107
Ultrasonic Borehole Imager*	UBI	Ultrasonic imaging	Variable	0.5–2
	GPIT	Tool orientation	0.25 and 15	NA
	HNGS	Spectral gamma ray	15	51
Göttingen Borehole Magnetometer	GBM	Magnetic field	5	NA
		Tool orientation		

* = trademark of Schlumberger. † = sampling interval based on optimal logging speed. NA = not applicable. For definitions of tool acronyms, see Table T12.

Table T12. Acronyms and units for downhole wireline tools and measurements, Expedition 330.

Tool	Output	Explanation	Unit
APS		Accelerator Porosity Sonde	
	APLC	Near array porosity (limestone calibrated)	%
	SIGF	Formation capture cross section (Σ_c)	Capture units
	STOF	Tool standoff (computed distance from borehole wall)	Inch
DIT		Dual Induction Tool	
	IDPH	Deep induction resistivity	Ωm
	IMPH	Medium induction resistivity	Ωm
	SFLU	Spherically focused resistivity	Ωm
DSI		Dipole Shear Sonic Imager	
	DTCO	Compressional wave delay time (Δt)	$\mu\text{s}/\text{ft}$
	DTSM	Shear wave delay time (Δt)	$\mu\text{s}/\text{ft}$
	DTST	Stoneley wave delay time (Δt)	$\mu\text{s}/\text{ft}$
FMS		Formation MicroScanner	
	C1, C2	Orthogonal hole diameters	Inch
	P1AZ	Pad 1 azimuth Spatially oriented resistivity images of borehole wall	$^\circ$
GPIT		General Purpose Inclinerometry Tool	
	DEVI	Hole deviation	$^\circ$
	HAZI	Hole azimuth	$^\circ$
	F _x , F _y , F _z A _x , A _y , A _z	Earth's magnetic field (three orthogonal components) Acceleration (three orthogonal components)	Oe m/s ²
HLDS		Hostile Environment Litho-Density Sonde	
	RHOM	Bulk density	g/cm ³
	PEFL	Photoelectric effect	b/e ⁻
	LCAL	Caliper (measure of borehole diameter)	Inch
	DRH	Bulk density correction	g/cm ³
HNGS		Hostile Environment Natural Gamma Ray Sonde	
	HSGR	Standard (total) gamma ray	gAPI
	HCCR	Computed gamma ray (HSGR minus uranium contribution)	gAPI
	HFK	Potassium	wt%
	HTHO	Thorium	ppm
	HURA	Uranium	ppm
UBI		Ultrasonic Borehole Imager	
		Spatially oriented acoustic images of borehole wall	
		Acoustic arrival times and amplitudes	μs
		Borehole diameter Borehole azimuth	Inch $^\circ$
GBM		Göttingen Borehole Magnetometer	
	B _x , B _y , B _z	Earth's magnetic field (three orthogonal components)	Bits (tool coordinate system)
	R _x , R _y , R _z	Tool rotation	Bits (converted to degrees)
	N _x , N _y	Inclination/Deviation	Bits (converted to degrees)
	T1, T2	Telemetry and gyro temperature	Bits (converted to $^\circ\text{C}$)
	F _x , F _y , F _z	Magnetic field (corrected for tool rotation)	nT

For the complete list of acronyms used in IODP and for additional information about tool physics, consult IODP-USIO Science Services, LDEO, at iodp.ldeo.columbia.edu/TOOLS_LABS/tools.html.

Table T13. Specifications of the Göttingen Borehole Magnetometer, Expedition 330.

Component	Specification
Borehole magnetometer	Three-component fluxgate
Power supply	50 V/0.25 A (12 W)
Random walk of fluxgate sensors (nT)	<0.1
Range (μ T)	± 50 (x and y magnetometer), ± 70 (z magnetometer)
Resolution (nT)	6.1 (x and y magnetometer), 8.54 (z magnetometer)
Data transmission	Digital two-wire Manchester encoded
Sample rate	Eight readings from 8 channels/s
Data acquisition system	Personal computer (DOS)
Tool weight (kg)	68
Tool length (m)	3.5
Tool diameter (mm/inch)	86 (3.375)
Housing	Low-magnetic monel
Maximum operation temperature ($^{\circ}$ C)	0–70 (limited by FOGs)
Maximum operation pressure (MPa)	70
Recommended logging speed (m/h)	300 (open hole)
Maximum logging speed (m/h)	3700 (limited by hole diameter)
Tool navigation system	Three FOG μ FORS-36 m (LITEF)

FOG = fiber-optic gyro, μ FORS = miniature fiber-optic rate sensor.

Table T14. Media used for culturing prokaryotes, Expedition 330.

Media	Component	Mass/Volume/ Concentration	Treatment after mixing components
Artificial seawater (ASW)	18.2 MΩ·cm MilliQ Water	1 L	Before adding, adjust pH to 7.3 and autoclave
	NaCl	27.5 g	
	MgCl ₂ ·6H ₂ O	12.16 g	
	KCl	0.72 g	
	NaHCO ₃	0.2 g	
	Tris-HCl	3.2 g	
	CaCl ₂ ·2H ₂ O	1.4 g	
	NH ₄ Cl	0.05 g	
	K ₂ HPO ₄ ·3H ₂ O	0.05 g	
	Trace elements solution	1 mL	
Trace vitamins solution	1 mL		
Trace elements solution	ATCC trace mineral supplement		
Trace vitamins solution	18.2 MΩ·cm MilliQ water	1 L	Filter sterilize (no autoclave); store in darkness at 4°C
	Calcium pantothenate	10 mg	
	Niacin	10 mg	
	p-aminobenzoic acid	10 mg	
	Thiamine	10 mg	
	Riboflavin	10 mg	
	Pyroxidine	10 mg	
	Cobalamin (Vitamin B ₁₂)	10 mg	
	Thioctin (α-lipoic) acid	10 mg	
	Folic acid	10 mg	
	Biotin	10 mg	
Autotrophic sulfur-oxidizing bacteria (ASOB)	Start with ASW		Purge with N ₂ prior to inoculating
	Na ₂ S ₂ O ₃	10 mM	
	Na ₂ S	100 μM	
Heterotrophic sulfur-oxidizing bacteria (HSO)	Start with ASOB		Purge with N ₂ prior to inoculating
	Dextrose	10 mM	
Autotrophic sulfate-reducing bacteria (ASR)	Start with ASW		Purge with N ₂ prior to inoculating
	Na ₂ SO ₄	60 mM	
	Na ₂ S	500 μM	
Heterotrophic sulfate-reducing bacteria (HSR)	Start with ASR		If adding acetate as acetic acid, readjust pH to 7.3
	Lactate	10 mM	
	Acetate	10 mM	
Autotrophic methanogen (AM)	Start with ASW		Filter sterilized solution Purge with N ₂ prior to inoculating
	Sodium molybdate	5 mM	
	Na ₂ S	100 μM	
Heterotrophic methanogen (HM)	Start with AM		Purge with N ₂ prior to inoculating
	Methanol	10 mM	
Autotrophic Fe(III)-reducing bacteria (AIR)	Start with ASW		Goethite (<250 μm) or ferrihydrite are best; purge with N ₂ prior to inoculating
	Poorly crystalline Fe oxides		
Heterotrophic Fe(III)-reducing bacteria (HIR)	Start with AIR		If adding acetate as acetic acid, readjust pH to 7.3
	Lactate	10 mM	
	Acetate	10 mM	
Autotrophic Fe(II)-oxidizing bacteria	Start with ASW		Add semi-daily, with some O ₂ ; keep microaerophilic (with added resazurin, solution should remain pink)
	FeCl ₂	1 mM	
Marine broth (selects for heterotrophs; use 50%, 10%, and 1% media solution, diluted with autoclaved 3% NaCl)	Difco marine broth from Sigma (Sigma-Aldrich, St. Louis, MO)		

Table T15. Range of concentrations for stable isotopes, Expedition 330.

Stable isotope	Range of concentrations added (mM)
¹³ C bicarbonate	2.7
¹³ C glucose	10
¹³ C acetate	0.10–10
¹⁵ N ammonia	0.00050–0.50
¹⁵ N nitrate	0.001–1.0
³⁴ S elemental sulfur	0.00030